# Durham E-Theses

## *Parton model and large P(_t) phenomena*

Da'ee, Mohammad Sadegh

**How to cite:**

Da'ee, Mohammad Sadegh (1978) *Parton model and large P(_t) phenomena*, Durham theses, Durham University. Available at Durham E-Theses Online: http://etheses.dur.ac.uk/9032/

**Use policy**

The full-text may be used and/or reproduced, and given to third parties in any format or medium, without prior permission or charge, for personal research or study, educational, or not-for-profit purposes provided that:

- a full bibliographic reference is made to the original source
- a link is made to the metadata record in Durham E-Theses
- the full-text is not changed in any way

The full-text must not be sold in any format or medium without the formal permission of the copyright holders.

Please consult the full Durham E-Theses policy for further details.

PARTON MODEL

AND

LARGE $P_t$ PHENOMENA

by

MOHAMMAD SADEGH DA'EE

A thesis submitted for the degree of
M.Sc. of the University of Durham

December 1978

Department of Mathematics
University of Durham
South Road
Durham City
England   DH1 3LE

## PREFACE

Under supervision of Professor E. J. Squires to whom I wish sincerely to express my deep gratitude for his continuous guidance, encouragement, and patience, presented work has been carried out in the Durham University Mathematics Department. Also, many thanks to the lecturers of both mathematical and theoretical physics departments from whom I have benefitted a great deal.

## ABSTRACT

Our understanding of large $P_t$ phenomena from the point of view of the quark-parton model is reviewed in this thesis. For this purpose some necessary experimental and theroetical background related to low $P_t$ phenomena is given in the first chapter. We show in particular that the inclusive single particle cross section at low $P_t$ follows a simple curve but that this falls far below the data when it is extrapolated to high $P_t$. This suggests the existence of small constituents. In the second chapter we show how the existence and properties of these constituents are established in the simpler situation of lepton-hadron scattering processes. The constituents are approximately point-like, spin one-half, quarks.

In the third chapter we see how large $P_{j}$ hadronic processes can be used to probe the small scale structure of hadrons, and how the experimental results confirm the quark structure. We discuss several versions of the model and show that a reasonably consistent picture emerges. There are, however, some difficulties which can hopefully be overcome by the introduction of QCD (gluon) corrections.

For this mixed experimental-theoretical review, kinematics concerning two-body and inclusive reactions are given in Appendices A and B. Also, related to the low $P_t$ discussion of the first chapter, some theoretical background (e.g. scaling, limiting fragmentation and Regge-Muller formalism) is given in Appendix C.

# CONTENTS

# CHAPTER I

## Preliminary Remarks concerning
### Low and Large $P_t$ Phenomena

## I.1 Introduction

To elucidate the forces between particles and their overall
size and shapes we look after their elastic scattering. But the
structure and excitation of matter have to be obtained through
their inelastic scattering. In this way, we see that the
detailed study of the complete final state of three, four, or
more particles has been done through quasi-two-body processes
with one or two resonances in the final state. Through these
so-called exclusive processes lots of information on decay,
correlation, and energy dependences have been gained. On the
other hand, via inclusive interactions where we look at one or
few final states and sum over everything else; e.g.:

$$ab \longrightarrow x \qquad \text{zero-particle inclusive process} \qquad (I.1a)$$

which is just the total X-section, $\sigma_{ab}^{tot}$, depending only on the
incoming energy, and:

$$ab \longrightarrow cx \qquad \text{one-particle inclusive process} \qquad (I.1b)$$

and:

$$ab \longrightarrow cdx \qquad \text{two-particle inclusive process} \qquad (I.1c)$$

with $x = \sum$ (all possible final states except those which are
presented), application of ideas closely related to two-body
phenomenology, through Kinematics, can be considered. In this
field, the simple and general properties are scaling and
limiting fragmentation. These important results seem not to be

working at large angles and energies. This violation causes consequences which are showing onset of a somehow different essential feature of the dynamics of the hadronic interactions. Experimental enhancements to this, however, will be reviewed in Section (I.4) after tracing out the degree of success of the ideas based on the aforementioned hypothesis in Section (I.3).

Before embarking on above experimental implications, typical two-body reactions at large momentum transfer data which are also showing some disbehaviour from what they used to do at smaller $|t|$ are given in Section (I.2).

However, related kinematics of two-body and inclusive reactions will be reviewed in Appendices A and B. Also some theoretical aspects, such as scaling, limiting fragmentation, and Regge-Muller formalism are reviewed in Appendix C.

## I.2 Theoretical and Experimental Remarks Concerning Two-Body Reactions

### (I.2a) Remarks on two-body reactions at small - $|t|$

Phenomenologically, we subdivide two-body (TB) and quasi-two-body problems (QTB):

$$1 + 2 \longrightarrow 3 + 4 \qquad (I.3)$$

where 3 and/or 4 may be particles or resonances, into[1] two classes:

(i) The processes of diffractive type which proceeds by Pomeron exchange (e.g.: $I_t = B_t = S_t = 0$, $C_t = +$, $P = (-1)^j$).

(ii) The reactions which proceed by meson or baryon exchange. Elastic scattering may be considered as process of type (i), while charge exchange scattering is of type (ii).

The high energy elastic differential cross section is dominated by a peak at small momentum transfer, $|t|$. This small $|t|$ peak, a universal property of all such systems

that have been studied, is ascribed to a very general process: diffractive elastic scattering. Following this orientation, the small $|t|$ peak is found to be called "diffractive peak" and the region is called "the diffractive region" wherein the differential x-section is roughly fitted by $e^{Bt}$ where $t = -q^2$ is the invariant momentum transfer variable. As $|t|$ increases beyond the exponential region, $d\sigma/dt$ begins to flatten out sometimes[1] smoothly as in PP scattering in 3-7 GeV/C ranges shown in Fig. 1, sometimes[2] with bumps or dips as in $\bar{K}P$ data shown in Fig. 2. However, mostly diffractive region is taken as $|t|$ varying between 0 up to 1.5 $(GeV/C)^2$.

Having been guided still by the invariant variable $t$ which can be given in c.m. as:

$$t = -2P^2(1 - \cos\theta) \; ; \quad P = |\underline{P}_1| = |\underline{P}_2| \tag{I.4}$$

we see that at the other end of the angular range from the diffractive region, the behaviour of the differential cross section at $\theta = 180^\circ$, which is called "the backward scattering region" wherein data are still fitted to an exponential form like $e^{Bu}$, is extremely varied; sometimes there is a peak at $180^\circ$ such as that shown in Fig. 2 for $K^+P$ and $\bar{K}P$, for other systems at other energies there may be seen smaller peaks and dips or a flat region. But in no case does $d\sigma/dt$ approach the size of the diffraction peak.

(I.2b) Scattering at large angles

The Data - Energy dependence of $d\sigma/dt$ in TB reactions is obvious, such that: if we move on with energy further we find a kind of power law behaviour in s, roughly like $s^{-n}$ at fixed t for $d\sigma/dt$. The power has dependence on the reaction mechanism. As an example Fig. 3 shows the characteristic behaviour of $d\sigma/dt$ of elastic scattering of the pion and nucleon. This wide

angle - roughly at $90°$ in c.m., so in the t- (or u-) region greater than 1 or 2 $(GeV/C)^2$ - elastic scattering shows[3] that the differential cross section tends to be flat. Understanding of the decrease of this cross section with energy which is approximately as $s^{-(8\pm1)}$ is believed to be in the framework of forthcoming models which will consider large angle scattering as due to the interaction of the pointlike constituents of the hadrons. However, Fig. 4 shows[1] the energy dependence of the differential cross section of pp scattering at various values of t at ISR energies. It is evidence that at low energies and high four momentum transfer the s-dependence is much weaker than at high energies and low four momentum transfer. Thus one may see that part of the energy dependence is of a kinematical nature, connected with sort of threshhold effect on high momentum effect.

Regge Pole Picture - Of models explaining the small and large angle data of TB reactions is the Regge pole picture[6] in which, for instance, we may consider a sort of core plus a periphery and apply the Pomeron trajectory discussion either to the periphery[4] or conversely to the core.[5] However in the task of constructing[7] relationships between the Regge model of high energy two body reactions and the one particle exchange model of these reactions, theorists have been succeeded by different experimental observations confirming stability of the following relations:

$$d\sigma/dt \xrightarrow[s \gg]{} \beta(t) s^{2\alpha(t)-2} \qquad (I.5)$$

for the exchange of a simple Regge pole in the t-channel. In eq. (I.5) $\beta(t)$ is some function of t containing the amplitude of the process, and $\alpha(t)$ is the pole trajectory function

fixing the energy dependence of $d\sigma/dt$ at each value of t. Moreover , cocerning with problems related to the contribution of other poles (rather than just one pole) and cuts to the amplitude, we may define an $\alpha_{eff}(t)$ by:

$$d\sigma/dt \rightarrow \beta(t) \, s^{2\alpha_{eff} - 2}$$

(I. 6)

But at sufficiently high energies , $\alpha_{eff}(t)$ is expected [7] to correspond to the leading trajectory for the process; i.e. : the leading trajectory is the one which is dominating over the other trajectories of the process with its highest $Re\,\alpha(t)$ at any given t. Therefore, still there seems to be no harm in determining $\alpha_{eff}(t)$ from eq. (I .5) through the following formula at high enough energies :

$$Log(d\sigma/dt) = (2\alpha(t) - 2)log\, s + Log\,\beta(t)$$

(I .7)

For a given process,therefore, at each fixed t,plotting $log(d\sigma/dt)$ versus $log(s)$ determines the effective trajectory for that process. This is the case in the following example of pion-proton charge exchange scattering, namely: $\pi^- p \rightarrow \pi^0 n$ . We know the behaviour of this charg exchange cross section,when it is integrated,should show a power law behaviour at some small negative value of $|t|$ . On the other hand, we see from Fig. 5a,showing[8] the energy dependence of the differential charge exchange cross section of this pross from 6 to 100 Gev, that the energy behaviour of this process at large $|t|$ is clearly different from that at small $|t|$ . Also the process shows a narrow forward peak in t which confirms the correspondance of the present picture with that of one particle exchange model. These all confirm the validity of eq. (I .5). However, the anticipated t-channel exchange and the effective value of $\alpha$ being deduced from the appropriate exponent,are[9] as follows:

| Exchange | Effective $\alpha$ |
|----------|--------------------|
| $f$      | $0.41 \pm 0.07$    |

However, the value of $\alpha \sim 0.4 - 0.5$ is seen to be in good agreement to fit within the experimental errors, to a linear Regge trajectory $\alpha = 0.5_4 t$ which, as it is seen in Fig. 5b, passes through $f(J = \bar{1}, \; m_f^2 = 0.58 \pm 0.10 \; GeV^2)$ and $g(J = \bar{3}, \; m_g^2 = 2.82 \pm 0.27 \; GeV^2)$. This $f$—trajectory, and other experimental evidence on existence of such trajectories, which extrapolates closely to $f$-meson position at $\alpha = 0.5 \; t \; (GeV/C)^2$ confirms the connection of Regge trajectories with particles.

Shrinkage: and very large $|t|$-region - Consulting Fig. 5a, it is seen that the roughly smooth behaviour at "low" energies of the cross sections gradually evolves into structure at $|t| \sim 1-2 (GeV/C)^2$ at higher energies as the x-section "shrinks" (i.e.: becomes compressed to smaller and smaller t-values). This shrinkage of the cross section is attributed[10] to, here, $\alpha_\rho (t) < 0$, and the rate of shrinkage at each fixed-t is said to be given by the value of $\alpha_\rho (t)$ at that value of t.

Shrinkage may also be described in terms of "slope parameter" B, defined by:

$$B(s,t) = \frac{d}{dt} \left( \log (d\sigma/dt) \right) \tag{I.8a}$$

this at high energies has been preicted by the Regge theory as:

$$B(s,t) = 2 \frac{d\alpha_{eff}(t)}{dt} \log s + B_o(t) \tag{I.8b}$$

For PP $\longrightarrow$ PP, eq. (I.8b) is the normal Regge shrinkage as well as the exponent of the observed exponential behaviour of $\frac{d\sigma}{dt}$ (PP $\longrightarrow$ PP) down to $t = -1.3 \; (GeV/C)^2$ where the clear dip

of $d\sigma/dt$ appears. As it is seen in Fig. 6 beyond $|t| = 2.5$ (GeV/C)$^2$ (up to 6.5 (GeV/C)$^2$) first of all[11] shrinkage has stopped (Fig. 6a), secondly[12] throughout the entire s-range considered there are no further minimum in $\frac{d\sigma}{dt}$ (PP ⟶ PP) or change in its (observed) logarithmic slope $D = 1.8$ (GeV/C)$^{-2}$ (Fig. 6b). Notice that drawn curves in Fig. 6a are fits to the data from two-amplitude model[13] of Philips and Barger: elastic scattering in the large t-region is described by coherent superposition of two exponential amplitudes, where the second one is energy independent (represented by slope D) and the first one is shrinking with increasing energy (represented by B of eq. (I.8b)):

$$\frac{d\sigma}{dt} = \left| \sqrt{A}\ exp\ (Bt/2) + \sqrt{C}\ exp\ (Dt/2 + i\phi) \right|^2 \tag{I.9}$$

This parametrization of the scattering to exponentials with a relative phase of $\phi$ gives the s-dependence of $d\sigma/dt$ at a fixed t, when C and D parameters are kept constant, in terms of other parameters independent of any interference effect - such as an interference between single and double pomeron exchanges - causing the dip.

However, falling off of the different large angle cross section at approximately the same rate, that is: the absence of any shrinkage effects beyond $|t| \sim 2.5$ (GeV/C)$^2$, indicates[14] the possibility of factorizing the cross sections in this large angle regime approximately as:

$$\frac{d\sigma}{dt} (s, \cos\theta) \Big|_{\cos\theta \neq \pm 1} \sim f(s)\ g(\cos\theta) \tag{I.10}$$

For example Fig. 7 which shows the PP cross section data at different energies normalized to 90° cross section is the possibility of this indicated factorization. Moreover, in comparison with Regge regime which operates at smaller $|t|$

than 2.5 $(GeV/C)^2$ or[15] at smaller $\Theta$ cm. than $10^O$, taken data at large s and large t or large $\Theta$ cm. may belong to a region in which the peripheral component has died away.[16]

## I.3   Single Particle Inclusive Experiments

In analyzing the experimental data on invariant cross section, by consulting the kinematic, one may be mainly starting using one of the two sets of variables $(x, P_t)$ and $y, P_t)$. In each case, experimentally, one of the variables of the set is kept constant while the other is varied. Hence we may start by following the phenomenological subdivision of $f = f(P_t)$ as illustrated below, where $P_t < 0.1$ $(GeV/C)^2$ is devoted to the small $P_t$ region. In this region, the lower energy data and general analytic considerations are suggestive[17] of a weak $P_t$ dependence of the invariant cross section.
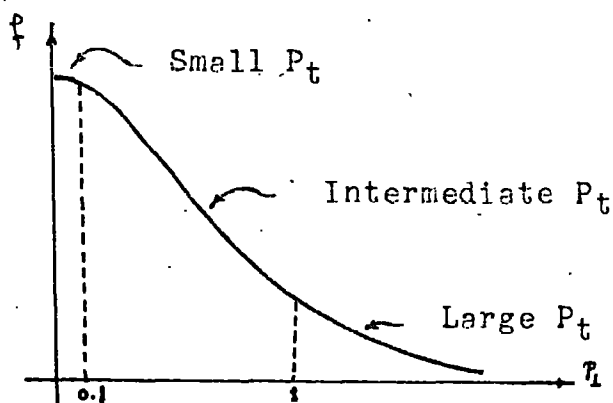


Diag.I.1:   Illustration of the shape
of the $P_t$ distribution

(I.3a)   Intermediate $P_t$ region:   $0.1 < P_t < 1$ $GeV/C^2$

Here the upper limitation on $P_t$ may grow up to 1.4 or 1.5 GeV. For instance: for reactions $PP \longrightarrow (\pi^\pm, K^\pm, P^\pm) + x$, emitted particles in the angular range $80^{m \cdot rad} \leqslant \Theta \leqslant 300^{m \cdot rad}$ with momentum $1.5 \leqslant P \leqslant 10$ GeV/C are corresponding to the range of $0.15 \leqslant P_t \leqslant 1.5$ GeV/C at ISR[18]. At this range of $P_t$ and where on a sign of no major energy dependence, the data group together either global (i.e. studying all the experiment-

ation) or differential(studying of the shape of the $P_t$ distribution of the produced particles will be done by keeping constant the x or the $y_{lab}$ variables). In this way the following expressions have been fitting the data:

$$f = \frac{E d^3 \sigma}{d^3 p} = A e^{-B P_\perp} \qquad (I.11a)$$

$$= c e^{-D P_\perp^2} \qquad (I.11b)$$

$$= E e^{-F m_\perp} \quad ; \quad m_\perp = (P_\perp^2 + m^2)^{1/2} \qquad (I.11c)$$

Using (I.11a) to fit the data (on $\pi^+$ at fixed x = 0.075, 0.30) results in the shown dashed-straight lines in Fig. 8 where the other dashed-curves are the results of using (I.11b) and (I.11c) to fit the data on $\pi^+$, $K^+$, and P. Notice, when $P_\perp > m$, naturally eq. (I.11c) is equivalent to eq. (I.11a). Also in this region $P_t$ is sometimes so small that plotting versus $P_t$ gives a poor statistic to each bin. For this reason, these data are fitted by eq. (I.11b). In this sense, eqs. (I.11) are representing a kind of universal curve. Basing on this universality, Hagedorn[19] and his co-workers used to extrapolate down the curve for gaining some more knowledge about the hadronic interactions at higher energies which were not available at their time. We return to this subject in Section (I.4) below.

(I.3b)  Limited transverse momentum

In the transverse direction all types of particles tend to be limited in $P_t$. This can be numerically evaluated using the following definition of $< P_t >$ :

$$< P_\perp > = \int f \, P_\perp \, dP_\perp^2 \Big/ \int\int f \, dP_\perp^2 \qquad (I.12a)$$

By assuming factorization of the cross section with the parametrization (I.11a), we compute $< P_t >$ by keeping fixed either

$x(so, <P_t>_x)$ or $y_{lab}$ (therefore $<P_t>_{y_{lab}}$ ) from

$$< P_t > = 2/B \qquad\qquad (I.12b)$$

Apart from "seagull effect" rigon - namely: a dip at $x \approx 0$ which disappears letting $<P_t>_x$ to be approximately constant from $x \geqslant 0.2$ onward - of pions in $(<P_t>_x, x)$ plot of Fig. 9a, the quick increase of $< P_t >$ in the fragmentation region [(from $y_{lab} \leqslant 1$, up to $y_{lab} \leqslant 2$) where large transverse momenta cannot be found ] and slowly increase of $< P_t >_{y_{lab}}$ with $y_{lab}$ after $y_{lab} \approx 2$ (which means eq. (I.11a) is only a first order approximation even for large $y_{lab}$) in $(<P_t>_{y_{lab}}, y_{lab})$ plot of Fig. 9b we may find mean values of transverse momenta of the order of $< P_t > \simeq 0.33$ GeV/C for pions and $< P_t > \simeq 0.4-0.5$ GeV/C for $K^\pm$ or $P^\pm$. However, even at very high energies, there is seen[21] little variation in $< P_t >$ . In fact, the most common strong interactions and even E.M. phenomena are characterized by low mean $P_t < 1$ GeV/C.

This smallness of $< P_t >$ may, however be assigned[21] to peripherality interactions of hadrons through exchanging a soft quanta as the dominant mechanism.

## (I.3c) Multiplicities

From the topological cross section[22] for the production of events with n charged secondaries, it is seen that the theoretical[23] models are predicting the energy dependence of the multiplicities to be of the (log S) type in the high energy region, while at low energies it is predicted to be of a power type, $S^\alpha$ . However, combination of both types has also been used to fit the multiplicities over the complete range of energies; i.e.:

$$< n_c > = A + B \log S + c S^{-1/4} \qquad\qquad (I.13)$$

$$< n_c > = A + B \log S + C S^{-1/2} \log S \qquad (I.14)$$

With some fits[24,25] made to the mean number of charged
hadrons per collision of PP at ISR energies, these fits show that
$< n_{ch} >$ grows much less rapidly than the maximum rate of
growth $\sim \frac{2}{3} \sqrt{s}$ which may be possible. However, as it is seen
from Fig. 10, the pions, at high energies, are taking over the
bulk of multiplicity and rise in proportion to the total $< n_{ch} >$ .

(I.3d) <u>Longitudinal Behaviour of Inclusive Distribution</u>

So far we have seen that there is a $P_t$ -limitation for all
particles in their transverse motion, and also not a lot of
energy goes into particle production. Hence the influence of
energy is obvious in altering the longitudinal momentum
dimension, $P_{11}$. The mean centre of mass longitudinal momentum
grows in proportion to $\sqrt{s}$;

$$< P_{11} > = \eta_h \sqrt{s} \qquad (I.15)$$

With respect to the Feynman scaling hypothesis which comes
later, it is seen that: $\eta_h = < x_h >$ . This is equal[26] to
0.5 for the final proton in PP $\longrightarrow$ Px.

Longitudinal momentum distribution of a single particle
inclusive reaction data in an invariant cross section $f(x)$
versus $x$ plot are seen all contracted in a small interval
around $x = 0$, the width of which decreases with increasing
energy. This plot is, then, used to study the production of
particles with very high longitudinal momentum. On the other
hand, the variable-$y$, the range of which increases logarith-
mically with $s$, allows a rather well description of the over-
all distribution in a $f(y)$ versus $y$ plot.

The Y-distribution can be divided into three parts, two "fragmentation regions", at the extremes of the plot, with rapidities close to the rapidity of the incident particles, and for which the limiting fragmentation[38] and scaling[39] predictions can be summarized as:

$$\rho_{ab}^{c}(Y, Y_{projectile}, \tau_\perp) \xrightarrow[Y(s) \gg]{} \rho_{ab}^{c}(Y_{projectile}, \tau_\perp)$$

which can be approached by roughly a $s^{-\frac{1}{2}}$ dependence as is predicted in the Muller Regge formalism. For the third region which is centred around $y_{cm} = 0$, the "central region", in which the scaling hypothesis prediction may be read as:

$$\rho_{ab}^{c}(Y, Y_{c.m.}, \tau_\perp) \xrightarrow[Y(s) \gg]{} \rho_{ab}^{c}(\tau_\perp) \qquad \text{in the plateu around } Y_{c.m.} \sim 0$$

the aforementioned formalism predicts that the approach to this limit takes place at a slower rate than in the fragmentation regions, as a $s^{-\frac{1}{4}}$.

(I.3e)  S-dependence of the Intermediate $P_t$ Particle
        Production Spectra In The Fragmentation Region

Attempts for observing experimentally the concepts of scaling as well as Pomeron factorization (i.e. cross sections which are independent of the incident projectile) is for simplfying the problems of describing secondary particle spectra produced in the collision of a projectile and target particle and gaining information on the nature of the Pomeron singularity and on the validity of the secondary trajectory exchange process for a single particle inclusive reaction. As is seen in Fig. 11, which shows analysis of the data[27] of the reaction $P \xrightarrow{a} \pi^{\pm}$ with $a = \pi^{\pm}$, $K^{\pm}$, $P$, $\bar{P}$, and $\gamma$ ranging from an incident momentum of 3.7 GeV/C to 400 GeV/C, in the fragmentation region most of the reactions exhibit falling cross sections in disagreement with the hypothesis of limiting fragmentation, while the spproach to scaling behaviour in the

limit of infinite energy appears (from above) consistent with the expected $s^{-\frac{1}{2}}$ dependence, and having hold a factorization in the limit of infinite energy is not rejected since the data appear to converge at a common point as $s^{-\frac{1}{2}} \longrightarrow \infty$ .

### (I.3f) S-dependence of the Intermediate $P_t$ Particle Production Spectra In The Central Region

Experimental observations are all showing[28], depending on type of produced particle, an average increase of the differential cross section over the ISR energy range at $x = 0$. This is in contrast to what is expected from the invariant cross section at fixed values of $P_t$ and $x(y)$ at high energies according to the Feynman scaling hypothesis. Also the displayed data[28] on Fig. 12 for $(PP \longrightarrow \pi^{\pm}x)$ experiment at $P_t = 0.5$ GeV/C versus $s^{-\frac{1}{4}}$ being taken as an approach to scaling, are all consistent with an approach like $s^{-\frac{1}{2}}$. This is not inconsistent with what has been predicted from Regge-Muller formalism for central region. Certainly[29] by taking into account all the appropriate contributing double-Regge diagrams (see Appendix C), the correct approach to scaling limit, and hence an asymptotically constant cross section being implied by the significant violation of scaling at $x = 0$ in the available energy range, can be obtained.

### I.4 Large $P_t$ region, $P_t > 1$ GeV/C

The following certain elements of the Table below characterizes[30] the low $P_t$ domain of a production spectra.

| Low $P_t$ Spectra | Behaviour | Particle Ratios |
|---|---|---|
| Dependence on increasing $P_t$ (at fixed s) | A rapid exponential decrease. The s-independent slope of which is larger for lighter particles than for heavier ones. | Mostly pions<br>$\pi/\kappa \sim 10\%$<br>$\pi^+/\pi^- \sim 1$ |
| Dependence on increasing s (at fixed $P_t$) | Approximately very weakly rising/none. | |
| Notice that: In general the Average Transverse Momentum $<P_t> = 0.3 - 0.5$ GeV/C | | |

On the basis of these features, the Feynman scaling hypothesis has been tested to gain some ideas about the essential feature of the dynamics governing the nature of hadronic interactions in the low $P_t$ domain. But once this domain has been passed to high $P_t$ domain from a transition region at 1.0 to 1.5 GeV/C, things are different as such none of the elements of the above table works, and then the aforementioned transition region must be the onset of a new hadronic interaction dynamics. This is enhanced by the following experimental facts.

(I.4a) $P_t$-Dependence of the Large $P_t$ Particle Production Spectra

Extrapolation of a proposed low-$P_t$ steep exponential decline to large $P_t$ spectra domain gives, say, a $\pi^o$ cross section at $P_t = 6$ GeV/C which is seven[31] orders of magnitude smaller than the observed actual amount at high energy and at the same $P_t$. This transverse momentum dependence of the invariant PP $\longrightarrow \pi^o x$ cross section at fixed large centre of mass angle $\theta_{cm} = 90^o$, and different fixed values of the ISR range of energy has been displayed on Fig. 13. The slower fall-off, comparing with low $P_t$, of the events with increasing $P_t$ at

fixed s has also been observed[30] for other particles in a PP ——— K$^{\pm}$, P, P$^-$X reaction at large angles, the result of which at y = 0, $\Theta_{cm}$ = 90° and S = 45 GeV/C can be seen in Fig. 14 where all of the cross sections are showing the same general shape with the exception that the kaons and nucleons cross sections do not have the steeper slope at small P$_t$ as do the π's .

This large P$_t$ type behaviour of the data at fixed s has also been confirmed by all other experimental groups.[32]

(I.4b)  S-Dependence of the Large P$_t$ Particle Production
        Spectra:  Empirical Fit Functions

Fig.15 shows the variation of the invariant cross section of π , which has been produced by a proton incident on a nucleon target (W) at FNAL[33], by increasing s at each P$_t$- value.  It is obviously seen that the cross section is increasing by increasing s at each fixed P$_t$, confirming that the output of high P$_t$ particles is several orders of magnitude higher than the extrapolation of the e$^{-bP_t}$ behaviour found at small P$_t$. The same effect has also been found[30] for charged pions as well as all other heavier particles (e.g.: K,N) at the ISR where at P$_t$ = 3.0 GeV/C and different energies the invariant cross sections of particles are found increasing by a factor of about 3.

However, s- and P$_t$-dependence of the single particle invariant cross sections at high energy, large angle data of π° of reference (31) have been fitted empirically to:

$$\int = A P_t^{-N} F(P_t/\sqrt{s}) \quad ; \quad A = 1.5 \pm 0.05 \quad N = 8.24 \pm 0.05$$

$$F(P_t/\sqrt{s}) = e^{-bP_t/\sqrt{s}} \quad ; \quad b = 26.10 \pm 0.05 \tag{I.16a}$$

which by including the associated systematical errors, the data agree with N = 8.  And if a mass term as large as M∼1 GeV is

included in (I.16a) for damping the behaviour at low $P_t$, above
fit reads as:

$$\frac{E d^3\sigma}{d^3p}(pp \quad \pi^0 x) \sim \frac{120 \, mb/Gev^2}{(P_\perp^2 + 1 \, Gev^2)^4} \, e^{-13 x_\perp} = g(P_\perp) f(x_\perp, \Theta_{cm} \sim 90^\circ) \tag{I.16b}$$

where $0.1 < x_\perp = \frac{P_\perp}{P_\perp^{max}} \sim \frac{2 P_\perp}{\sqrt{s}} < 0.4$ . Above the upper part of $x_t$, up
to 0.72, the measurements of the data have been available only
at FNAL[33] where this fit to the data of Fig. 15 reads the
following normalization:

$$\frac{E d^3\sigma}{d^3p} \sim s^{-n} f(x_\perp, \Theta_{cm} \sim 90^\circ)$$
$$\sim P_\perp^{-N} \bar{f}(x_\perp, \Theta_{cm}) \; ; \qquad \bar{f} = x_\perp^N f \qquad N = 2n \tag{I.17}$$

which gives a high value for $N (\sim 11.0 \pm 0.4)$. However, the
same experimental group has also used a hydrogen target giving
lower values of the parameter N, compatible with the ISR
results. The data indicate that the atomic number dependence of
the particle yields observed previously is also $P_t$ dependent
$\sim A^{\alpha(P_\perp)}$ . The values of $\alpha(P_t)$ are shown in Fig. 16 for $\pi^+$
and $\pi^-$ productions. In (I.17), the power of s is sensitive
to finite mass effect for low $x_t$, and for $x_L = 0$, and it must
be equal to zero in order to agree with Feynman scaling. However
at ISR where the target is a simple proton, the invariant cross
sections of all detected particles (pions, Kaons, or nucleons)
have been reported being[34] fitable to functions as in (I.16)
or (I.17) confirming $n \sim 4$. The fit to the $\pi^0$ and $\pi^+$ data are
further illustrated in Fig. 17 and 18 respectively. Here the
function of $\bar{f}(x_t, 0 \quad 90^\circ) \sim P_\perp^6 (\frac{E d^3\sigma}{d^3p})$ is displayed versus $x_t$
on each figure. Over the range of $x_t$ between 0.08 and 0.35.
$\bar{f}(x_t)$ in Fig. 17 is observed to decrease by a factor $\sim 20$ on
such parametrization of the type;

$$\bar{f}(x_\perp) = A' \exp(-B x_\perp) \tag{I.18}$$

with $A' = (14.8 \pm 0.6) \times 10^{-27}$ and $B = 12.6 \pm 0.2$ or

$$f(x_i) \sim c \, (1-x_i)^{m'} \qquad \qquad \text{(I.21)}$$

with $c = (12.9 \pm 0.6) \times 10^{-27}$ and $m' \sim 10.5 \pm 0.2$ giving the invariant cross section in $cm^2 c^3/GeV^2$. On the other hand, by consulting the straight line in Fig. 18 which is a fit to a much newer renormalized neutral pion data, one may hope that the data on charged pions probably are approaching the same scaling limit.

However above experimental results, within their accuracy, are confirming the factorization of the empirical fit formula as well as the stability of $n \sim 4$. Relying on experiments done at ISR we give some more features of large $P_t$ domain of charged particle production spectra in the next coming Table. To see the difference between two domains (low- and large-$P_t$) it is necessary to consult the previous Table as well as to know[30] that in large $P_t$ domain the fraction of the cross section for charged-particle-production (e.g.: $\left( E d^3\sigma/d^3p \right)_i / \sum_j \left( E d^3\sigma/d^3p \right)_j$, where i and j indicate the particle type), which goes into production of a given particle type when both signs are taken together, at a given $P_t$ is independent of energy, while in contrast the charges excess (i.e. the sum of the cross sections for positively charged particles minus the sum of the cross sections for negatively charged-particles divided by the sum of the cross sections for all charged particles) for a given $P_t$ depends on s, but for a given $x_t$ it is approximately independent of s. These two points can be seen in Figs. 19 and 20, respectively.

| Large $P_t$ Spectra | Behaviour | Particle Ratios |
|---|---|---|
| Dependence on increasing $P_t$ (at fixed s) | A slow inverse power law decrease | $\pi/K/N \sim 2/1/1$ <br><br> $\pi^+/\pi^- > 1$ in PP |
| Dependence on increasing s (at fixed $P_t$) | Strongly rising | collisions. |

Notice that: In General The Average Transverse Momentum
$< P_t > \sim 0.3 - 0.5$ GeV/C

## I.5 Conclusion

It is clear that in a certain stage, all experimental mechanisms are different developed ways of answering to a fundamental question of "what is the matter made of?". And a common feature of all these mechanisms is seen to be the probing of ever shorter distances which is synonymous with scattering beams of ever higher transfer of momentum to the target under study. In the other way round, one may say that the large momentum transfer events result from violent collisions of the elementary particles, and that in such collisions the internal structure of the particle is probed most deeply. This is first of all a classical idea as we know that a violent collision of them, breaks them open and then exposes the internal structure of the object. Secondly through quantum mechanical concepts, for instance: according to the uncertainty principle, a spatial structure as fine as $\Delta x$ can be detected only if:

$$\Delta p \gtrsim \frac{K}{\Delta x}$$

and when a right momentum transfer is chosen. However, trends of the data are showing that there must have been chosen such

a right transfer of momentum at large s, large angle hadronic reactions. Indeed occurrence of fixed angle features and absence of prominent fixed $|t|$ (or fixed $|\,|$) structure associated with hadron exchange mechanisms in two-body reaction data, and on the other hand, the violation of Feynman scaling at large $P_t$ inclusive reactions are all indicating above argument has been set on, and, further, they are then, a manifestation of a constituent structure of the scattering hadrons.

Here we have a case remarking the possibility of probing small transverse distances by a large transverse momentum, whose significance is in the same footing as that of the famous Rutherford[44] $\alpha$ - and $\beta$ - particles scattering experiment through which the structure of atom has been searched. In the next chapter we will show how far this hint of the data has resemblance and can be accepted.

# CHAPTER II

## Parton Model

### II.1 Introduction

Violent collisions of hadrons have shown that their corresponding data disobey the usual theoretical and experimental expectations valid at smaller $P_t$ (see first chapter), causing a hint that the hadrons may be constituted from some point entities. To see this more clearly, in what follows the data from violent collisions of a known point particle, a lepton, and a hadron will be looked into. In this way, easier by nature supplying the only four non-strongly interacting, hence, leptons: $\bar{e}, \nu_e, \bar{\mu}, \nu_\mu$ and their antiparticles which are all fermions with spin $\frac{1}{2}$. Neutral leptons i.e.: $\nu_e$ and $\nu_\mu$ interact only via weak interaction while the charged ones i.e. $\bar{e}$ and $\bar{\mu}$ have both electromagnetic and weak interactions.

However, our first hint of a deeper than atomic and nuclear underlying substructure of the matter, through consideration of deep inelastic scattering, comes from detailed systematical studies of hadronic spectroscopy suggesting that the substructure involves quarks with spin $\frac{1}{2}$ coming in three (or four) flavours with fractional charges. The point like nature of quark is exhibited by significance of scaling stating that "no more resolution of any structure within the quark can be made."

The solidity of each of the above remarks will be met within the contents of the Old Quark Model, namely the data below the charm threshhold which will be discussed

here. For this to be clear, some remarks including our usual idea about form factors will be touched on briefly in Section II.2 being followed by a brief discussion on classification of hadrons in Section II.3 in quark model relevant to the next coming subject, namely $eN$ inelastic scattering. This will first be treated kinematically allowing us to understand the relative data in Section II.4. The parton model will be given in Section II.5 which includes also relative discussion on $eN$ scattering. What can be expected from this model in interpreting the $\nu(\bar{\nu})N$ scattering can be found in Section II.6 which starts by some preliminary remarks on $\nu(\bar{\nu})N$ kinematics. This section also includes most of the sum rules discussed in literatures. To see how far the parton model ideaology is workable in the other fields, we present the lepton pair production in Section II.7.

## II.2 Elastic lN Scattering

### (II.2a) Introductory remarks and notations

In an electron scattering by an applied field A, taking it to be that of proton, which occurs through exchange of photons the characteristic strength of the interactions of the photons with the field is given by $\sqrt{\alpha} = \sqrt{e^2/\hbar c}$ where $\alpha$, the fine structure constant, is of order of $\frac{1}{137} \ll 1$. Since this coupling strength is very small, it is sensible to confront the experimental results with calculations (based on the Feynman graphs) to lowest order in $\alpha$.

When the beam of electrons scatter from a stationary proton target in the Lab frame;
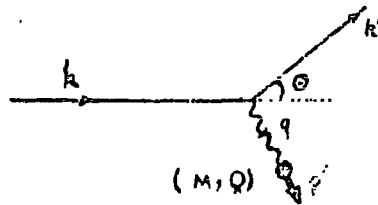
Diag.II.1: Electron-Nucleon scattering
in the Lab frame (nucleon at rest)

we have:

$$P = (M,Q) \; , \; k = (E, \underline{k}) \; , \; k' = (E', \underline{k'}) \; , \; P' = (P+q) \; , \; q = (k-k') \qquad \text{(II.1)}$$

Here $\Theta$ is the scattering angle. Now if electron mass effect is neglected then four-momentum squared of the virtual photon may be written as:

$$q^2 = (k-k')^2 \sim -2 k \cdot k'$$
$$= (P'-P)^2 \sim -2P \cdot P'$$
$$= -4 E E' \sin^2 \frac{\Theta}{2} \quad \longleftrightarrow \quad m \sim 0 \rightarrow E = k^0 \sim |\underline{k}| \quad \& \quad E' = k^{0'} \sim |\underline{k'}| \qquad \text{(II.2)}$$

Thus, for scattering, $q^2 \leq 0$ (i.e. spacelike photons). For convenience we define

$$q^2 = -Q^2 \qquad \text{(II.3)}$$

In Lab frame:

$$p \cdot q = M \qquad \text{(II.4)}$$

and since $P = (M,Q)$, then

$$\nu = q^0_{\text{lab}} = E-E' = Q^2/2M \qquad \text{(II.5)}$$

which is the energy loss to the recoiling hadronic system. Also with respect to Diag. II.1 we have:

$$M(E-E') = E E' (1-\cos \Theta) \qquad \text{(II.6)}$$

However, if an elastic scattering is concerned, then

$$(P + q)^2 = P'^2 = M^2 \qquad \text{(II.7)}$$

which leads to:

$$2M\nu = Q^2 \qquad \text{Elastic scattering} \qquad \text{(II.8)}$$

Thus, here, $\nu$ and $Q^2$ are not independent. For inelastic scattering to a system of invariant mass $W^2$

$$p'^2 = W^2 \qquad \text{Just fixed for each experiment} \qquad \text{(II.9)}$$

therefore:

$$M^2 + 2M\nu - Q^2 = W^2 \qquad \text{Inelastic Scattering} \qquad \text{(II.10)}$$

and of the three invariants $Q^2$, $\nu$ and $W^2$ only two are independent (M stands for the mass of proton).

(II.2b) <u>Unpolarized Scattering and the Rosenbluth Formula</u>

If $\sigma, \sigma', \lambda$ and $\lambda'$ are the spin projections of the electron and proton respectively, according to the usual Feynman rules the elastic scattering amplitude could be written down as:

$$A \sim e^2 < k', \sigma' | j_\mu(0) | k, \sigma > \frac{g_{\mu\nu}}{q^2} < p', \lambda' | j^\nu(0) | p, \lambda > \qquad \text{(II.11)}$$

Here, $g_{\mu\nu}/q^2$ is the photon propagator. For leptonic vertex function, which is just the matrix elements of the electromagnetic current operator $j_\mu(0)$ being evaluated at the origin in space-time $\left( j_\mu(x) = e^{-ikx} j_\mu(0) e^{ikx} \right)$, we may write:

$$< k', \sigma' | j_\mu(0) | k, \sigma > = \bar{u}(k', \sigma') \gamma_\mu u(k, \sigma) \qquad \text{(II.12)}$$

where u and $\bar{u}$ are the usual 4 component Dirac spinors and $\gamma_\mu$, the 4 x 4 gamma matrices.

For hadronic vertex, the two following types of targets may be considered:

(i) <u>If we suppose that the proton is a spin $\frac{1}{2}$, mass M structureless particle (like $\mu$)</u> then a similar form as the

leptonic vertex could be assigned to the hadronic one, as;

$$< P', \lambda' | j^{\nu}_{(0)} | P, \lambda > = \bar{u}(P', \lambda') \, \gamma_\mu \, u(P, \lambda) \qquad (II.13)$$

(ii) <u>If the target is actually a realistic proton</u> then the general form of the electromagnetic current taken between single proton states may look like:

$$< P', \lambda' | \delta_\nu(\bar{\omega}) | P, \lambda > = \bar{u}(P', \lambda') \, \Gamma_\nu \, u(P, \lambda) \qquad (II.14)$$

Here, $\Gamma_\nu$ covers any linear combinations of functions which are built up from P, P' and $\gamma$-matrices. The number of these functions may be reduced down (by using the Dirac equation for eliminating multiplicative scalar factors such as ($\gamma \cdot P$) or ($\gamma \cdot P'$)) to the three functions: $\gamma^\mu_\delta$, P = P + P'. and q = P' - P. For a precise form of $\Gamma_\nu$, each of these should be multiplied by a form factor $F(Q^2)$ due to the internal structure of the proton generating such a dynamical $Q^2$ dependence. Thus, if the current conservation requirement, $\partial_\mu \delta^\mu(x) = 0$, is notified, then:

$$\Gamma_\nu = \gamma_\nu \, ( F_1(q^2) + K \, F_2(q^2)) - \frac{(P+P')_\nu}{2M} \, K \, F_2(q^2) \qquad (II.15)$$

with the quantity K being the anomalous magnetic moment of the proton (= 1.79 Bohr magnetons).

<u>For the cross sections</u>, we may start from the transition matrix element;

$$S_{fi} = -i \int J^{(e)}_\mu(x) \, D_F(x-y) \, J^{(P)\nu}(y) \, dx \, dy \qquad (II.16)$$

where the Feynman propagator for electromagnetic radiation, $D_F(x-y)$, looks like:

$$D_F(x-y) = -(2\pi)^{-4} \int e^{-iq(x-y)} / (q^2 + i\epsilon) \, dq \qquad (II.17)$$

Then, the differential x-section could have the following form-

after translating the currents to the origin in space time—:

$$d6 \sim \frac{1}{Flux} \; \delta^4(k+p-k'-p') \; |A|^2 \; d(\text{Phase space})$$

$$\sim \frac{mM}{\sqrt{(k.p)^2 - m^2 M^2}} \; \delta^4(k+p-k'-p') \; |A|^2 \; \frac{m \, d^3 k'}{(2\pi)^3 \, E'} \; \frac{M \, d^3 p'}{(2\pi)^3 \, E'_{PROTON}} \qquad (II.18)$$

If no information regarding the polarization is sought, then the absolute square of the matrix element is to be averaged over the initial spin states and summed over the final ones. Now by making use of the completeness relation for positive energy spinors:

$$\sum_{6} u_\alpha(k,6) \, \bar{u}_\beta(k,6) = \left(\frac{\not{K}+m}{2m}\right)_{\alpha\beta} \equiv \left(\Lambda_+(k)\right)_{\alpha\beta} \; ; \; \not{K} := \gamma^\mu k_\mu \qquad (II.19)$$

and trace theorem, we present a general example to obtain the differential x-section: suppose;

$$\left|A_{fi}\right|^2 = \left|\bar{u}(f) \, \Gamma \, u(i)\right|^2 \equiv \left(\bar{u}(f) \Gamma u(i)\right)\left(\bar{u}(i) \bar{\Gamma} u(f)\right) \; ; \; \bar{\Gamma} = \gamma^0 \Gamma^\dagger \gamma^0 \qquad (II.20)$$

then:

$$\frac{1}{2}\sum_{f} A_{fi} = \frac{1}{2} \sum_{f} \bar{u}_\kappa(f) \left( \Gamma \frac{\not{q}'_i + r}{2r} \bar{\Gamma} \right)_{\alpha\beta} u_\beta(f)$$

$$= \frac{1}{2} Tr \left( \Gamma \frac{\not{q}'_i + r}{2r} \bar{\Gamma} \frac{\not{q}'_f + r}{2r} \right)$$

$$= \underbrace{\frac{1}{2r^2} \left( Q'^\mu_i Q'^\nu_f + Q'^\mu_f Q'^\nu_i - g_{\mu\nu}(Q'_i Q'_f - r^2) \right)}_{T^{\mu\nu}} \qquad (II.21)$$

Now if the same procedures apply to case (i) above, we get

$$|A|^2 = L_{\mu\nu} W^{\mu\nu} \qquad (II.22a)$$

where each of the leptonic, $L_{\mu\nu}$ , and hadronic, $W^{\mu\nu}$, tensors reads as;

$$L_{\mu\nu} = \frac{1}{4m^2} Tr \, (\not{K}'+m) \gamma_\mu (\not{K}+m) \gamma_\nu \Rightarrow \frac{1}{m^2} \left( k_\mu k'_\nu + k'_\mu k_\nu - g_{\mu\nu}(kk'-m^2) \right) \qquad (II.23a)$$

$$W^{\mu\nu} = \frac{1}{4M^2} Tr \, (\not{p}'+M) \gamma^\mu (\not{p}+M) \gamma^\nu \Rightarrow \frac{1}{M^2} \left( p^\mu p'^\nu + p'^\mu p^\nu - g^{\mu\nu}(pp'-M^2) \right) \qquad (II.23b)$$

In Lab where (II.1), (II.2) and (II.6) hold, (II.22a) reads as;

$$L_{\mu\nu} W^{\mu\nu} = \frac{2}{m^2} E E' \left( \cos^2 \frac{\theta}{2} - \frac{q^2}{2M^2} \sin^2 \frac{\theta}{2} \right) \tag{II.22b}$$

By introducing this into (II.18), after carrying out the phase-space integrals such that the electron would be allowed to emerge into a solid angle $d\Omega$, the result reads as:

$$\frac{d^2\sigma}{d\Omega dE'} = \frac{\alpha^2}{4E^2 \sin^4 \frac{\theta}{2}} \delta\left( \frac{Q^2}{2M} - \nu \right) \left( \cos^2 \frac{\theta}{2} + \frac{Q^2}{2M^2} \sin^2 \frac{\theta}{2} \right) \tag{II.24a}$$

where the $\delta$-function is for satisfying the conditions (II.8). By integrating over $dE'$, we get

$$\frac{d\sigma}{d\Omega} = \left( \frac{d\sigma}{d\Omega} \right)_{Mott} \left( 1 + 2\tau \tan^2 \frac{\theta}{2} \right) \quad ; \quad \tau := \frac{Q^2}{4M^2} \tag{II.24b}$$

where:

$$\left( \frac{d\sigma}{d\Omega} \right)_{Mott} = \frac{\alpha^2 \cos^2 \frac{\theta}{2}}{4E^2 \sin^2 \frac{\theta}{2} \left( 1 + \frac{2E}{M} \sin^2 \frac{\theta}{2} \right)} \quad \longleftarrow \quad E \ll M \tag{II.25}$$

Eq. (II.25) describes the scattering in a static Coulomb field, then the term in the bracket of (II.24b) is a correction to (II.25) arising from the magnetic interaction between the electron and the mass M structureless protons. When case (ii) is considered, $W^{\mu\nu}$ which reads now as:

$$W^{\mu\nu} = \frac{1}{4M^2} \text{Tr} \left( \not{p}' + M \right) \Gamma^\mu \left( \not{p} + M \right) \Gamma^\nu \tag{II.23c}$$

where with respect to (II.15), $\Gamma^\mu \equiv \gamma^\mu F_1(q^2) + \frac{\kappa F_2(q^2)}{2M} i \sigma_{\mu\alpha} q^\alpha$, causes to have the double differential x-section as:

$$\frac{d^2\sigma}{d\Omega dE'} = \frac{\alpha^2}{4E^2 \sin^4 \frac{\theta}{2}} \delta\left( \frac{Q^2}{2M} - \nu \right) \chi$$

$$\chi \left( \cos^2 \frac{\theta}{2} \left( F_2^2(q^2) + \frac{1-\tau}{1+\tau} \kappa F_2^2(q^2) \right) + 2\tau \left( F_1(q^2) + \kappa F_2(q^2) \right)^2 \sin^2 \frac{\theta}{2} \right) \tag{II.26a}$$

which by integrating over $d$ , we get:

$$\frac{d\sigma}{d\Omega} = \left( \frac{d\sigma}{d\Omega} \right)_{Mott} \left( \left( F_1(q^2) + \tau \kappa F_2^2(q^2) \right) + 2\tau \left( F_1(q^2) + \kappa F_2(q^2) \right)^2 \tan^2 \frac{\theta}{2} \right) \tag{II.26b}$$

For avoiding cross term $(F_1 F_2)$, one may re-write these ex-

pressions in terms of linear combinations of $F_1$ and $F_2$ defined by:

$$G_E(q^2) = F_1(q^2) - \tau K F_2(q^2) \quad ; \quad G_E(0) = 1 \qquad (II.27)$$

and

$$G_M(q^2) = F_1(q^2) + K F_2(q^2) \quad ; \quad G_M(0) = \mu = 1 + K \qquad (II.28)$$

These are called, respectively, electric - and magnetic - form factors in terms of which

$$\frac{d^2\sigma}{d\Omega dE'} = \frac{\alpha^2}{4E^2 \sin^4\frac{\theta}{2}} \delta\left(\frac{Q^2}{2M} - \nu\right) \left[\cos^2\frac{\theta}{2}\left(\frac{G_E^2 + \tau G_M^2}{1+\tau}\right) + 2\tau G_M^2 \sin^2\frac{\theta}{2}\right] \qquad (II.26a')$$

and

$$\frac{d\sigma}{d\Omega} = \left(\frac{d\sigma}{d\Omega}\right)_{Mott} \left(\frac{G_E^2 + \tau G_M^2}{1+\tau} + 2\tau G_M^2 \cdot \tan^2\frac{\theta}{2}\right) \qquad (II.26b')$$

This is known as the "Rosenbluth formula" which if primarily interests are in the high energy approximation; $s \gg M^2, s \gg |Q^2|$, then (II.26b') may be given as

$$\frac{d\sigma}{dQ^2} = \left(\frac{4\pi\alpha^2}{Q^4}\right)\left(\left(G_E^2 + \tau G_M^2\right)/(1+\tau)\right) \qquad (II.26b'')$$

(II.2c)   Some Predictions from Form Factors

$G_{E,M}$ satisfy the scaling[10] law;

$$G_E^p = \frac{G_M^p}{\mu_p} = \frac{G_M^n}{\mu_n} = G_D \qquad (II.29)$$

and the dipole form

$$G_D = \frac{1}{\left(1 + Q^2/\Lambda\right)^2} \quad ; \quad \Lambda = 0.71 \qquad (II.30)$$

$$0 \leqslant G_E^n \leqslant 0.1$$

This empirical fit in which $\mu_N$ stands for the static magnetic moment, has been useful for determining the $G_E$ up to $Q^2 \sim 4$ and $G_M$ up to more than $Q^2 \sim 20$. However, the trends of the data of $G_{E,M}^N$ (N for nucleon) in Fig. 21 appear to show $1/Q^4$ behaviour

which reads as $G(Q^2) \sim \frac{1}{Q^4}$ when $Q^2 \gg$ (experimental parameter $0.71 = \Lambda$) $(GeV/C)^2$.

$G(Q^2)$ may be considered as a measurement of the probability amplitude for, say, nucleus to remain a nucleus after absorbing a virtual photon carrying $Q^2$. This, on a plot of cross section against, say, $E_2 \equiv E'$ appears as elastic peak due to coherent elastic scattering from the nucleus (see Fig. 22). More loss of energy to discrete levels causes the appearance of the coherent excitation of nuclear resonances to the left of the elastic peak in Fig. 22. Now if we insist on increasing $Q^2$ such that $Q^2 \gg \Lambda$ (see eq. (II.30)), as the sharp fall off the probability amplitude (as fast as $1/Q^4$) ensures, the cross section dies away. This means, physically, the onset of another region where the preference of the nucleus to break up is satisfied. As a result of this is a large quasi-elastic peak at the far left end of Fig. 22 due to electron elastically scattering off the constituent nucleons within the nucleus. This quasi-elastic scattering occurs when $W = \frac{m}{M} = N$ where $N$ is the number of constituents to which scattering depends on only, $m$ the nucleus mass, and $M$ the proton or neutron mass. The area under this quasi elastic peak is related to the sum of the squared charges of the constituents.

Since $\Lambda_p < 1$, there exists a regime of $Q^2$ where the proton form factor takes over. Here is actually onset of the repetition of history by nucleons. And as we see later in this chapter there appears to be no more scaling in this region in where quarks are believed to be scattered.

## II.3    Hadrons' Quark Model

Gell-Mann and Zweig have stated[59,62] that the wide range of different particles have built up from just three types of

fundamental entity, the so called up, u, down, d, and strange, s, quarks each of which has spin $\frac{1}{2}$. They are characterized by isospin, I, and strange, S, quantum numbers. The u and d quarks have S=0 and are members of an I=$\frac{1}{2}$ doublet, while the s quark has I=0 and S=-1 (see the following table).

We know that hadrons are of two types: baryons (B=1), decaying radioactively leaving a proton or a neutron as their end result, and mesons (B=0). However, the relation $Q/e = I_3 + (B+S)/2$ - the Gell-Man/Nishigima formula - relates the charge, isospin and strangeness of baryons and mesons.

According to the following rule, the particle states are made out of quarks:

Baryons are built up from 3-quark contributions (qqq)

Mesons are built up from a quark-antiquark contribution ($q\bar{q}$) therefore the baryon number = $\frac{1}{3}$ to each q and = $-\frac{1}{3}$ to each $\bar{q}$ is assigned in the following table.

### Quark/Antiquark Quantum Numbers

| Quark Label | Spin J | B | I,$I_3$ | S | Charge Q/e | Anti Quark Label | Spin J | B | I,$I_3$ | S | Charge Q/e |
|---|---|---|---|---|---|---|---|---|---|---|---|
| u | $\frac{1}{2}$ | $\frac{1}{3}$ | $\frac{1}{2},\frac{1}{2}$ | 0 | $+\frac{2}{3}$ | $\bar{u}$ | $\frac{1}{2}$ | $-\frac{1}{3}$ | $\frac{1}{2},-\frac{1}{2}$ | 0 | $-\frac{2}{3}$ |
| d | $\frac{1}{2}$ | $\frac{1}{3}$ | $\frac{1}{2},-\frac{1}{2}$ | 0 | $-\frac{1}{3}$ | $\bar{d}$ | $\frac{1}{2}$ | $-\frac{1}{3}$ | $\frac{1}{2},\frac{1}{2}$ | 0 | $+\frac{1}{3}$ |
| s | $\frac{1}{2}$ | $\frac{1}{3}$ | 0,0 | -1 | $-\frac{1}{3}$ | $\bar{s}$ | $\frac{1}{2}$ | $-\frac{1}{3}$ | 0,0 | +1 | $+\frac{1}{3}$ |

For the baryons, the different 3-quark combinations may be grouped into multiplets, consisting of octets and decuplets of states with a particular spin and parity, $J^P$, and a well-defined symmetry with respect to interchange of quark labels, spin and space coordinates.

As an example, we recall the quark model family description of proton (P) and neutron (n). Members of this family have S = 0 and form an isospin doublet, the $I=\frac{1}{2}$ nucleon (N). Still they are members of a bigger family called octet of baryon states of $J^P = \frac{1}{2}^+$, in which the three quarks are in a relative S-state (1=0), with two spin parallel and one antiparallel. For the nucleon only u and d quarks are involved; a proton consisting of the combination uud and a neutron, ddu. This octet together with quark labelling is given as:
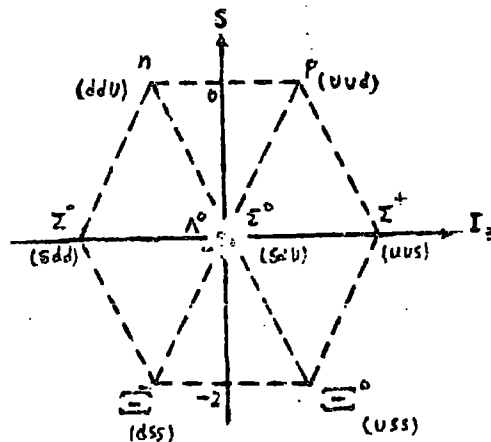


Diag.II.2: Schematic diagram of the octet of baryons of spin-parity

## II.4 Electromagnetic Deep Inelastic lN scattering

(II.4a) Inelastic eN kinematics

By assuming one photon exchange for the reaction $1 + N \longrightarrow 1' +$ hadrons the amplitude;
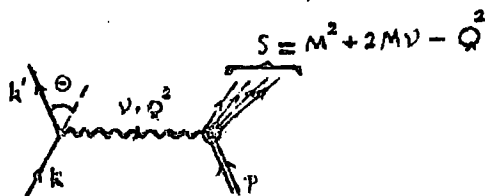


Diag.II.3: Inelastic electron-proton scattering via one photon exchange

factorizes as:

$$A \sim e^2 \, \bar{U}(k',s') \, \gamma_\mu \, u(k,s) \, \frac{1}{q^2} \, <r';n|J^\mu(o)|r> \qquad (II.31)$$

by taking $|A|^2$ and summing over the hadronic states, n:

$$d\sigma \sim L_{\mu\nu} W^{\mu\nu} (P,q) \qquad \text{(II.32)}$$

If no polarization is sought, then, $L_{\mu\nu}$, is the same as (II.23a) while $W^{\mu\nu}$ now may be written as:

$$W^{\mu\nu}(P,q) = \frac{1}{2}\sum_{S}\sum_{n} <PS|J^{\mu}_{(o)}|n> <n|J^{\nu}_{(o)}|PS> (2\pi)^3 \delta^4 (P+q-P_n) \qquad \text{(II.33a)}$$

where 4-momentum $\delta$-function is included since there is no restriction on the energy of the scattered electron from its scattering angle. P, q, and metric tensors can only form two combinations which satisfy the current conservation, $q_{\mu} W^{\mu\nu} = q_{\nu} W^{\mu\nu} = 0$, and symmetry property, $W^{\mu\nu} = W^{\nu\mu}$, requirements, such that:

$$W^{\mu\nu}(P,q) = \left(-g^{\mu\nu} + \frac{q^{\mu}q^{\nu}}{q^2}\right) W^{em}_1 (\nu,q^2) + \left(\left(P^{\mu} - \frac{P\cdot q}{q^2} q^{\mu}\right)\left(P^{\nu} - \frac{P\cdot q}{q^2} q^{\nu}\right)\right) \frac{W^{em}_2 (\nu,Q^2)}{M^2} \qquad \text{(II.33b)}$$

Upon constructing this and (II.23a) the result after neglecting leptonic mass at high energies reads (in Lab frame) as:

$$L_{\mu\nu} W^{\mu\nu} = 2 E E' \left(2 W^{em}_1 (\nu,q^2) \sin^2\frac{\theta}{2} + W^{em}_2 (\nu,Q^2) \cos^2\frac{\theta}{2}\right) \qquad \text{(II.34)}$$

which by introducing it into (II.32), the differential cross sections for the final electron, with energy in the range of dE', to emerge into $d\Omega'$ reads as:

$$\frac{d^2\sigma}{dQ^2 d\nu} = \frac{4\alpha^2 E^2}{Q^4} \left(W^{em}_2 (\nu,q^2) \cos^2\frac{\theta}{2} + 2 W^{em}_1 (\nu,Q^2) \sin^2\frac{\theta}{2}\right) \qquad \text{(II.35a)}$$

(This would be the Rosenbluth equation when $\nu = \frac{Q^2}{2M}$ )

alternatively it may read as:

$$\frac{d^2\sigma}{dQ^2 d\nu} = \frac{4\pi\alpha^2}{Q^4} \frac{E'}{ME} \left(W^{em}_2 (\nu,q^2) \cos^2\frac{\theta}{2} + 2 W^{em}_1 (\nu,Q^2) \sin^2\frac{\theta}{2}\right) \qquad \text{(II.35b)}$$

However by comparing with (II.26a), the forms that $W_{1,2}$ can take for the elastic scattering read as:

$$W_1^{el}(\nu, Q^2) = \tau \, G_M^2(Q^2) \, \delta\left(\frac{Q^2}{2M} - \nu\right) \tag{II.36a}$$

$$W_2^{el}(\nu, Q^2) = \frac{G_E^2(Q^2) + \tau \, G_M^2(Q^2)}{1 + \tau} \, \delta\left(\frac{Q^2}{2M} - \nu\right) \tag{II.36b}$$

while, by comparing with (II.24a), for elastic scattering from a spin $\frac{1}{2}$ pointlike coupling $W_{1,2}$ read as:

$$W_1^{Pt}(\nu, Q^2) = \tau \, \delta\left(\frac{Q^2}{2M} - \nu\right) \tag{II.37a}$$

$$W_2^{Pt}(\nu, Q^2) = \delta\left(\frac{Q^2}{2M} - \nu\right) \tag{II.37b}$$

The structure functions, $W_{1,2}^{em}(\nu, Q^2)$, which summarize our lack of knowledge of the dynamics in the vertex $\gamma, P \longrightarrow$ hadrons, depend on $q^2$ and $q.P = M\nu$.

$W^{\mu\nu}$ is the contribution from the hadronic vertex, therefore another way of looking at our scattering is by treating the electron beam as a "source" of a beam of photons whose mass and energy can be tuned by varying the energy and scattering angle of the electron. We are then studying total photo-absorption cross sections as a function of energy and mass of the photon. However, it can be shown that the inelastic lepton-nucleon cross section in terms of the photoabsorption cross sections, $\sigma_T$ and $\sigma_L$, reads as:

$$\frac{d^2\sigma}{d\Omega dE'} = \Gamma_T \left(\sigma_T + \epsilon \sigma_L\right) \tag{II.35c}$$

with

$$\Gamma_T = \text{The Transverse Virtual Phototon Flux} = \frac{k\alpha}{2\pi^2 Q^2} \frac{E'}{E} \frac{1}{1 - \epsilon} \tag{II.38}$$

However, the relative size of contributions from a transverse photon and a longitudinal photon to the cross section is given by:

$$R = \frac{\sigma_L}{\sigma_T} = \frac{W_2^{em}}{W_1^{em}} \left(1 + \frac{\nu^2}{Q^2}\right) - 1 \tag{II.39}$$

(II.4b) <u>Deep Inelastic Scattering Data:  Scaling</u>

The data[45] in deep inelastic region looks like that of e-p in Fig. 23 which is reminiscent of our previous discussion concerning Fig. 22 as well as proving that if we had had a nucleus target, then, since:

$$Q^2_2 \gg \Lambda_{Proton} \gg Q^2_1 \gg \Lambda_{Nucleus} \qquad (II.40)$$

a new regime of $Q^2$ has been reached as a result of which the scattering on nuclear target can not be in deep continuum region.  In this way, Fig. 24 shows that at fixed missing mass $W \geqslant 2$ GeV the cross section falls off roughly like $\frac{1}{Q^2}$ and not like $\frac{1}{Q^8}$ (the nucleon form factor squared) which means whatever has been met inside the proton by our highly virtualized photon does not show any structure.  The other point is that:  from integrating the spectrum over $\nu$ at fixed $Q^2$ a large value for cross section has been obtained which is the same order of magnitude of the Mott cross section.  But first of all as long as fast fall off the proton form factors is regarded as an effect of the structure of the proton due to strong interaction (otherwise it should have remained at unity for all $Q^2$) it is impossible to have a point proton.  Secondly, the obtained large value of the cross section must be due to electrons scattering off the point like constituents within the proton.  Up to now there has not been found another $Q^2_3$ regime for the far end left of (II.40).  This means no observation of the constituents of proton.  However, a conjecture which is known being made by Bjorken[46]; i.e.:

$$\underset{Q^2,\nu\to\infty}{\mathscr{Lim}} \nu W^{em}_2 (Q^2,\nu) \longrightarrow F_2 \left(\frac{2M\nu}{Q^2}\right)$$

$$\underset{Q^2,\nu\to\infty}{\mathscr{Lim}} 2M W^{em}_1 (Q^2,\nu) \longrightarrow F_1 \left(\frac{2M\nu}{Q^2}\right) \qquad ; \quad \frac{2M\nu}{Q^2} = \cdots = x^{-1} \qquad (II.41s)$$

is a way of gaining information about proton governing dynamics.

This "scaling" or "scale invariance" arises very naturally in a model which accepts proton as being made of pointlike constituents or partons (see next section). To see this we have to measure the cross section at various $\theta$ for the same values of $Q^2$ and $\nu$ in deep continuum, then extracting $W_1^{em}(then\ \sigma_T)$, at large angle, and $W_2^{em}(then\ \sigma_L)$ at small $\theta$. However, relying on

$$\frac{\nu W_2}{W_1} = (1+R)\left( 1 \Big/ (\frac{1}{\nu} + \frac{\nu}{Q^2}) \right) \qquad (II.42)$$

we see that if R has the proper functional form to make right-hand sides of the equation function of the dimensionless variable $\omega$ then, scaling of $\nu W_2$ and $W_1$ will mutually occur. So if we have $\sigma_T$ and $\sigma_L$ separated experimentally, then judging about R gets easier. Fig. 25a shows[47] determination of $\sigma_T$-- and $\sigma_L$- data -- trends of which are in consistent with the underneath assumption of one photon exchange in the definition of the electromagnetic structure function implying the linear dependence of $\left( (d^2\sigma/d\Omega d\epsilon')/\Gamma_T \right)$ on $\epsilon$ for a particular point $(Q^2, \nu)$ (here $Q^2$ varies from 1.0 to 11.0 GeV$^2$ and $\omega$ from 2.6 to 4.0 GeV). The measured values of R are in the range 0 to 0.5 which on the assumption of it being roughly constant in this kinematic range, the proton average value of R is $0.18 \pm 0.10$. In Fig. 25b the measured R is shown as a function of W implying no clear dependence of R on any kinematic variable. The smallness of R causes to accept it, only conveniently, equal to zero as it is the case in presenting scaling of $\nu W_2$ and $2MW_1$ in Fig. 26a which shows appropriate data[48] well beyond the prominent resonance regions i.e. with cuts of $Q^2 > 1$ GeV$^2$ and $W^2 > 4$ GeV$^2$.

(II.4c) <u>Precocious Scaling; Scaling Violation;</u>

Relation (II.41) will not hold in the resonance region where there are enhancement at particular values of W, nor for

small $Q^2$, since $\nu W_2(W, Q^2 \to 0) \to 0$. But by the following dimensionless variable for which the lower limit goes down to $W \gtrsim 1.8$ GeV and $Q^2 \gtrsim 1$ GeV$^2$:

$$\omega' = \omega + \frac{M^2}{Q^2} \to \omega \text{ in Bjorken limit} \qquad (II.43)$$

Bloom and Gelman[49] have shown that the low energy resonance electroproductions have a behaviour which is correlated with that of the deep inelastic scattering. This has been tested in terms of a constant $Q^2$ finite energy sum rule (rooted on getting the scaling hold for all $\omega'$ as long as $Q^2 \to 1$ when interchangability of the Regge - $\nu \to \infty$ , fixed $Q^2$ - and Bjorken - $\nu$ and $Q^2 \to \infty, \frac{\nu}{Q^2}$ fixed - limits is assumed):

$$\frac{2M}{Q^2} \int_0^{\nu_{max}} d\nu \; \nu W_2 (\nu, Q^2) = \int_1^{1 + W_{max}^2/Q^2} d\omega' \; F_2(\omega') \qquad (II.49)$$

where $W_{max}$ is in the scaling region and $\nu_{max}$ is given by: $\nu_{max} = (W_{max}^2 - M^2 - Q^2)/2M$. For a range of $Q^2$ from 1 to 4 GeV$^2$ and for $W_{max}$ from 2.2 to 2.5 GeV interpolating the experimental values at fixed $Q^2$ in Fig. 26b indicates that the evaluation of this sum rule is satiafied.

While plotting of the data in $\omega'$ extends the scaling to smaller value of $W^2$, by introducing a variable[50] such as:

$$\omega_W = \frac{2M(\nu + m_\rho)}{Q^2 + m_\rho^2} \Rightarrow \omega \text{ or } \omega' \leftrightarrow Q^2 \gg m_\rho^2 \qquad (II.50)$$

scaling at large $Q^2$ will be obtained. And for $Q^2 \ll m_\rho^2$ it has been found that the function $\frac{\omega}{\omega_W} \nu W_2$ exhibits scale invariance even down to $Q^2 = 0$ (see Fig. 26c).

However, by making our attention restricted to data below threshhold for production of heavy hadronic degree of freedom such as charm, in this introductory remarks we, then, are not going to be concerned with the renormalizable field theories

which give a complete explanation of the behaviour of the data such as those shown[51] in Fig. 26d exhibiting quite a vast scaling violation for nucleon structure functions in meson deep inelastic scattering at 100 and 150 GeV.

(II.4d)  Data on scaling in neutron

Determinations of the neutron cross section from proton cross section has been done through[52] subtracting the proton cross section from deutron cross section. However, because in a ratio measurement many sources of errors (e.g. solid angle uncertainties, radiation corrections) tends to cancel out, determination of $\sigma_n/\sigma_p$ is mostly preferred over $\sigma_n$ alone, as is the case in the presentation of the data on Fig. 27a versus x' where, although $\sigma_n$ and $\sigma_p$ ratios are consistent with a single function of $\omega'$ i.e.: $\sigma_n$ exhibits scaling but significant difference between them ( hence, $\nu W_2^n \neq \nu W_2^p$ , say) is seen over the entire kinematic range shown, and thus provide evidence for a significant nondiffractive component in the scattering process. This is seen confirmed in Fig. 27b where $\nu (W_2^p - W_2^n)$ versus x' for $Q^2 > 0.9$ GeV$^2$, W > 1.8 GeV, and assuming $R_p = R_n$, represents a peak at $x' \sim 0.3$. The curve goes to zero at $x' = 1$ and $x' = 0$. These two points confirm $\sigma(\gamma p) - \sigma(\gamma n) \to 0$ at large $\nu$ .

II.5  A Model and Predictions From It

(II.5a)  The Parton Model

Eq. (II.35) with respect to (II.41a) and $y = \frac{\nu}{E}$ reads as:

$$ME \frac{d^2\sigma}{d\omega dy} = \frac{2\pi\alpha^2}{y^2} \left( F_2(\omega) (1-y) + F_1(\omega) y^2 \omega^{-1} \right)$$

(II.35c)

There is no fixed dimensional parameter on the right-hand side. Therefore, deep inelastic electron scattering is independent of any scale of length. Meaning that the nucleon's structure responsible for scattering must be pointlike in character

leading to the idea that the nucleon is composed of pointlike
constituents - the partons. This will be discussed more in the
(kindergarten) parton model[53] as follows:

In this model the role of impulse approximation is
apparent; such as demanding the parton being scattered off by
a sufficiently large momentum transfer, $Q^2$, allowing to con-
sider the scattering as:
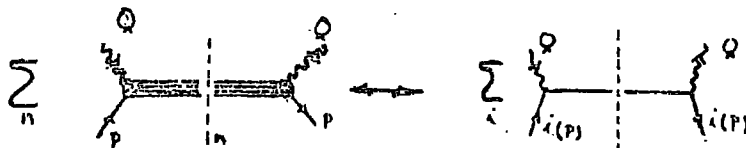


Diag.II.4: Equivalence of sum over
intermediate states and incoherent summation of
scattering from individual constituents of the
proton in deep inelastic electron-proton scattering

That is the nucleon is thought as consisting of partons, very
much the same as nucleus which is composed of nucleons. But
the main difference between the two is that a nucleus is rather
lightly bounded meaning that the nucleons are nearly real
particles, while by studying the ratio of binding energy to the
rest energy of the partons in a proton;

$$\frac{\text{binding energy}}{\text{rest energy}} \sim \frac{100\text{'s MeV}}{100\text{'s MeV}} \sim 1$$

we see that partons are tightly bounded inside the nucleon and,
so, are highly virtual (hence, changing their character from one
Lorantz frame to another). Apart from the binding energy, there
is one more frame dependent notion; namely "the lifetime, T,
of the parton" which should be greater than the time of inter-
action, $\tau$ , between a sudden pulse carrying a large energy
transfer from the projectile and the parton" if the impulse
approximation has to work. Because in the hadronic systems, the

time scale governing internal motion is comparable to the light
transit time, therefore internal motions is comparable to the
light transit time, therefore only a fuzzy picture of the
instantaneous states of the hadron seems obtainable.  However,
the solution is to have our hadron in a frame in which it can
move with nearly the speed of light in, say z-direction.  In
such a frame (which is, at high energies, the overall centre-of-
mass system) the Einstein time dilation effect diforms the
proton into a pancake (i.e. it suffers longitudinal contraction)
and slows the internal motions of the partons to a standstill
position.  Now "seeing" a scattered parton speeding away freely
from the interaction of the rest, in a relatively transverse
direction, seems probable if a sudden pulse propagating in the
transverse direction with a large transverse momentum hits it
elastically, i.e.:
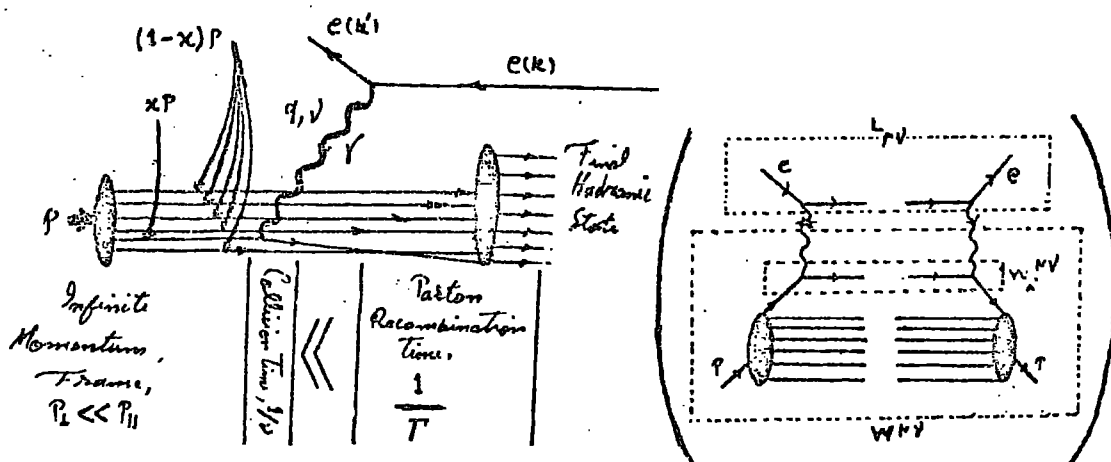


Diag.II.5:   Inelastic electron-proton
scattering in the parton model.  The proton breaks
up into constituent partons, only one of which
collides elastically with the leptons
(contributing $w_i^{\mu\nu}$ for the $i^{th}$ parton)

In brief, conditions are realizable as:

$$P^{\mu}_{parton,i} \cong x_i \cdot P^{\mu} \qquad ; \qquad \sum_i x_i = 1 \tag{II.51}$$

where $x_i$ is the finite fraction of the infinite momentum which
each ($i^{th}$) parton has when it is viewed in infinite momentum

frame if the partons in the rest frame of the nucleon are
limited in the magnitude of their momentum. Moreover, viewed
from overall centre-of-mass frame (see above for this approxi-
mation) the T and $\tau$ are of order, respectively;

$$T \simeq (\Delta E)^{-1} = \sum_i E_i - E \simeq 2P \Big/ \Big(\sum_i \big((k^2 + m_i^2)/x_i\big) - M^2\Big) \tag{II.52}$$

$$\tau \simeq q_o^{-1} \simeq 4P/(2M\nu - Q^2) \tag{II.53}$$

Thus provided that

$$2M\nu - Q^2 = 2M\nu \Big(1 - \frac{1}{\omega}\Big) \gg \sum_i \big((k_{\perp i}^2 + m_i^2)/x_i\big) - M^2 \tag{II.54}$$

we have $T \gg \tau$ . But (II.54) is satisfied if $2M_N\nu$ and $Q^2$ are
much greater than any transverse momentum - or mass - squared
with their ratio, $\omega = \dfrac{2M\nu}{Q^2}$ , fixed. Consequently the fraction
of the longitudinal momentum carried by the scattered parton
in the infinite momentum frame has to equal the scale variable
$\omega^{-1}$ with respect to which we may write:

$$P^o_{parton,i} \simeq \Big(xP + \frac{m_i^2 + k_{\perp i}^2}{2xP} + \frac{2M\nu - Q^2}{4P} + \frac{k_{\perp i}Q_\perp}{xP}\Big) \sim P_i^\nu + Q^o \tag{II.55}$$

which means the four momentum is conserved across the photon-
parton vertex.

However, we employ above ideas in inelastic lepton-nucleon
scattering as follows.

## (II.5b) Parton Model Predictions About the Deep Inelastic e-P Scattering

With respect to previous discussion, the deep inelastic
e-P scattering may be presented as:

$$W_{1,2}^{em}(\nu,Q^2) = \sum_i W_{1,2}^{el(i)}(\nu,q^2) \tag{II.56}$$

Contribution of each parton, carrying charge $e_i$, to each of the
electromagnetic structure functions is given by:

$$W_1^{el(i)} = \tau \, e_i^2 \, \delta \left( \frac{Q^2}{2m} - \nu \right) \tag{II.37a'}$$

$$W_2^{el(i)} = e_i^2 \, \delta \left( \frac{Q^2}{2m} - \nu \right) \tag{II.37b'}$$

where m = xM is the parton mass. Now if the probability of the existence of $i^{th}$ parton between xM and (x + dx)M masses is $f_i(x)$, then it may be shown that (II.72) reads as:

$$MW_1^{em}(\nu, Q^2) \longrightarrow \frac{1}{2} \sum_i f_i(x) \, e_i^2 \equiv F_1(x) \tag{II.57a}$$

$$\nu W_1^{em}(\nu, Q^2) \longrightarrow \sum_i x \, f_i(x) \, e_i^2 \equiv F_2(x) \tag{II.57b}$$

These remind us (II.41a) meaning the Bjorken deep inelastic limiting region satisfies the conditions for applying an impulse approximation to electron scattering from partons as viewed from infinite momentum frame, or vice versa (see Fig. 26a). From comparing these equations we get the following relation[54]:

$$2 x \, F_1(x) = F_2(x) = \sum_i x \, f_i(x) \, e_i^2 \tag{II.58}$$

In generalized parton model, however, if $P_N$ stands for the probability of N existing partons inside the proton, each with different distribution in $x$; i.e. $f_N(x_i)$ such that;

$$\int_0^1 f_N(x_i) \, dx_i = 1 \tag{II.59}$$

then (II.57b), for example, reads as:

$$\nu W_2(\nu, Q^2) = \nu \sum_{N=1}^{\infty} P_N \sum_{i=1}^{N} e_i^2 \int_0^1 dx_i \, f_N(x_i) \, \delta(\nu - Q^2/2M\nu)$$

$$= \sum_N P_N \sum_i x \, e_i^2 \, f_N(x) \bigg|_{x = Q^2/2M\nu}$$

$$= F_2(x = Q^2/2M\nu = \omega^{-1}) \quad ; \quad \sum_{N=1}^{\infty} P_N = 1 \tag{II.57b'}$$

and the assumption of having the same longitudinal momentum distribution for all partons becomes:

$$< x_i > = \int_0^1 x_i \, f_{iN}(x_i) \, dx_i = \frac{1}{N}$$

(II.60)

### (II.5c) Partons as Quarks; Sum rules; Duality

Equations (II.57) lead us to: $W_2^{em}/W_1^{em} = \frac{Q^2}{\nu^2}$ which by inserting this result into (II.39) we get:

$$R = \frac{\sigma_L}{\sigma_T} = \frac{W_2}{W_1}\left(1 + \frac{\nu^2}{Q^2}\right) - 1 = \frac{Q^2}{\nu^2} \equiv \frac{4M^2}{Q^2\omega^2}$$

(II.39a)

But from Fig. 25b suggestion of $R(\sigma_L) \to 0$ in the limitation of either $Q^2 \longrightarrow \infty$, $\nu$ fixed or $\nu \longrightarrow \infty$, $Q^2$ fixed is consistent with having our partons as spin $\frac{1}{2}$ objects. Because[55] by looking at the virtual photon (current)-parton interaction in their Breit frame, the improbability of a transverse current (with helicity $\pm 1$) to be absorbed by a spin-0 parton comes from its inability to carry any angular momentum in or out along the direction of current. Hence, $\sigma_L = 0 \Rightarrow R \to \infty$, in manifest disagreement with the data, meaning little of the proton's charge is carried by spin zero partons as far as $R \ne 0$ but very small. On this basis, partons are accepted as quarks of Gell-Mann and Zweig.

However, with respect to (II.59) and $-\frac{dx}{x} = \frac{d\nu}{\nu}$, eq. (II.57b') may be written as:

$$Z = \int_0^\infty W_2(\nu, Q^2) \, d\nu = \int_0^1 \frac{1}{x} F_2(x) \, dx = \sum_N \rho_N \left( \sum_i e_i^2 \right)$$

(II.61)

= expected value of the sum of the squares of all the parton's charges in the nucleon.

In this sum rule[56], the left hand side integral diverges logarithmically if the constant part of the (large $\nu$, finite $Q^2$) experimental value of $\nu W_2$ is not excluded. This constant

part of the (diffractive) virtual photon-nucleon scattering is
believed (at high energies) to be due to the isoscalar Pomeron
exchange term in the t-channel which is dual to the non-
resonant background in the direct s-channel (at low energies).
However, to avoid the logarithmic divergence we should only
consider the non-constant part of the (nondiffractive) virtual
photon-nucleon scattering corresponding (at high energies) to
the ordinary exchange terms in the t-channel which are dual to
the direct channel resonances (at low energies). Therefore in

$$\int_0^1 \frac{dx}{x} \left( F_2^P(x) - F_2^n(x) \right) = \sum_N \ell_N \left( \sum_{i,P}^N e_i^2 - \sum_{i,n}^N e_i^2 \right) \qquad (II.62a)$$

we do not confront with any divergence difficulties. To see
this in the context of the quark model we recall that according
to this model proton and neutron each consists of three quarks
which are supposed to be associated with the nonconstant part of
the virtual photon-nucleon scattering. As these valence quarks

contribute differently to eP and en scattering, then, they cannot
describe the constant part of scattering. To have this constant
part described it is assumed[57] that proton and neutron each
also consist of neutral quark-antiquark pairs which are assoc-
iated with the aforementioned constant part. However, provided
that the $q\bar{q}$ pairs possess zero net strangeness, baryon number,
and isospin, their combined effect will be zero as far as the
hadron multiplets are concerned.

To get the result of (II.62d), by recalling (II.58) with "i"
now standing for the quark flavour, we define;

$$f_u(x) = u(x) = \text{No. of up quark with momentum}$$
$$x \text{ to } x + dx \text{ in, say, the}$$
$$\text{proton} = u^P$$

$$= \text{No. of down quarks with momentum}$$
$$x \text{ to } x + dx \text{ in, say, neutron (by}$$
$$\text{isospin reflection)} = d^n$$

$$= u \qquad (II.63)$$

Now, to use (II.74) it should be noted that the virtual photon can hit anyone of the three types of quarks or antiquarks then:

$$\frac{1}{x} F^{\gamma p} = \frac{4}{9} (u + \bar{u}) + \frac{1}{9} (d + \bar{d}) + \frac{1}{9} (s + \bar{s}) \tag{II.64a}$$

$$\frac{1}{x} F^{\gamma n} = \frac{4}{9} (d + \bar{d}) + \frac{1}{9} (u + \bar{u}) + \frac{1}{9} (s + \bar{s}) \tag{II.64b}$$

As it is seen there are six terms for each structure function. On the other hand to get the net number of each kind of quarks we proceed as follows: the total charge on, say, a proton is +1, then;

$$1 = \frac{1}{3} \int_0^1 \left( 2(u - \bar{u}) - (d - \bar{d}) - (s - \bar{s}) \right) dx$$

and as $I^P = + 1/2$ , then;

$$\frac{1}{2} = \frac{1}{2} \int_0^1 \left( (u - \bar{u}) - (d - \bar{d}) \right) dx$$

also $S^P = 0$, so:

$$0 = \int_0^1 (s - \bar{s}) dx$$

The solutions result in:

$$\int_0^1 (u - \bar{u}) dx = 2 \tag{II.65a}$$

$$\int_0^1 (d - \bar{d}) dx = 1 \tag{II.65b}$$

$$\int_0^1 (s - \bar{s}) dx = 0 \tag{II.65c}$$

However, by using the duality requirement[57];

$$q(x) = V^q(x) + S^q(x) \qquad ; \quad V^S = 0 \tag{II.66a}$$

$$\bar{q}(x) = S^{\bar{q}}(x) \tag{II.66b}$$

and noting that the sea is supposed to have zero isospin and be even under charge conjugation,

$$S^u = S^d = S^{\bar{u}} = S^{\bar{d}} = S^s = S^{\bar{s}} = S(x) \tag{II.66b'}$$

(II.65) may read as:

$$\int_0^1 V^u(x)\,dx = 2 \qquad\qquad\qquad (II.65a')$$

$$\int_0^1 V^d(x)\,dx = 1 \qquad\qquad\qquad (II.65b')$$

On the other hand, after subtracting (II.64b) from (II.64a) with respect to (II.66) the result looks like the following:

$$\frac{1}{x}\left(F_2^{ep}(x) - F_2^{en}(x)\right) = \frac{1}{3}(V^u - V^d)$$

whose integration with respect to x and equations (II.65a') and (II.65b') read as:

$$\int_0^1 \frac{1}{x}(F_2^{ep}(x) - F_2^{en}(x))\,dx = \frac{1}{3} \equiv \overline{\sum_i}\left((e_i^2)_p - (e_i^2)_n\right) ; \sum_{N=1}^{\infty} P_N = 1 \qquad (II.62b')$$

This sum rule is compatible with the data in Fig. 27b and yields[52] 0.28.

Now if $V^u$ and $V^d$ have the same functional shape, then eqs. (II.65a') and (II.65b') demand that:

$$V^u(x) = 2 V^d(x) := 2V(x) \qquad\qquad\qquad (II.67)$$

with respect to which the curve of Fig. 27b' is $F_2^{ep} - F_2^{en} = \frac{1}{3} V$. But;

$$F_2^{eP} = V + \text{contribution from the sea} \qquad\qquad (II.68)$$

which is plotted in the lower part of Fig. 27b' where the difference between this curve and the data quoted on the figure is the contribution from the sea (which is negative). This means that (II.67) must break down at least near x = 1 where by taking the data literally, $V^d(x)$ is very much less than $V^u(x)$ and, hence, V quarks, here, are doing nearly all the scattering. Also adjustment of the curve to data near x = 1 shows a nearly zero contribution of the sea there and it could not become important until $x \leqslant 0.4$. That is to say that the "wee" partons

having fairly small fractional longitudinal momentum give the sea contribution going towards a constant value as x gets smaller, corresponding to Pomeron exchange.

Eq. (II.57b') with respect to $-dx = \frac{Q^2}{2M}\frac{d\nu}{\nu^2}$ and (II.60) can be integrated as:

$$\frac{Q^2}{2M}\int_0^1 \frac{1}{\nu} W_2(\nu,Q^2)\,d\nu = \int_0^1 F_2(x)\,dx = \sum_{N=1}^{\infty} \theta_N \left(\frac{\sum_{i=1}^N e_i^2}{N}\right) \qquad (II.69a)$$

= Mean-square charge
per parton

Experimentally[58], the SLAC/MIT data for the left hand side of this equation give the following results:

$$\int_0^1 F_2^{\gamma p}(x)\,dx = 0.16 \pm 0.02 \qquad \int_0^1 F_2^{\gamma n}(x)\,dx = 0.12 \pm 0.02 \qquad (II.69b)$$

Considering the nucleon as made up of three quark-partons, the right-hand-side of (II.69a) predicts that:

$$\int_0^1 F_2^{\gamma p}(x)\,dx = \left(2\left(\tfrac{2}{3}\right)^2 + \left(\tfrac{-1}{3}\right)^2\right)\Big/ 3 \qquad \int_0^1 F_2^{\gamma n}(x)\,dx = \left(\left(\tfrac{2}{3}\right)^2 + 2\left(\tfrac{-1}{3}\right)^2\right)\Big/ 3$$

$$= 0.33 \qquad\qquad = 0.22 \qquad (II.69c)$$

each of which is nearly twice its corresponding experimental value. Following the picture of three valence quarks, and a uniform core of $q\bar{q}$ pairs we see that

$$\int_0^1 F_2^{\gamma p}(x)\,dx = \sum_N \theta_N \left(2\left(\tfrac{2}{3}\right)^2 + \left(\tfrac{-1}{3}\right)^2 + \frac{\left(\tfrac{2}{3}\right)^2 + \left(\tfrac{-1}{3}\right)^2 + \left(\tfrac{-1}{3}\right)^2}{3}(N-3)\right)\Big/ N \simeq \left(\tfrac{3}{9} + \tfrac{1}{3}\tfrac{1}{N}\right) \gtrsim 0.22$$

$$\int_0^1 F_2^{\gamma n}(x)\,dx = \sum_N \theta_N \left(\left(\tfrac{2}{3}\right)^2 + 2\left(\tfrac{-1}{3}\right)^2 + \frac{\left(\tfrac{2}{3}\right)^2 + \left(\tfrac{-1}{3}\right)^2 + \left(\tfrac{-1}{3}\right)^2}{3}(N-3)\right)\Big/ N \simeq \tfrac{2}{9} \sim 0.22 \qquad (II.69d)$$

each of which is still larger than the corresponding experimental integrals. But the Kuti-Wieskopf model[57] which includes the neutral gluon (something to hold the targets' constituents together) in addition to valence quarks and the

sea of $q\bar{q}$ pairs predicts a value for (II.69a) which is comparable with both experimental results in (II.69b). However, unless we disbelieve in symmetric momentum distribution (i.e. eq. (II.60) would be wrong) otherwise the gluon or neutral parton exists and have no weak or electromagnetic charge but carry momentum as hypothesized.

When having had the neutrino scattering discussed, the amount of the momentum carried by gluons will be given.

## II.6 Weak Deep Inelastic lN Scattering

### (II.6a) Kinematics of $\nu(\bar{\nu})N$ scattering

By neglecting the nearly zero mass of the incoming neutrinos on account of being at high energies, the unpolarized inelastic neutrino nucleon double differential cross section reads as:

$$\frac{d^2\sigma}{d\Omega d\epsilon'} = \frac{G^2}{(2\pi)^2}\left(\frac{M_w^2}{M_w^2+Q^2}\right)\frac{\epsilon'}{\epsilon} L_{\mu\nu} W^{\mu\nu} \delta(\Sigma E_f - \Sigma E_i) \tag{II.70a}$$

where in contrast to electron scattering the propagator has infinite mass meaning there is no $Q^{-4}$ in the cross section and a much larger fraction of the data is at large $Q^2$. However the leptonic tensor could be written down as:

$$L_{\mu\nu} = k_\mu k'_\nu + k'_\mu k_\nu - k\cdot k'\, g_{\mu\nu} \pm i\varepsilon_{\mu\nu\lambda\sigma} k^\lambda k^\sigma \tag{II.71}$$

where the extra term which is seen multiplied by the fourth rank Levi-Civita symbol denoting to the separate existence of the left-handed neutrino (hence, upper sign) and right-handed antineutrino (lower sign) beams is cancelled out in electron scattering due to averaging over the two-co-existing right- and left-handed electron spin states in the initial beam. This is also the reason for not having a factor of $\frac{1}{2}$ in front of (II.70). Moreover, $W^{\mu\nu}$ may be written as:

$$W^{\mu\nu} \sim |\langle n| J^{(H),\nu}_{(0)}|P\rangle|^2 \sim \langle P| J^{\mp,\mu}_{(0)}|n\rangle\langle n| J^{\pm,\nu}_{(0)}|P\rangle \qquad (II.72a)$$

but, because the weak interaction current is not conserved, and as it is a mixture of vector and axial parts, the expansion of $w^{\mu\nu}$ now involves all the basic tensors $P^\nu, P^\mu q^\nu, q^\mu q^\nu, g^{\mu\nu}, \varepsilon^{\mu\nu\alpha\beta}P_\alpha P_\beta$ with which the same procedure as in electron case, leads us to:

$$W^{\mu\nu} = -g^{\mu\nu} W_1 + P^\mu P^\nu \frac{W_2}{M^2} - i \frac{\varepsilon^{\mu\nu\alpha\beta}P_\alpha P_\beta}{2M^2} W_3 + \cdots \qquad (II.72b)$$

$$= \sum_n \left| \underset{P}{\overset{x}{\rightleftharpoons}} n \right|^2 \sim 2 \, \mathfrak{Im} \; \underset{P \quad P}{\overset{x \quad q}{\bigotimes}}$$

if the lepton is serving as an external source of the virtual meson field $W_\mu$ coupled to a hadron current $J^{(H)}_\mu$.

In contrast to the electromagnetic structure functions which are purely vector-vector (VV), $W_{1,2}$ are now each the sum of two parts, (VV) and axial-axial (AA). But $W_3$ is the vector-axial vector interference term only, with one of the two currents in the right-hand term of the above graphical representation of $W^{\mu\nu}$ being vector and the other axial.

Contraction of (II.71) and (II.72b) yields (in the Lab.):

$$L_{\mu\nu} W^{\mu\nu} = 2EE' \left( 2 \sin^2 \frac{\theta}{2} \, W_1 + \cos^2 \frac{\theta}{2} \, W_2 \mp \frac{E+E'}{M} \sin^2 \frac{\theta}{2} \, W_3 \right) \qquad (II.73)$$

Note as the (V-A) interference term in $W^{\mu\nu}$ couples to the (V-A) interference term in $L_{\mu\nu}$, hence two different signs appear in front of $W_3$. This involves a $\gamma_5$ which effectively changes sign when we go from lepton (V-A) to antilepton (V+A) i.e. replacing a neutrino beam by an antineutrino beam. Introducing (II.73) into (II.70a) yields:

$$\frac{d^2\sigma}{d\Omega dE'}\binom{\nu}{\bar{\nu}} = \frac{G^2 E'^2}{2\pi^2} \left( \frac{M_W^2}{M_W^2 + Q^2} \right)^2 \left[ 2W_1 \sin^2 \frac{\theta}{2} + W_2 \cos^2 \frac{\theta}{2} \mp W_3 \frac{E+E'}{M} \sin^2 \frac{\theta}{2} \right] \qquad (II.70b)$$

which may also be represented as:

$$\frac{d^2\sigma}{dQ^2 d\nu}\binom{\nu}{\bar{\nu}} = \frac{G^2 E'}{2\pi E}\left(2W_1 \sin^2\frac{\theta}{2} + W_2 \cos^2\frac{\theta}{2} \mp W_3 \frac{E+E'}{M} \sin^2\frac{\theta}{2}\right) \qquad (II.70c)$$

The hypothetical absorption cross sections $\sigma_R$, $\sigma_L$, and $\sigma_S$ are respectively defined for the right-handed, left-handed, and scalar intermediate vector boson, W, in analogy with the electro-magnetic case. In terms of these, the structure functions $W_{1,2,3}$ read as:

$$W_1 = \frac{K}{\pi G\sqrt{2}}(\sigma_R + \sigma_L) \qquad (II.74a)$$

$$W_2 = \frac{K}{\pi G\sqrt{2}}\frac{Q^2}{Q^2 + \nu^2}(\sigma_R + \sigma_L + 2\sigma_S) \qquad (II.74b)$$

$$W_3 = \frac{K}{\pi G\sqrt{2}}\frac{2M}{\sqrt{\nu^2 + Q^2}}(\sigma_R - \sigma_L) \qquad (II.74c)$$

It is clear now that if $\sigma_R = \sigma_L$, i.e.: conservation of parity, then $W_3 \longrightarrow 0$ and $\frac{\sigma_R + \sigma_L}{2} = \sigma_J$ as it is the case in electromagnetic case.

(II.6b)  <u>Quark-Parton Picture of Inelastic ($\nu, \bar{\nu}$)P Scattering</u>

Eq. (II.72a) may also be rewritten as (with p and n denoting the relevant target nucleon, 1 and 2 being SU(2) indices):

$$W_{\mu\nu}^{\nu p} = \frac{E}{M}(2\pi)^2\int d^4x\, e^{iq\cdot x} <P|J_\mu^{1-i2}(x)\, J_\nu^{1+i2}(0)|P> \qquad (II.75a)$$

$$W_{\mu\nu}^{\bar{\nu}p} = \frac{E}{M}(2\pi)^2\int d^4x\, e^{iq\cdot x} <n|J_\mu^{1+i2}(x)\, J_\nu^{1-i2}(0)|P> \qquad (II.75b)$$

which satisfy the strangeness conserving ($\Delta S = 0, \Delta I = 1$) component of $J^{(h)}$, the hadronic current. From (II.75) and iso-spin invariance it is seen that:

$$W_{\mu\nu}^{\nu p} = W_{\mu\nu}^{\bar{\nu}n} \qquad\qquad W_{\mu\nu}^{\bar{\nu}p} = W_{\mu\nu}^{\nu n} \qquad (II.76)$$

In the (kindergarten) parton model point of view of the deep inelastic neutrino nucleon scattering the weak current acting

at the parton neutrino vertex changes the charge of the parton as such that $\Delta Q = 1$ (the basic reaction is supposed to read as: $\nu_i\ \underset{\text{parton}}{} \longrightarrow \ell\ \underset{\text{parton}}{}$ ). Therefore for spin $-\tfrac{1}{2}$ partons we have:

$$W_{\mu\nu}^{\nu p} \int_0^1 dx \sum_{N,i,i'} \mathscr{P}_N \frac{Em_i^2}{M E \bar{E}'} \int_0^1 d^3\bar{p}'\ \bar{u}_{i'}\gamma_\mu (1-\gamma_5) u_i \bar{u}_i \gamma_\nu (1-\gamma_5) u_{i'} f_i(x) e_i^{2,w} \delta^4(\bar{p}+q-\bar{p}') \quad \text{II.72c)}$$

(for antipartons $u \to v$ ) here $e_i^W$ is a weak charge which is unity if the parton belongs to an isospin multiplet and can be raised by an isospin raising operator to i', otherwise $e_i^W$ vanishes. On the other hand $e_i^{-W}$ in the following relation(s) is unity if the parton i can be lowered to i', but vanishes otherwise:

$$W_{\mu\nu}^{\bar{\nu} p} \to \int dx \sum_{N,i,i'} \mathscr{P}_N \frac{Em_i^2}{M E \bar{E}'} \int d^3\bar{p}'\ \bar{u}_{i'}\gamma_\mu (1-\gamma_5) u_i \bar{u}_i \gamma_\nu (1-\gamma_5) u_{i'} f_i(x) \bar{e}_i^{-i,w} \delta^4(\bar{p}+q-\bar{p}') \quad \text{(II.72d)}$$

Still these two equations may be brought to situations like that of eq. (II.72b) which enables us to compare the relevant coefficients and get:

$$\lim_{\substack{\mathscr{Z}_{tom}\\ B_j}} MW_1\binom{\nu}{\bar{\nu}} \longrightarrow \sum \mathscr{P}_N \sum f_i(x) \frac{e_i^{2,w}}{\bar{e}_i^{2,w}} = F_1(x)\binom{\nu}{\bar{\nu}} \tag{II.77a}$$

$$\lim_{\substack{\mathscr{Z}_{tom}\\ B_j}} \nu W_2\binom{\nu}{\bar{\nu}} \longrightarrow \sum \mathscr{P}_N \sum f_i(x) \frac{e_i^{2,w}}{\bar{e}_i^{2,w}} 2x = F_2(x)\binom{\nu}{\bar{\nu}} \tag{II.77b}$$

$$\lim_{\substack{\mathscr{Z}_{tom}\\ B_j}} \nu W_3\binom{\nu}{\bar{\nu}} \longrightarrow \sum \mathscr{P}_N \sum f_i(x) \frac{e_i^{2,w}}{\bar{e}_i^{2,w}} 2\eta_i = F_3(x)\binom{\nu}{\bar{\nu}} \tag{II.77c}$$

here $\eta_i$ is a signature which is negative for partons and positive for antipartons. There is the following interrelation between $F_i$:

$$F_1^{\nu,\bar{\nu}} = \frac{1}{2x} F_2^{\nu,\bar{\nu}} \tag{II.78a}$$

$$\mp 2 F_1^{\nu,\bar{\nu}} = \mp \frac{1}{x} F_2^{\nu,\bar{\nu}} = F_3^{\nu,\bar{\nu}} \tag{II.78b}$$

here the upper (lower) sign refers to parton (antiparton) contribution. With $F_{2,3 p}^{\nu,\bar{\nu}}$ and $F_{2,3\bar{p}}^{\nu,\bar{\nu}}$ being the contributions of parton ($p$) and antiparton ($\bar{p}$) to $F_{2,3}^{\nu,\bar{\nu}}$, the probabilities for

finding parton and antiparton at a given x read as

$$F_{2,3}^{\nu,\bar{\nu}} = F_{2,3f}^{\nu,\bar{\nu}} + F_{2,\bar{f}}^{\nu,\bar{\nu}} \tag{II.79}$$

which with respect to (II.100b) we get the following relations:

$$F_{3,f}^{\nu,\bar{\nu}} = \frac{-1}{x} F_{2,f}^{\nu,\bar{\nu}} \qquad\qquad F_{2,\bar{f}}^{\nu,\bar{\nu}} = \frac{1}{x} F_{3,\bar{f}}^{\nu,\bar{\nu}} \tag{II.78b'}$$

Now, if

$$M_W^2 \gg Q^2 \sim 4 \varepsilon \varepsilon' \sin^2\frac{\theta}{2} = 4\frac{\nu^2}{y^2}(1-y)\sin^2\frac{\theta}{2} \Rightarrow dQ^2 d\nu = \frac{2M\nu^2}{y}dx\,dy$$

then, bracket involving $M_W^2$ can be dropped out, and we may write (II.70) in terms of $F_i^{\nu,\bar{\nu}}$ and $0 < y = \frac{\nu}{\varepsilon} < 1$ (the inelasticity which is the ratio of the actual energy transferred to the maximum transferrable energy) as:

$$\lim_{\substack{\varepsilon,Q^2,\nu\to\infty \\ x,y\ fixed}} \frac{d^2\sigma}{dx\,dy}\left(= \frac{2M\nu^2}{y}\frac{d^2\sigma^{\nu,\bar{\nu}}}{dQ^2 d\nu} = \frac{2M\nu\varepsilon\varepsilon'}{\pi}\frac{d^2\sigma^{\nu,\bar{\nu}}}{d\Omega d\varepsilon'}\right) = \frac{G^2 M\varepsilon}{\pi}\left((1-y)F_2 + \left(\frac{y^2}{2}\right)2xF_1 \mp y(1-\frac{y}{2})xF_3\right) \tag{II.80}$$

With respect to (II.78) and (II.79) we get (II.80) as:

$$\lim_{\substack{\varepsilon,Q^2,\nu\to\infty \\ x,y\ fixed}} \frac{d^2\sigma^{\nu}}{dx\,dy} = \frac{G^2 M\varepsilon}{\pi}\left(F_{2,f}^{\nu}(x) + (1-y)^2 F_{2,\bar{f}}^{\nu}(x)\right) \tag{II.81a}$$

$$\lim_{\substack{\varepsilon,Q^2,\nu\to\infty \\ x,y\ fixed}} \frac{d^2\sigma^{\bar{\nu}}}{dx\,dy} = \frac{G^2 M\varepsilon}{\pi}\left((1-y)^2 F_{2,f}^{\bar{\nu}}(x) + F_{2,\bar{f}}^{\bar{\nu}}(x)\right) \tag{II.81b}$$

Integrating these with respect to y and then x leads to:

$$\lim_{\varepsilon\to\infty} \sigma^{\nu} = \frac{G^2 M\varepsilon}{\pi}\int_0^1\left(F_{2,f}^{\nu}(x) + \frac{1}{3}F_{2,\bar{f}}^{\nu}(x)\right)dx \tag{II.82a}$$

$$\lim_{\varepsilon\to\infty} \sigma^{\bar{\nu}} = \frac{G^2 M\varepsilon}{\pi}\int_0^1\left(\frac{1}{3}F_{2,f}^{\bar{\nu}}(x) + F_{2,\bar{f}}^{\bar{\nu}}(x)\right)dx \tag{II.82b}$$

which means under the scaling assumption (II.77), the cross sections should rise linearly with incident beam energy. However, the data in Fig. 28 are from experiments[59] done at CERN in energy range E = 2-15 GeV and from FNAL in the range E = 20-100 GeV. Both neutrino and anti-neutrino cross sections

are rising linearly with energy supporting above theoretical predictions.

### (II.6c) Experimental Evidence

The CERN experimental data of Fig. 28 indicates that:

$$\mathbb{R} = \frac{\sigma(\bar{\nu})}{\sigma(\nu)} = 0.38 \pm 0.04 \qquad (II.83a)$$

$$= \frac{3 + A - 2B}{3 + A + 2B} \qquad (II.83b)$$

$$= \frac{3 - L + 3R}{3 + 3L - R} \qquad (II.83c)$$

where $\quad A = \dfrac{\int_0^1 2x F_1 dx}{\int_0^1 F_2 dx} \quad , \quad B = \dfrac{\int_0^1 x F_3 dx}{\int_0^1 F_2 dx} \quad , \quad R, L = \sigma_{R,L} / (\sigma_R + \sigma_L + 2\sigma_S)$

$\mathbb{R}$ asks for the reliability of the assumptions (II.76) and (II.77) accepting the inequalities $0 \leq |B| \leq A \leq 1$ which is followed from the positive definiteness of the probability. However, the imposed limitation on the magnitude of A of this inequality, from $\mathbb{R}$, reads as:

$$0.87 \pm 0.10 = \frac{3(1 - \mathbb{R})}{1 + 3\mathbb{R}} \leq A \leq 1 \qquad (II.84)$$

showing how correctly the Callan-Gross relations (II.78a) are satisfied. A=1 follows if the longitudinal cross section, $\sigma_s$, can be neglected in comparison with the transverse ones (i.e. $\sigma_s \ll \sigma_L, \sigma_R$ ) in which event R+L = 1 causing $\mathbb{R}$ to be between $\frac{1}{3}$ (if R=0) and 3 (if R=1). (II.83a) confirms the lower limit of $\frac{1}{3}$, suggesting again that most of the constituents inside the proton are of spin $-\frac{1}{2}$ entities. Also $\mathbb{R} \sim \frac{1}{3}$ hints a factor 3 reduction for antineutrino cross section has the following explanation in quark-parton model wherein by V-A theory particles are left-handed and antiparticles are right-handed. For a system of two spin $\frac{1}{2}$ particles (or antiparticles), such as $\nu q$ (or $\bar{\nu}\bar{q}$ ), colliding colinearly in c.m. there is no angular

restriction whatsoever, since the total angular momentum J=0.

Hence, the y-distribution is isotropic i.e.: $d\sigma/dy \; (\nu q \; ; \; \bar\nu\bar q) \sim$

constant as it is the case of the data[60] for E $\sim$ 50 GeV in Fig.

29 - the straight line, being referred to as A - from FNAL which

is consistent with the data for E $\sim$ 30 GeV from CERN for various

region of x. On the other hand for a c.m. colinear interacting

system of spin -$\frac{1}{2}$ particle-antiparticle, such as $\nu\bar q$ (with $J_z = -1$ )

and $\bar\nu q$ (with $J_z = +1$ ), isotropic interaction is impossible since,

for instance to have our antiparticle, $\bar\nu$ , scattered backward

by the particle q, there is a needness for $J_z$ to be equal to -1

resulting in $\Delta J_z = -2$ . Through emerging initials and finals:
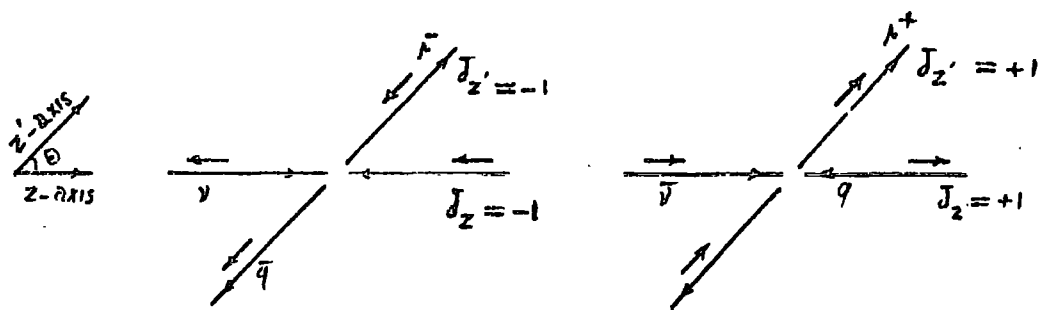


Diag. II.6:  Emerging initials and finals of a system
of two interacting (a) particle $\nu$-antiparticle $\bar q$ and
(b) antiparticle $\bar\nu$-particle q of spin $\frac{1}{2}$

the angular momentum conservation may be worked[61] out

resulting in an angular distribution of the following form:

$$\left| d^1_{11}(\Theta) \right|^2 = \frac{(1+\cos\Theta)^2}{4} = (1-y)^2 \sim \frac{d\sigma}{dy} \; (\nu\bar q \; ; \; \bar\nu q)$$

(II.85)

which vanishes for $\Theta = \pi$ (equal to impossibility of $\Delta J_z = 0$ , see

above) and yield the factor 3 reduction upon it being itegrated.

However, the $(1-y)^2$ distribution for $\bar\nu$ induced reactions can be

seen in Fig. 29 (the curvey line, being referred to as B).

For an isoscalor target above argument leads us to

differential cross sections (II.81) being based on the con-

ventions (II.78) and (II.79) to which adding the definition;

$$Q = \int_0^1 \mathcal{F}^{\nu,\bar\nu}_{i,\bar i}(x) \, dx$$

(II.86)

reveals the role of B, whose magnitude has the following limitations:

$$0.87 \pm 0.10 \leqslant B = \frac{Q - \bar{Q}}{Q + \bar{Q}} \leqslant \frac{2(1 - \mathbb{R})}{1 + \mathbb{R}} = 0.90 \pm 0.08 \qquad (II.87)$$

Accepting only the spin $\frac{1}{2}$ entities results in to have the upper limit of (II.87) for B. Therefore, as B measures the amount of antimatter in the nucleon, we may have the spin $\frac{1}{2}$ antiparticle cross section contributions as:

$$\frac{\bar{Q}}{Q + \bar{Q}} = \frac{1 - B}{2} = \frac{3\mathbb{R} - 1}{2(\mathbb{R} + 1)} = (0.05 \pm 0.04) \qquad (II.89)$$

which is a few percent showing the relative importance of quarks over antiquarks.

(II.6d)   The Gluon Momentum:

With respect to (II.64), for nucleon we have:

$$F_2^{eN}(x) = \left( \frac{5}{9} (u + d + \bar{u} + \bar{d}) + \frac{2}{3} (s + \bar{s}) \right) \frac{x}{2} \qquad (II.90)$$

and with respect to (II.77b), $F_2^{\nu N}$ which is a measure of the number of scatterers inside the nucleon may be written as:

$$F_2^{\nu N}(x) = x \left( u + d + \bar{u} + \bar{d} \right) \qquad (II.91)$$

Comparing the integrated form of (II.90) and (II.91) we get the following prediction for "the mean square quark charge":

$$<Q^2> = \frac{\int_0^1 F_2^{eN}(x) dx}{\int_0^1 F_2^{\nu N}(x) dx} \geqslant \frac{5}{18} = 0.278 \qquad (II.92)$$

The experimental values of the quantities in eq. (II.92) are[59]:

$$\int_0^1 F_2^{eN}(x) dx = 0.15 \pm 0.01 \qquad \int_0^1 F_2^{\nu N}(x) dx = 0.51 \pm 0.05 \qquad (II.93)$$

with which $<Q^2> = 0.29 \pm 0.03$.

However, we know that u, d, s are the probability of

finding, respectively, up, down, strange quarks and hence xu, xd, xs should represent the fractional momentum distributions of the target's momentum among the quarks. Therefore we expect that the integration of (II.91) expresses the total fractional momentum (or mass) carried by the constituents of the proton, and hence to be unity. This is much more than what has been found experimentally in (II.92). Also from (II.90) we expect to have $\frac{18}{5} \int_{0}^{1} F_2^{eN}{}_{(x)} dx$ equal to unity, which its numerical value is something roundabout $0.52 \pm 0.03$. This nearly half the momentum is believed to be carried by the gluons.

## II.7    Lepton Pair Production

It has been shown[63] that:  if at high energies, s, when kinematical constraints allowing application of the impulse approximation have been met by a process in which two hadrons A and B (e.g.: pp, $e^- e^+$, $\mu\nu$, and $\gamma P$) interact absorbing or producing a lepton pair (e.g.: $\mu^+\mu^-$, $e^- e^+$, $\mu\nu$, and $e\nu$) of huge mass, $Q^2$, such that $Q^2/s := \tau$ is finite, then the governing subprocess in which the quarks have been assigned conditionally a limited finite momentum transfer, is named as the quark fusion model; since a quark (from A or B) fuses against an antiquark (from B or A). However, by neglecting the hadron mass in account of being at high energies, and if $P_1$ and $P_2$ are four momenta of A and B which are supposed to be protons, then;

$$s = (P_1 + P_2)^2 \sim 2P_1 P_2 \qquad\qquad (II.94)$$

Also if $x_{1,2}$ are the fraction of the longitudinal momenta of parent protons carried by the partons, then from conservation of the four-momenta at each vertex we see that:

$$Q^2 = (x_1 P_1 + x_2 P_2) \sim x_1 x_2 s \quad ; \quad 0 < x_{1,2} < 1 \qquad (II.95)$$

This is the formal condition for a pair of mass $Q^2 = m_{\mu\mu}^2 = (P_{\mu_1} + P_{\mu_2})^2$ being formed in the reaction: $P+P \longrightarrow q\bar{q} \longrightarrow \mu_\nu + hadrons$
$\;\;\;\;\;\;\; \longrightarrow \mu^+\mu^-$ for which the differential cross section is:

$$\frac{d\sigma(s,Q^2)}{dQ^2} = \frac{1}{3}\sum_i \frac{4\pi\alpha^2}{3Q^2}e_i^2 \int_0^1\int_0^1 f_i(x_1)f_{\bar{i}}(x_2)\frac{x_1x_2}{Q^2}\delta(x_1x_2-\frac{Q^2}{s})dx_1dx_2 \qquad (II.96)$$

Here, $f_i(x_1)\left(f_{\bar{i}}(x_2)\right)$ are the probability of finding $q_i(\bar{q}_i)$ with fraction $x_1(x_2)$ of momentum $P_1(P_2)$, and $x_1x_2/Q^2$ stands for the proton flux. The factor $\frac{1}{3}$ comes from coloured quark model wherein each quark is found in three versions: red, green, and blue.

However, in the present process which proceeds via a massive timelike virtual photon, both partons are having spacelike momenta.

By writing (II.96) as:

$$\frac{d\sigma}{dQ^2} \sim \sum_i e_i^2 \int q_i(x_1)\bar{q}_i(x_2)\delta(x_1x_2-\frac{Q^2}{s})dx_1dx_2 \qquad (II.97a)$$

where $q_i(x_1) = x_1 f_i(x_1)$ $\left(and\; \bar{q}_i(x_2)=x_2 f_{\bar{i}}(x_2)\right)$ stand for the quark (anti-quark) distribution function, with respect to (II.66) and neglecting any contribution from the strange quark (II.92a) results in:

$$\frac{d\sigma}{dQ^2} \sim \left[\left(4V_u(x_1)+V_d(x_1)+10s(x_1)\right)\frac{s(x_2)}{9} + \left(4V_u(x_2)+V_d(x_2)+10s(x_2)\right)\frac{s(x_1)}{9}\right] \qquad (II.97b)$$

Now, with having the rough estimate of the shape of $V(x)$ and $s(x)$ (for instance, from electron scattering data of Fig. 27) the data on present reaction are given[34] (the presented) theoretical fit (in Fig. 30). However, the sharp fall off of the calculated curve in Fig. 30 is traced back to the antiquark distribution function, $s(x)$ (see (II.66)) being zero for $x \leqslant 0.4$. Moreover the discrepancy between the data (at $\sqrt{Q^2} \leqslant 2.5$ GeV) and the curve is assigned to $\sqrt{Q^2}$ values being low for the assymptotic theory to be valid. Of other several facts for such dis-

crepancies is the basic assumption of zero transverse momenta

assigned to the quarks in order to see them free of their

binding energy. This has been corrected by attributing a "finite"

transverse momentum to each quark. Also in quantum chromodyna-

mics[64] (QCD) based on some experimental facts, such as depen-

dence of the average transverse momentum of lepton pairs

produced in pp collisions on the mass of the pair, there have

been given several corrections to the aforementioned leading

Drell-Yan diagram confirming the quark transverse momentum as

well as having quarks and gluons responsible for forming the

basic (previously discussed) subprocesses.

# CHAPTER III

## Large P$_t$ Phenomena

### III.1 Introduction

In the last two chapters we presented some experimental and theoretical discussion concerning the existence and properties of hadronic constituents. These constituents are of course approximately pointlike spin $\frac{1}{2}$ quarks. Such a quark structure of hadrons will be used in this chapter. This will be done by means of looking into the single- and many-particle data at large P$_t$ from the point of view of the predictions coming from specific theoretical models. In Sec. III 2 we introduce some theoretical idea which will be used in the rest of the chapter. Experimental observations defining the structure of the large P$_t$ events are dealt with in Sec. III.3, and the theoretical predictions are compared with experiments in Sec. III.4. Sec. III.5 deals with recent experiments where the process is triggered not by a single particle at large P$_t$ but by a large P$_t$ "jet". The last section is devoted to a summary of the conclusions.

### III.2 Some Theoretical Remarks

### (III.2a) Preliminary Remarks

Of lots of various phenomenological functions giving experimental parametrization to the invariant cross-section distribution one is the following (see Ch. I):

$$\frac{E d^3\sigma}{dp^3} = A \, P_\perp^{-N} \, f(x_\perp, \theta) \qquad \text{(III.1a)}$$

or in order to take into account also the low P$_t$ region it can

be equivalently seen as:

$$\frac{E d^3 \sigma}{d p^3} = A \left( P_\perp^2 + M^2 \right)^{-N/2} f(x_\perp, \Theta)$$
(III.1b)

However, the scaling function, $f(x_\perp, \Theta)$ , which is expected in parton models to be energy independent at fixed reduced transverse momentum, $x_\perp \sim 2 P_\perp / \sqrt{s}$ , is often approximated at $\Theta = 90^\circ$ as:

$$f(x_\perp, \Theta \sim 90^\circ) = (1 - x_\perp)^F$$
(III.2a)

or, equivalently, as:

$$f(x_\perp, \Theta) \underset{x_\perp \to 1}{\sim} f(\Theta) (1 - x_\perp)^F$$
(III.2b)

The parameters N, $M^2$, and F, as obtained[65] in various experiments, are given in Table I. This table, in summary, shows the value of N to be equal to $\sim$ 8 for pions, 8-9 for kaons, 10-12 for protons, and 9 for antiprotons. (Apart from recent experimental measurements[84] of inclusive neutral pions (up to $P_t = 16.5$ GeV/C) production at c.m. energies of 53 and 63 GeV, $\Theta \sim 90^\circ$, from PP collision) these values are generally compatible with those suggested by the dimensional counting rules,[66] a subject which has also shown a good success in predicting the value of $n \equiv N/2$ of the asymptotic form[67] of the differential cross section of the exclusive hadronic reactions, at wide angle, as:

$$\frac{d\sigma}{dt} (AB \to h, D) \sim s^{-n} f(\Theta)$$
(III.3)

This, however, could be[68] correct at not too large energy ($S < 100$ GeV$^2$, $|t| > 2.5$ GeV$^2$).

(III.2b) Parton Models and Counting Laws

Given experimental facts in Chapter I and conclusion there-in encourage the idea that hadrons are made of constituents, or partons if we consult as well the success of leptons in providing an ideal tool for investigating the hadron structure (see Chapter II). It is, however, believed that the destruction of the coherence of the initial hadron states and their subsequent evolution into many new hadron states have the following underlying mechanism:
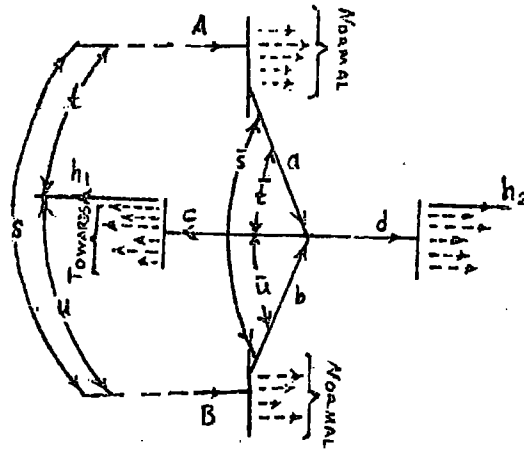


Diag.III.1: The structure of the large Pt inclusive process AB ⟶ h₁x in a hard collision model where there is an underlying 2-2 subprocess

Here a and b are some sort of constituent of A and B, respectively, which undergo a wide angle collision - depending on the forthcoming models - either elastically or quasi-elastically to produce c and d. Either these products themselves or their fragments appear as two final hadronic jets in one of which we trigger on $h^{\pm}_{0} = h_{1}$ at large $P_{t}$. Then the scaling behaviour of the inclusive cross section, $AB \to h_{1}X$, at large $P_{t}$ reflects the scaling behaviour of the subprocess $ab \to cd$ which is given by the dimensional counting rules defining:

$$N = N/2 = n_{active} - 2 \qquad (III.4)$$

$$F = 2n_{passive} - 1 \qquad (III.5)$$

In these equations, $n_{active} = n_a + n_b + n_c + n_d$ is the total number of elementary fields (q, l, $\gamma$) in the high $P_t$ hard subprocess ab $\longrightarrow$ cd and $n_{passive} = n(\bar{a}A) + n(\bar{b}B) + n(\bar{h}_1 c)$ is the number of elementary constituents that "waste" the momentum in the fragmentations A $\longrightarrow$ a, B $\longrightarrow$ b, and c $\longrightarrow$ $h_1$.

## (III.2c) Specific Models

If it is supposed[69] that the wide-angle quark-quark elastic scattering should satisfy the demands of the dimensional counting rules (III.3), this gives N = 4 in (III.1) in contrast to the experimental result. Also it can be proved[70] that the understanding of the exclusive processes, in the context of the dimensional counting rules, needs suppression of the quark-quark scattering. On the other hand, for the counting rules there is no firm experimental evidence, for instance the consequences of these rules are only applicable[65] in the limit of $x_t \to 1$ while bulk of the data are in the region $x_t \leqslant 0.5$. Following this orientation, we see that Feynman and Field (FF)[70] have proposed that the behaviour of the qq $\longrightarrow$ qq scattering should simply be chosen in such a way as to fit the single particle inclusive data. In other words, it is the experiment which provides the reasonable form of the differential wide-angle quark-quark elastic scattering of the subprocess and not the counting rules. In this approach the correct $P_t$ and $\theta_{cm}$ dependence in (III.1) has led them to chose the form:

$$\frac{d\sigma}{d\bar{t}} \propto 1/(-\bar{s}\,\bar{t}^3) \qquad (III.7)$$

where the invariants $\bar{s}$, $\bar{t}$ (and $\bar{u}$) refer to the qq $\longrightarrow$ qq amplitude. In this model, the proportionality factor, A, which is used to fit the inclusive cross section data up to $P_t = 5$ GeV/C

has the following numerical value:

$$A = 2.3 \times 10^3 \text{ mb GeV}^6$$

However, of the data which favour (III.7) are those of the angular dependence of the invariant cross section for reaction PP $\longrightarrow \pi^+ X$ at 53 GeV in Fig. 31 (as a solid curve). This figure confirms that the more peripheral the parton scattering, the more peaked is the behaviour at $\theta = 0^\circ$. However, in this class of model, the rarity of the high energy wide angle parton scattering is claimed for the rarity of the cross section.

Despite the aforementioned failure of the counting rules it may be claimed that they still work and accept that at present energies quark-quark scattering must be suppressed for some unknown reason. Then accepting the other choices for a, b, c and d seems permissible. Biased towards this approach, of wide variety of proposals are the Constituent Interchange Model[71] which in its language the quark-particle scattering is supposed to dominate, and the Quark Fusion model[72] in which two constituents fuse to produce the detected final state particle. In these classes of models one of the engaged partons is supposed to be at large $P_t$ and the rarity of such partons inside the parent hadron accounts for the rarity of the cross section.

The calculated specific form for the hard scattering cross section in CIM still looks like (III.7). We note that the QF model is a possible CIM term which is special in many ways. In CIM a pair of quark-antiquark is exchanged in the $\bar{t}$ channel while in QF cases, the exchanged object in the $\bar{t}$ channel is a single quark.

CIII and QF models give good fit to the value of N and the form of the function $\tilde{F}(x_L, \theta)$ in (III.1). Experimental evidence for this statement comes from fit to the 90° data[73] at 200, 300 and 400 GeV, at Fermilab, and 90° ISR data[30] at 31, 45 and 53 GeV which are shown in Fig. 32.

### (III.2d) A Probabilistic Formula

Constituents of hadrons are believed to act freely if their parents each is having large enough momentum. However, the communication between these freely acting constituents (in the duration of short time and distance scales) form the basis of the hard scattering in each of the aforementioned specific theoretical models (see Diag. III.1). Based on the validity of such an idea we can give a probabilistic formula to describe the inclusive processes, $AB \rightarrow h_i x$, at high transverse momentum. To drive this formula, we may write a convolution integral over the structure functions $G_{a/A}(x_a, k_{ta})$, $G_{b/B}(x_b, k_{tb})$, and $D_c^{h_i}(z_c, k_{tc})$ times the square of the matrix element for the subprocess $ab \rightarrow cd$. Functions $G_{\alpha/\beta}$ describe the distributions of constituent $\alpha$ inside the initial hadron $\beta$, and functions $D_\alpha^\beta$ describe the distribution of hadrons $\beta$ within the jet (see later sections for the definition of jet) coming from the constituent $\alpha$. Notice that this incoherence between the structure of the initial state prior to the hard scattering process and the subsequent evolution of the scattered constituents is central to the basic impulse approximation approach to the inclusive processes at high transverse momentum.

However, with respect to above remarks and if the masses of a,b,c and d are neglected (i.e.: $|A(ab \rightarrow cd)|^2 \sim \frac{d\sigma}{dt}(ab \rightarrow cd)|_{S,T,U}$) then the invariant cross section corresponding to Diag. III.1

may be given as:

$$E \, d\mathcal{G}/d^3 p \, (s,t,u \, ; \, AB \to h_1 X) \sim \sum_{ab;cd} \int dx_a \, dx_b \, G_{a/A} \, G_{b/B} \, D_c^{h_1} \frac{d\mathcal{G}}{d\bar{t}} (\bar{s}, \bar{t}, \bar{u} \, ; ab \to cd) \quad (III.8)$$

where it is supposed [82] that the transverse momentum distribution is independent of the longitudinal momentum distribution which means, for instance;

$$D_c^{h_1}(z_c) = \int d^2 k_\perp \, D_c^{h_1}(z_c, k_{\perp c}) \quad (III.9)$$

In above formulas the notations read as follows (all defined in hadron beam target c.m.): $x_{a,b}$ are longitudinal momentum fractions and $k_{ta,b}$ transverse momenta of constituents a and b in parent hadrons A and B respectively. The outgoing constituent c fragments into a hadron $h_1$ which carries momentum fraction $z_c$ and transverse momentum $k_{tc}$ with respect to c. The invariants s, t, u referring to the hadron process AB $\to$ $h_1 x$ are defined in Appendix B and $\bar{s}$, $\bar{t}$, $\bar{u}$ may be given as follows (when $m^2_{a,b,c,d} = 0$):

$$\bar{s} \sim x_a \, x_b \, s - k_{\perp a} \cdot k_{\perp b} \quad (III.10a)$$

$$\bar{t} \sim (x_a/x_c) t + k_{\perp a} \cdot k_{\perp h_1} \quad (III.10b)$$

$$\bar{u} \sim (x_b/x_c) u + k_{\perp b} \cdot k_{\perp h_1} \quad (III.10c)$$

For the forms of the structure functions $G_{\alpha/\beta}$ and $D_\alpha^\beta$ in diffused quark scattering of Feynman, Field, and Fox (FFF)[70] we should relay on a careful analysis of the lepton processes. Indeed, as can be judged from Fig. 33, their choices about the quark decay functions $D_q^{\pi, K}$ are fitting a variety of different lepton data. On the other hand the proposal[83] of the Constituent Interchange Model (CIM) for the G-functions is as follows - if the dimensional coupling constant is given by g and $f_{\alpha/\beta}$ stands for the fraction of $\beta$'s momentum which is carried by $\alpha$ :

$$G_{\alpha/\beta}(x_\alpha) = (1+g_\alpha)\,\frac{(1-x_\alpha)^{\partial_\alpha}}{x_\alpha}\left(\rho_{\alpha/\beta} \equiv \int_0^1 x\,G_{\alpha/\beta}(x)\,dx\right)$$
$$\underset{x_\alpha \to 1}{\sim}(1-x_\alpha)^{2n(\bar\alpha\beta)-1}$$

(III.11)

Here $n(\bar\alpha\beta)$ is the minimum number of spectator elementary fields left behind when $\alpha$ is extracted from $\beta$. Also in these type of models the D-functions have the following proposal:

$$D_\alpha^\beta(z_\alpha) \sim \delta(1-z_\alpha)\,\delta_{\beta,\alpha}$$

(III.12)

As it is seen from (III.8) the inclusive cross section for AB $\longrightarrow$ h,x at high transverse momentum equals to the sum of the cross sections for contributing wide angles subprocesses, such as ab $\longrightarrow$ cd, weighted by the fractional momentum fragmentation probability functions $G_{\alpha/\beta}$ and $D_\alpha^\beta$. Therefore scaling of the inclusive spectra reflects the scale invariance of the subprocess ab $\longrightarrow$ cd. However, as it was discussed in previous section, particular models differ in the choice of the basic interaction $\left(d\sigma/dt\,(\bar s,\bar t;\,ab\to cd)\right)$. But definitely, as it was discussed previously, a $P_\perp^{-4}$ dependence of the inclusive spectra-coming from when the subprocess reads as $q_a + q_b \longrightarrow q_a' + q_b'$ with the q standing for the quarks, and, hence, the calculations based on inserting (III.7) into (III.8)—is not true from point of view of the experimental results asking rather for a $P_t^{-8}$ dependence. This means the involvement of six elementary fields in favour of models as like as the CIM and the quark fusion model (QF). However an important way of distinguishing between these models is to relay on comparison of the cross sections for different interactions with what is predicted from these models, a subject which we turn to after consulting experiments for knowing how the large $P_t$ events are constructed.

III.3 <u>Experimental Observation Remarks</u>

(III.3a)  <u>Structure of Large-$P_t$ Events</u>

In the context of the hard scattering model the
result of the collision has the following picture in
the momentum space. In this space, the final hadrons
appear in a coplanar jet configuration (collection of
several hadrons coming from constituents which are in-
itially isolated in momentum space) with jets of hadrons
aligned with the directions of both the scattered and
unscattered constituents. Moreover, these jets are four
in number. The first two are defined with respect to a
charged or neutral particle, $h^{\pm}_{\delta}$ , at large $P_{\perp}^{h^{\pm}_{\delta}} > P_{\perp}^{min}$
( $\sim$ usually 2.0 GeV/C) which is triggered upon in space
of ( $y$ , $P_{\perp}^2$ , $\phi$ ) . This trigger particle, $h^{\pm}_{\delta}$ , is
correlated to the other products, $h^{\pm}_{\lambda}$ , which are at $P_{\perp}^{h^{\pm}_{\lambda}}$
such that if $P_{\perp}^{h^{\pm}_{\delta}} \cdot P_{\perp}^{h^{\pm}_{\lambda}} > o$ , then $h^{\pm}_{\lambda}$ are forming the jet
towards the trigger. Otherwise, namely; if $P_{\perp}^{h^{\pm}_{\delta}} \cdot P_{\perp}^{h^{\pm}_{\lambda}} < o$ , $h^{\pm}_{\lambda}$
form the jet away from the trigger. However, these two
large $P_t$ jets do not have to be colinear in the c.m.,
since the c.m. of the scattering constituents is moving.
The other two jets are at small $P_t$ and result from the
break up of the beam and the target hadrons. These
small $P_t$ jets are called the soft hadronic background
(or the low $P_t$ cloud) and retain the main properties of the

"normal" events where no particle at large $P_t$ is produced.

As far as the experimental difficulties are concerned, events at large $P_t$ are compared to normal events; (that is, for instance, normal inelastic pp collisions). These are obtained by a minimum bias trigger (see later section) which should trigger on any inelastic pp collision.

However, in what follows, we present some experimental results supporting the above ideas.

(III.3b) <u>Viewing the Normal Component Experimentally</u>

Due to the experimental difficulties little if known about the behaviour of the secondaries at low $P_t$ in the events at large $P_t$. However, of subjects discussed in this part is the effect of the leading particle being defined as those secondaries which are carrying the same charge as the beam particle and most of the beam momentum. As it is seen from Fig. 32 increasing[74] transverse momentum of the trigger causes the reduction of the fraction of events with a leading particle in the large $P_t$ events. Also shown is the equality of the possibility of observing a leading particle for different triggers.

(III.3c) <u>Viewing the Towards Jet Experimentally</u>

Fig. 34 shows[75] the rapidity spectrum of particles produced within a $25^{\circ}$ azimuthal range of a trigger particle at high $P_t$. As it is seen, at narrow azimuthal wedge around the trigger particle, the secondary particles have formed a sharp narrow ($\Delta y \sim 1$) peak at $y = y^{h^{\pm}}$ which rises when the secondaries are selected to be at high $P_t$ and when $\Theta^{h^{\pm}}$ is increased. These peaks are present for all sorts of charge combinations. They are however three times bigger for opposite charge combinations of trigger and secondaries than the same charge combinations of them. Also it is seen that far from $y^{h^{\pm}}$, the distribution coincide with that of normal events. This excess is usually referred to as the towards jet in which particles have a limited[76] transverse momentum (of about 300 MeV/C) with respect to the vector sum of their momenta (i.e. the jet direction). This statement has its confirmation from the presented[76] background subtracted data in Fig. 35, where the data are describable by a function as like as $e^{-6(P_\perp^j)^2}$

representing the aforementioned value.

Coincidence of the two-pion invariant cross section for alongside production at $90^{\circ}$ which may be written as:

$$E_1 E_2 \, d^6 \sigma / d^3 P_1 \, d^3 P_2 \propto (P_{\perp 1} + P_{\perp 2})^{-N} \, f(x_{\perp 1} + x_{\perp 2}) \tag{III.13}$$

with those of the single particle inclusive spectra (being shown as solid curve in Fig. 36) exhibits the fact that all members of the jet come from the same parent. This parent cannot just be the resonance decay. For instance, estimated[77] from the data on the invariant mass distribution $M(\pi^{\pm} \pi^{\pm})$ and $M(\pi^+ \pi^-)$, (represented in Fig. 37) just 16% of $\pi$'s with $P_t > 2.0$ GeV/C can come from $\rho$-decay.

## (III.3d) Viewing the Away Jet Experimentally

Independent of the trigger rapidity and centred at $y \sim 0$ are the data[75] shown in Fig. 38 representing the rapidity distribution of particles opposite in azimuth to the trigger directions which is named as away side jet. This rejects the idea[78] of a back-to-back correlation in rapidity giving hope to the idea of having a configuration in which the away and towards jets tend to balance their transverse and longitudinal momenta. Comparing the presented data in Figs. 34 and 38 gives this idea that the away jet is covering a wider angular range. Indeed, as it is seen from the azimuthal distributions data[79] of Fig. 39, there is a broad bump ($\pm 90^{\circ}$) over the background of the normal events which is rising with $P_{\perp}^{h^{\pm}}$. This may mean that the multiplicity of the away jet grows[80] with $P_{\perp}^{h^{\pm}}$ when it is integrated over all $P_t$ of away produced particles. This can be seen from Fig. 40 where the data are fitted to a linearly rising function;

$$M_h(\phi, P_\perp, \sqrt{s}) = A_h(\phi) + B_h(\phi) P_\perp^{h\frac{\pm}{o}} + C_h(\phi) \, \log(s/s_o) \; ; \quad \sqrt{s_o} = 44.7 \; Gev \qquad \text{(III.14)}$$

with h denoting the trigger species to the nature of which the behaviour of the shown data do not depend.

It may be noted that if in c.m., $\emptyset$ is defined as: $\tan \phi = \dfrac{P_y}{P_x}$ such that $(P_\perp^{h\frac{\pm}{o}})^2 = P_x^2 + P_y^2$ with $P_x$ and $P_y$ defined as:



b- $\bar{x}$-$\bar{y}$ Projection

a-$\bar{x}$=$\bar{z}$ Projection
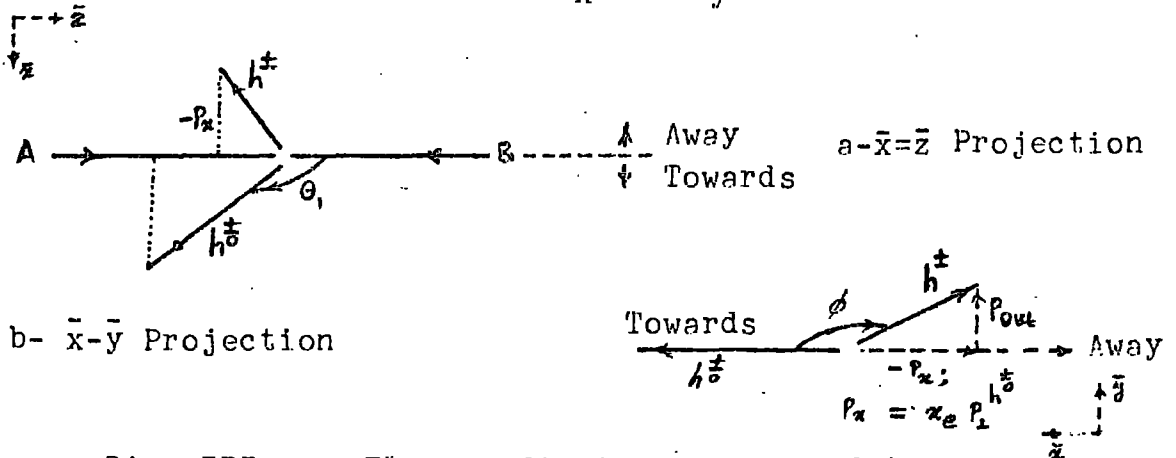
Diag.III.2: The coordinate system used to describe the production at high P$\perp$ in AB collision. $\bar{x}$-z plane is that of the beam A, and trigger hadron $h\frac{\pm}{o}$

then, the shrinking of $\emptyset$ distributions with $P_\perp^{h\frac{\pm}{o}}$ in Fig. 39 may mean that the component $P_{out} \sim P_y$, out of the triggering plane, is limited. More clearly, the shown $P_{out}$ distributions[79] (for different $P_x$ intervals in the case) of the $90°$ $\pi^o$ trigger; as it is seen in Fig. 41, are independent of $P_x$ and show an exponential cut-off in $P_{out}$, $e^{-2|P_{out}|}$, in favour of the expected coplanar structure in parton models.

Among the away particles, and through the correlation consideration therein, it is possible to find out that the away particles exhibit[81] a strong short range correlation in rapidity. This confirms the case to be the same as when the away particles have come from a narrow jet ($\Delta y \sim 1$). However as it is seen from Fig. 42 a stronger (by about a factor of 2) correlation exists for opposite charge pairs than for

the particles of the same charge. This has been assigned
to a substantial resonance production. Therefore we have
evidence confirming previous ones that there exists a narrow
jetlike structure in the away side region which its axis
changes direction from one event to another (this stays
sometimes for the name of an away fan-like jet).


## III.4  Theoretical Predictions

### (III.4a)  Remarks Related to the Single Particle Cross Section

In this part we are concerned with the beam ratios.
However, we know that in aforementioned specific theoretical
models, most of the $P_t$ dependence of the cross section arises
from the scattering rule chosen, while the angular behaviour
originates in the break up of the incident hadrons which in
turn depends on the distribution of momentum among con-
stituents making up the particles. Therefore, for two
different beams, A and B, the production ratio of a given
type of large $P_t$ particle, e.g.:

$$R(A/B) = \frac{E d\sigma (AP \longrightarrow \pi^0 X)/dp^3}{E d\sigma (BP \longrightarrow \pi^0 X)/dp^3} \qquad (III.15)$$

samples the ratio of A and B structure functions. For
instance, if A and B are, respectively, proton and pion, then
we need to have $G_{q/P,\pi}$ when we are fitting the data on $R(P/\pi)$
from the viewpoint of the diffused quark model. In this model
$G_{q/P}$ is given from the lepton induced processes (see Fig. 43a),
while $G_{q/\pi}$ has been assigned a constant value ( $\sim$ 0.25, dashed
line in Fig. 43b) from the theoretical predictions; because
there is no experimental information on $\nu W_2^{/\pi}$. With these
choices for $G_{q/P,\pi}$ we get a poor fit to the data on $R(P/\pi)$
(dashed curve in Fig. 44). However, to fit the data properly,
we may suppose that the (valence) quark and antiquark

distributions in pion go not to zero (like (1-x), as is
stated in counting laws) as $x \rightarrow 1$ but to a constant (as in
Fig. 43b, the solid lines) resulting[70] in a better fit to the
beam ratio $R(P/\pi)$ which is seen as a solid curve in Fig. 44.
On the other hand, based on a refined version of the G-functions
in the CIM and QFM, Chase and Stirling have [85] fitted the
data on the same ratio. This is seen in Fig. 45 where the QF
curve is already an order of magnitude too small at $x_t = 0.3$.
This disagreement is because of the involved type of antiquark
needed for the fusion which changes from valence to nonvalence
when the beam is changed from a proton to a pion. This is
against a predicted VV/VV (V for valence) shape of $R(P/\pi)$ from
the other two models (= diffused quark model and the CIM). This
idea is supported[86] also by comparing the inclusive, high $P_t$,
$\pi^0$ production spectra from $\pi^-$, $\bar{K}$, P and $\bar{P}$ beams at 100 and 200
GeV/C for $\theta_{cm}$ ranging from $2^0$ to $115^0$, and $P_t < 4.5$ GeV/C (see
Fig. 46). As shown in the bottom row of Fig. 46, the ratio
$R(\bar{P}/P)$ is close to 1. This value is what is expected when the
subprocesses emitting a single high $P_t$ quark produce as many
$\pi^0$ as those emitting an antiquark. In the other words, this
value of $R(\bar{P}/P)$ cannot be anticipated by the quark fusion
model since here we expect to see the enhancement of the
cross section in $P\bar{P}$ interactions (three valence $\bar{q}$ in the
initial state) relative to PP interactions.

The behaviour of the ratios in Fig. 46 also suggests
that the quarks scatter without regard to flavour (i.e.:
u,d, or s). Otherwise there would be just a reduction in the
magnitude of the $\pi^0$ cross section relative to the pion proton
interactions and the shape would be the same. However, the
variation in the ratios originate in the larger probability
for the quarks in the pion and kaon to have a greater portion
of the incident momentum.

(III.4b) <u>Jet Cross Section: Trigger Bias: Smearing</u>

Strong peaking of particle density in the trigger direction (in the Fig. 34) means that the number of correlated particles is small - that is: most of the jet momentum should be carried by the triggering particle. Based on proving this point is the experiment done by BFS group[87] who have estimated the momentum flow following the trigger $h^{\pm}_{o} = h^{\pm}$, which is emitted at 90°, as a function of $P_{\perp}^{h^{\pm}_{o}}$ and the trigger type. Consistent with the data, a linear dependence on $P_{\perp}^{h^{\pm}_{o}}$ is seen in Fig. 47 where the mean value $< \Sigma P_x >$ of the total momentum carried by all charged particles following the trigger within the rapidity interval $|y| < 1$ is plotted as a function of $P_{\perp}^{h^{\pm}_{o}}$. For the most relevant points, i.e. for $P_{\perp}^{h^{\pm}_{o}} \geqslant 2$ GeV/C, however, only the slopes for $\pi^{+}$ and $\pi^{-}$ triggers are well constrained by the data, such that: $d< \Sigma P_x > / d P_{\perp}^{h^{\pm}_{o}} = 5.6 \pm 1\%$. Even allowing for unseen neutral particles, this number never exceeds 10% which by itself means that the trigger carries at least 90% of the total jet momentum.

However, this peculiarity of jets is believed to be a distortion introduced by the single particle trigger at large $-P_t$, that is, the trigger bias effect. To see what this is, we recall that the fragmentation function, D, scales (i.e.: D = D(z)) and ignore, conventionally, the transverse momentum of the partons within the hadrons and of the jet fragments relative to total jet momentum. We may then parametrize the cross section for the production of a pair of equal and opposite transverse momenta $P_t$ as[88] follows:

$$E\, d\sigma/d P_{\perp} = A / P_{\perp}^{N-1} \quad ; \quad P_{\perp} = P_{\perp}^{h^{\pm}_{o}} \tag{III.16}$$

With (III.16) the single particle spectrum at large $-P_t$ is given by the following convolution integral:

$$E d\sigma / dP_L \;=\; \frac{2A}{P_L^{N-1}} \int dz \; z^{N-2} \; D(z) \;; \qquad P_L = P_L^{h^{\pm}} \qquad (III.17)$$

This is true if and only if the fragmentation functions of jets are the same. From (III.17) it is realizable that the single particle cross section has the same power dependence as the jet cross section if and only if D(z) scale with $P_t$. Also N being big means that the small values of z can not contribute much to this integral because of the term $z^{N-2}$ (experimentally[37] $<z> \simeq 0.9$). However, the larger the value of N, the more marked is this trigger bias effect.

However, it is shown that the cross section for triggering on a jet of particles is two orders of magnitude bigger than the cross section for triggering on a particle with the same transverse momentum such that a large ratio R = Jet/single of the order of 100 can be obtained. For the naive CIM we get R = 1, while in the diffused quark model R of order of 100 has the following explanations: In (III.7) $d\sigma/d\hat{t}$ falls off rapidly with transverse momentum of the outgoing quarks with respect to the transverse momentum of the incoming ones. For a fixed $P_L^{h^{\pm}}$, the differential cross section $d\sigma/d\hat{t}$ enhances the configurations in which the internal transverse momenta, $k_{\perp a,b}$, point towards $h_i^{\pm}$ (Diag.III.3a, below) whilst production of $h_i^{\pm}$ would be difficult when the transverse momenta of the partons, $k_{\perp}$'s, are antialigned (Diag.III.3b, below). The enhancing effect of Diag. III.3a exceeds the depressing effect of Diag. III.3b, a net enhancement results. However, all together this effect decreases the transverse momentum on the away side (see Diags. III.3a and III.3c).
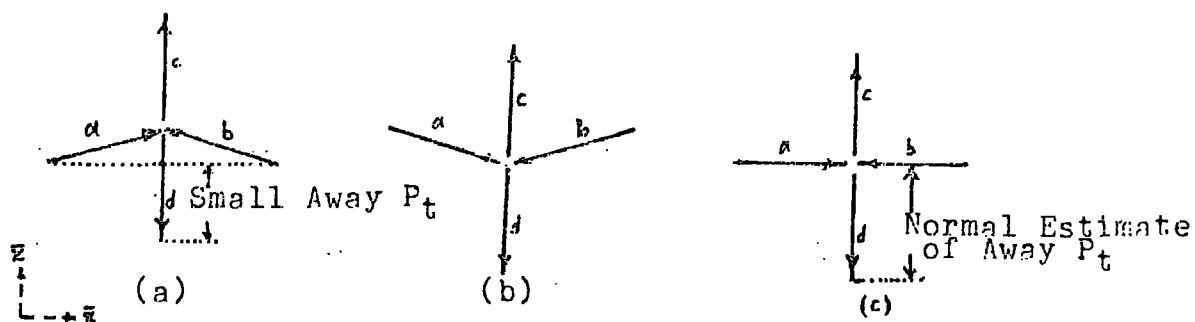
Diag. III.3: Schematic description of the internal
transverse momenta when (a) they are aligned
towards the trigger, (b) they are anti-
aligned, and (c) they are to be normally viewed

The basic internal transverse momentum dependence, in the
formalisms, is carried out by a function like $f_{(k_\perp)}$ when the
transverse momentum distribution is independent of x. This
means that the quark probabilistic function $F(x, k_\perp)$ (i.e. either
quark distribution or quark fragmentation functions) can be
decomposed as;

$$F(x, k_\perp) = \frac{1}{x_R} \times F(x) f_{(k_\perp)} \qquad (III.18)$$

where the carried energy fraction, $x_R$, is defined as:

$$x_{R\,a,b}^2 = x_{a,b}^2 + \frac{4}{s} m_{\perp a,b}^2 \qquad (III.19)$$

For $f_{(k_\perp)}$ mostly an exponential form;

$$f_{(k_\perp)} = b^2 \exp(-b|k_\perp|)/2\pi \qquad (III.20)$$

is chosen such that;

$$\langle k_\perp \rangle = 2/b \qquad (III.21)$$

Choices may typically be; $b = 6$ (GeV/C)$^{-1}$ ($\langle k_\perp \rangle = 330$ MeV/C)
or $b = 4$(GeV/C)$^{-1}$ ($\langle k_\perp \rangle = 500$ MeV/C). Experimentally[75] for
hadrons from quarks, for example, the SPEAR data have been
found     to be fitable to $\exp(-bk_\perp)$ (see Fig. 48a) while for

quark from hadrons $\mu$-pair data (shown in Fig. 48b) suggest a
larger $<k_{\perp}>_{h\to q} \sim 720$ MeV/C than $<k_{\perp}>_{q\to h}$ .

However, by introducing appropriate cut-off, extraordinary
effects of quark transverse momentum can be minimized.
Feynman et al (FFF)[8] by introducing a very large $\bar{s}$ and $\bar{t}$ cut
off ( $M_{\bar{s}}^2 \sim 12\ GeV^2$ , $M_{\bar{t}}^2 \sim 2$ For $<k_{\perp}>_{h\to q} \sim 500$ MeV/C ) in their
modified version of (III.7) namely:

$$d\bar{\sigma}/d\bar{t} \sim 1/(\bar{s}+M_{\bar{s}}^2)(M_{\bar{t}}^2 - \bar{t})^3$$

(III.7a)

force the hard scattering of quarks still to be the dominant
one.

(III.4c)   The $P_{out}$ Distribution

The most sensitive experimental quantity to the transverse
momentum of the quarks within the initial hadrons is the degree
to which the collision deviates from coplanarity. This is
called the $P_{out}$ distribution (or $\phi$ distribution of Fig. 39).
The shown data on this in Fig. 41 are too broad. This may be
because of considering it without paying attention to the
transverse motion of the partons in the naive parton picture.
However, by consulting (III.18) it has been argued that,
first of all, away side outgoing quark receives $P_{out}$ (see
Diag. III.2) (from $<k_{\perp}>_{h\to q}$ and from the trigger side jet
hadron transverse momentum spread, $<k_{\perp}>_{q\to h}$ ), which, secondly
is transferred to the hadrons fragmenting from this away quark
(after being scaled down by $x_e$, the ratio of hadrons momentum
relative to the quark momentum (see Diag.III.2)). Also the
fragmented hadrons receive a component due to $<k_{\perp}>_{q\to h}$ .
Hence;

$$P_{out} = x_e \times p_q^d + <k_{\perp}>_{q\to h}$$

(III.22)

which with respect to momentum conservation demanding for the validity of $P_j^d = P_j^a + P_j^b - P_j^c$ where $P_j^c = <k_\perp>_{q \to h} / z$ , we get:

$$< P_{out} > = x_e \left( <k_\perp>_{h \to q}^2 \; z + \frac{1}{2} (x_e^2 + 1) <k_\perp>_{q \to h}^2 / x_e^2 \right)^{1/2} \qquad (III.23)$$

This is calling for the dependence of $< P_{out} >$ on $x_e$. However if $< k_\perp >_{q \to h} \sim 330$ MeV/C (see Fig. 35) and $< k_\perp >_{h \to q} \gtrsim 500$ MeV/C then,[82] $x_e$ dependence of $< P_{out} >$ is quite clearly evident from Fig. 49 for the validity of (III.23).

### (III.4d) The Towards Component Structure

For the CIM to have the chance of predicting the experimental data this model has been extended as such that, for instance, in terms like $Q + M \to Q + M$ the system M can emerge either as a single stable meson or as an excited $q\bar{q}$ system, that is a resonance. To accept so, it is necessary to introduce a decay function $D_{M*}^{h_o^{\pm}}$ to fit the data, and, hence, exhibit that the produced associated particles to be just the remaining decay products of the aforementioned system M. This D-function, which is similar to the one shown previously for the diffused quark model, spoils[75] the successful single particle cross section predictions of this model (it changes the power of (1-x ), see (III.11)). Also practically the resonances are absent in the invariant mass spectra of Fig.37. On the other hand, in the diffused quark model the repeatation of the spectra of the scattered parent parton could be an explanation appropriate for interpreting the coincidence of the data in Fig. 36. However, the two particle cross sections can be obtained[82] from (III.8) with respect to the following mechanism in parton picture;
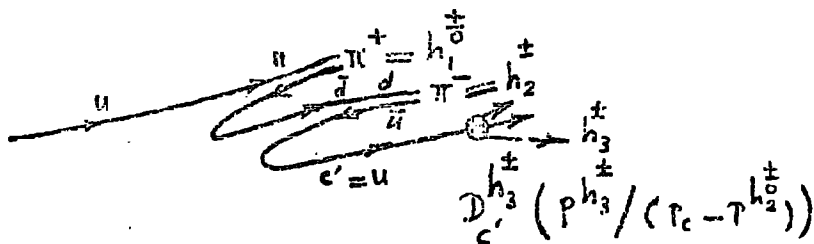
Diag.III.4: Unambiguous mechanism for
trigger meson with a valence quark structure

where the D-function in (III.8) now reads as:

$$\mathcal{D}_q^h(z) \rightarrow \mathcal{D}_q^{h_1 h_2}(z_1 z_2) = \mathcal{D}_q^{h_1}(z_1) \mathcal{D}_{q_2}^{h_2}\left(z_2/(1-z_1)\right)\big/(1-z_1) \qquad \text{(III.24)}$$

For the case of Diag.III.4, for instance, $z$, $z_1$, and $z_2$ read
as follows: $z = \dfrac{p^{\pi^+} + p^{\pi^-}}{p_u} = \dfrac{p^{\pi^+} + p^{\pi^-}}{p^{\pi^+}}$ , $z_1 = \dfrac{p^{\pi^+}}{p_u}$ and $z_2 = \dfrac{p^{\pi^-}}{p_d} = \dfrac{z\,p^{\pi^-}}{p^{\pi^-}\cdot(1-z)p^{\pi^+}}$
These determine the $z \rightarrow 1$ behaviour of the D-function since
we can have $(1-z_1) = (1-z)\left(p^{\pi^+} + p^{\pi^-}\right)\big/\left(p^{\pi^-} + p^{\pi^+}(1-z)\right)$. Now, by being
concerned just, for example, with the high $P_t$, pion productions,
we suppress configurations containing the same charge combina-
tions with respect to those which contain the unlike charge
combinations. This is done in account of the smallness of,
say, $p_d^{\pi^+}$. Also we accept a faster decrease for $\mathcal{D}_u^{\pi^-}$ relative
to $\mathcal{D}_u^{\pi^+}$ to be due to the production of (++) being smaller than
(+-). However, based on these ideas are the presented[82]
theoretical predictions for the rapidity spectrum of associated
particles in Fig. 50.

In this model there exists also a factor of six rise
between $\sqrt{s} = 19$ and 53 GeV for secondaries with $P_t > 1$ GeV/C,
while for secondaries with $P_t > 0.3$ GeV/C it is only a factor
of about 2.5. Quantitatively, this has been related to the
increase of the lower bound of the $z$ integration in (III.8)
reflecting the gradual flattening of the single particle $P_t$
distribution with increasing energy. This can be seen from

Fig. 51 showing[75] a measurement of the charged particles produced in association with a single particle $\pi^0$ trigger at $90°$.

With noting that the consideration concerning Fig. 40 can also be considered for towards particles, it can be seen from the figure that the toward multiplicity is higher for the proton trigger than for the pion trigger. It is because of the faster decrease of $D_q^p$ relative to $D_q^{\pi^+}$ when $z \to 1$, namely, a proton carries a lower fraction of the parent parton momentum than a pion, and, therefore, leaves more energy for other particles to be produced in the following certain form of production;

$$< N_{towards} > \sim Log\left(\frac{1}{<z>} - 1\right) \frac{P_\perp^{h^\pm_0}}{Sin\,\Theta} \qquad (III.25)$$

This means that the compensation of the increase of $< z >$ with $T_\perp^{h^\pm_0}$ is done by the $P_\perp^{h^\pm_0}$ factor itself. Apart from practical absence of the existence of double-charged (or many particle) resonances corresponding to the double charge correlation in the CIM model, above idea concerning multiplicity can be argued to be valid in the constituent interchange model as well.

(III.4e)  Away Component Structure

(III.8) should be modified in the presence of the away component for which we can have:

$$\frac{d^3 T_d}{E_d} \to \int_0^1 d\nu \, D_q^{h_1}(\nu) \frac{d^3 T_{h_2}}{E_{h_2}} \qquad ; \quad \nu = x_e z \qquad (III.26)$$

Therefore (III.21) could read now as:

$$d\sigma \left/ d^2 f_{\perp h_1} d^2 f_{\perp h_2} d^2 \Im_{h_1} d^2 \Im_{h_2} \right. \propto \int dz \, d\delta \, G_{a/A}(x_a) G_{b/B}(x_b) \frac{z}{\pi} \frac{d\hat{\sigma}}{d\hat{t}} D_c^{h_1}(z) D_d^{h_2}(x_e z) \qquad (III.27)$$

where with respect to the relation $P_a + P_b = P_c + P_d$ it may be proved that:

$$x_a = \left(\frac{m_{\perp c}}{z\sqrt{s}} e^{\vartheta_c} = \frac{x_1}{z}\right)\left(1 + exp(-\delta)\right) \tag{III.28}$$

$$x_b = \left(\frac{m_{\perp c}}{z\sqrt{s}} e^{-\vartheta_c} = \frac{x_2}{z}\right)\left((1 + exp(\delta)) = \frac{\bar{s}}{t}\right) \tag{III.29}$$

$$\delta = \vartheta_c - \vartheta_d , \quad \frac{z}{z-x_1} \leqslant (1+e^\delta) \leqslant \frac{z}{x_2} , \quad x_R = x_1 + x_2 \leqslant z \leqslant 1 \tag{III.30}$$

However, if for $A + B \longrightarrow (h^{\pm}_0 = h_1) + (h^{\pm} = h_2) + x$ (A and B are protons) $G_{\alpha/\beta}$ goes to zero at the lower and upper bounds of the allowed region (III.30), and as we can have $G_{\alpha/\beta} \sim (1-x)^3$, then the maximum can be shown to be at the point of rapidity equal to what follows:

$$exp(2\delta_{max}) = \frac{(1-x_2)x_1}{(1-x_1)x_2} \tag{III.31}$$

or equivalently at

$$\vartheta_{h_2 max} \sim -(x_\perp Sh\vartheta_c)/2 \tag{III.32}$$

We see that the peak should be centred near $\vartheta_{h_2} \sim 0$ and shifted a little opposite to $\vartheta_h$ if $x_\perp$ is small. This is the case of the maximal peripherality, because shifting of the peak to the trigger side occurs - in the diffused quark model of Feynman et al (FFF) - if the differential quark scattering amplitudes read as (III.7) being symmetric about $\vartheta_{h_2} = 0$ in agreement with experiment, see Fig. 52. From Fig. 52a it is clear that the experiment is lower than the theoretical curve. However by choosing $< k_\perp >_{h \to q}$ greater than 330 MeV/C (or nearly equal to 500 MeV/C) the size of theoretical curve goes down in becoming comparable with experiment.

From Diag.III.1 it is evident that the situation on the away side of the diffused quark model of FFF and CIM of EBG looks similar with each other. For instance their predictions

for normalization on the away side is similar. However, with the normally quoted form for the CIM model we get a "back antiback" theoretical prediction for the away side rapidity shape shown in Fig. 52b, which is clearly in disagreement with experiment. Recent[75] proposal which concerns this point agrees more with a form as like as (III.7) for spin $\frac{1}{2}$ quarks.


### III.5  Many Particle Events

#### (III.5a)  Many Particle Trigger Experiment

It is believed that in measuring the total hadron energy deposited in a given solid angle and therefore the total jet energy (independent of its unknown fragmentation function, D) no trigger bias could affect the experimentation. This sort of measurement, however, has been done by using a hadron calorimeter at FNAL[89] (experiment E 260). The device contains two four-section calorimeters. Each of these calorimeters triggers when the total $P_t > 0.75$ GeV/C. Moreover, what is suggestive of a jet trigger can be seen in Fig. 53b denoting a sum over all events in sections of one of the calorimeters as a jet event at large $P_t$. Also, triggering on a single particle trigger had been done under satisfying the condition of having a signal from any one section to exceed a preset transverse momentum bias of 3 GeV/C - see Fig. 53a where the second section in the left x-axis calorimeter shows a single trigger $P_t$ of 3.81 GeV/C. A typical E 260 jet, shown in Fig. 53b, consists of ( $4 \leqslant T_L^{Jet} \leqslant 5 \; GeV/c$ ).

    (i)   Charged hadrons (mean charged

           multiplicity three)               57%

    (ii)  Photons ( $\pi^0, \eta$ decay)        30%

    (iii) Neutral hadrons         ( $13 \pm 8$ )%

(III.5b)  Many Particle Event and Specific Models

We first recall that the ratio of the jet cross section
to the single particle cross section (R = Jet/Single particle)
can be expected to be R = 1 in the naive constituent inter-
change model.  This is not certainly confirmed by the reported
preliminary results of E 260 from a short run on a Beryllium
target (at momenta up to 200 GeV/C).  The R which is predicted[99]
to depend on $x_{\perp}$ and $\theta_{c.m.}$, for $\theta_{c.m.} \sim 90^o$ is about 370 at
$x_{\perp} = 0.4$ and rises to 1000 at $x_{\perp} \sim 0.7$.  This is just the
order of magnitude we expected from previous discussion on
the trigger bias.  Particularly the jet cross section in Fig.
54 which is greater than 100 times the cross section for producing
charge particles (summed over all charges), is in excellent
agreement with the diffused quark model predictions of Feynman
et al (FFF).  This means that the jets observed in hadron-
hadron collisions should arise from the fragmentation of quarks
just as the jets in lepton-hadron processes.  To show that this
last statement is a fact, there should be resemblance between
the distribution of hadrons within hadron- and lepton-
initiated processes if quarks fragment into the hadrons in a
universal manner.  Indeed, as it is seen from Figs. 55a and 55b,
there are similarities between the unbiased inclusive z-distri-
bution of the charge jet fragments of Fig. 55a and the similar
distribution of quark jets , induced by lepton processes, of
Fig. 55b.  To see this conclusion more firmly, we continue the
comparison of E 260 data with the predictions of the two models
about them.

## (III.5c)  Comparison of Jet and Single Particle Triggers

"A particle trigger on one side see a jet on the other side, while a jet trigger should produce out a single particle on the away side," this is what can be imposed on us if we want to compare the jet and single particle triggers in constituent interchange model of BBG which is in sharp contrast with what has been observed experimentally by E 260 preliminary data. Namely the failure of CIM, this time, is indeed so much the worse than the previous times. On the other hand, the only difference, in the diffused quark model of FFF, between a jet and single particle trigger - due to their original quark momentum $Z_c$ - can be appropriately removed and, hence, have the experimental results reproduced (see Fig. 56). As is the case in Fig. 56, when jets are triggered on directly, instead of the variable $X_e = -P_x^{Away\ Hadron}$ $P_t^{Trigger} = -P_x / <z_c> P_t^{Jet\ Trigger}$ we may use directly the variable $z = -P_x / P_t^{Jet}$ for describing the away jet fragmentation. However, in the case of two identical jets with $P_t$ (Towards jet) $= P_t$ (Away jet)(i.e.: $k_t = 0$, see Diag.III.3c) an identical z distribution of the trigger side and of the away side, namely:

$$\left(\frac{d\sigma}{\sigma\, dz}\right)_{Away} \equiv \left(\frac{d\sigma}{\sigma\, dz}\right)_{Towards} \tag{III.33}$$

is expected. On the other hand, if the mechanism of Diags.III. 3a,b is at work (i.e.: $k_t \neq 0$), then;

$$\left(\frac{d\sigma}{\sigma\, dz}\right)_{Away} < \left(\frac{d\sigma}{\sigma\, dz}\right)_{Towards} \tag{III.34}$$

What is judging this discrepancy, however, is the experimental away z distributions on Fig. 57 for two different values of $P_t$(jet). The towards z distribution is represented by the dashed curve on this figure which is standing above the away

distribution in favour of the mechanism of Diags.III.3a,b
(i.e.: $k_t \neq 0$).

## III.6  Conclusion

In this chapter experimental results of the single- and
many-particle hadronic events at high transverse momentum have
been interpreted from the viewpoints of the following three
main theoretical notions (see Sec. (III.2c)):

| | | |
|---|---|---|
| (i) | Quark Model (QM) | $q+q \rightarrow q+q$ |
| (ii) | Quark Fusion Model (QFM) | $q+\bar{q} \rightarrow M+M$ |
| (iii) | Constituent Interchange Model (CIM) | $q+M \rightarrow q+M$ <br> $\bar{q}+M \rightarrow \bar{q}+M$ |

However, from what is known as the counting rules (see Sec.
(III.2b)), we see that the first of these theoretical models
contains four elementary fields (= Quarks) giving cerainly a
very poor theoretical fit to the inclusive spectra at high
$P_t$, because these kind of experimental results are behaving
much more like (III.1) with $N = 8$ (see the first chapter).
This means the involvement of not more than six elementary
fields in the favour of the other two theoretical models,
(ii) and (iii). However, of these two (QF and CI) models
the CIM also has been capable of predicting some other aspects
of the experimental results;  such as the beam ratios, a
subject which has already ruled out the quark fusion model
(see Sec. (III.4a)).

From the many particle experiments view point, on the
other hand, there is no evidence to confirm the predictions of
the naive CIM, namely that the away side from a jet should be
a single particle, but that the away side a single particle
trigger is a jet (see Sec. (III.5a)). Instead there are
experimental evidences[91] in favour of a two-jet structure of

large $P_t$ events which are similar to those seen in the lepton-nucleon interactions (see Sec. (III.5)). This means also that the jets in the large $P_t$ events must be quark jets. Therefore, it is concluded that the first theoretical model, the QM, is the only one which is worth modifying to fit the data. In this way the quark-quark elastic differential cross section given by (III.7) is preferred over a form such as (III.3) for predicting the experimental results correctly.

By recalling that indeed the gluons exist (see Secs. (II.5c) and (II.6d)) we may claim that some of the produced particles at large $P_t$ may be the results of the interactions of gluons. In fact, these type of reactions (namely - if g stands for the vector gluons; $gg \rightarrow gg$, $gg \rightarrow q\bar{q}$, $g\bar{q} \rightarrow g\bar{q}$, $gq \rightarrow gq$, $q\bar{q} \rightarrow gg$, $q\bar{q} \rightarrow q\bar{q}$, $\bar{q}\bar{q} \rightarrow \bar{q}\bar{q}$, and $qq \rightarrow qq$ which for each to the lowest order in the perturbation theory a calculated cross section exists[92,93]) approximately contribute a $P_t^{-4}$ to the invariant cross section. However, even by regarding the quatum chromodynamic processes we cannot predict those experimental features which are at $P_t > 5$ GeV/C where nearly a $P_t^{-6}$ dependence for the inclusive spectra (at $P_t \sim 17$ GeV/C) has been found.[84] One more difficulty is that neither the proportionality factor A of (III.7) which is too large nor the quark-gluon coupling constant which is given as: $\alpha_s(Q^2) = 0.5/(1 + 0.36 \log \frac{Q^2}{4})$ can be produced by any theoretical argument. Hence, as is clear, our theoretical models still need some correction to explain the entrie data.

# APPENDIX A

## Cross Sections: Two-Body Kinematics[7,20,35]

In what follows the free particle states are normalized to one particle per unit volume. The phase for a single particle is thus $d^3P/(2\pi)^3$ .

## 1. Two particle collision cross sections

$$\alpha = (1,2) \quad ; \quad \} = (3,4,\cdots\cdots,n+2)$$

### A.1 - Invariant or Feynman Amplitude M

The invariant amplitude, M. is related to the s-matrix through:

$$S_{fi} = \delta_{fi} - i\,(2\pi)^4\,\delta^4(P_f - P_i)\,M_{fi}\Big/ \sqrt{\prod_j 2E_j} \tag{A.1}$$

where $\alpha$ and $\}$ are the labels for the initial and final states and products of factors $(2E_j)$ is over all the particles in $\alpha$ and $\}$ states. The implicit in the s-matrix element are the conservation of energy and momentum delta functions. M has these factors excluded. Its various arguments are thus to be evaluated taking the conservation laws into account. With the presence of the square root of the ($\prod_j 2E_j$ ) and the single particle normalization stated above, M is Lorentz invariant.

### A.2 - The differential x-section

It can be written in its following invariant form where the projectile and the target are labelled, respectively # 1 and # 2.

$$d\sigma_{fi} = \frac{(2\pi)^4\,|M_{fi}|^2}{4\left((P_1\cdot P_2)^2 - m_1^2 m_2^2\right)^{1/2}} \prod_{j=3}^{n+2} \frac{d^3P_j}{(2\pi)^3\,(2E_j)}\,\delta^4\left(\sum_j P_j - P_i\right) \tag{A.2}$$

The factor $\left( (P_1 \cdot P_2)^2 - m_1^2 \, m_2^2 \right)^{1/2}$ is called flux factor. The differential x-section can be expressed per unit interval in invariant momentum transfer $t = (P_1 - P_3)^2 = (P_2 - P_4)^2$ as:

$$\frac{d\sigma}{dt} = \frac{\pi}{P'_{c.m.} \, P_{c.m.}} \frac{d\sigma}{d\Omega_{cm}} = \frac{1}{64 \, \pi \, s \, P_{cm}^2} \left| M_{fi} \right|^2 \qquad (A.3)$$

Note that $s P^2_{cm}$ is just the square of the invariant flux factor.

For elastic scattering the standard c.m. scattering amplitude $f_{c.m.}$ is related to the invariant amplitude by:

$$f_{c.m.} = -M / 8 \pi W \qquad (A.4)$$

For inelastic two-body processes conventions vary, but usually an additional factor $\left( P'_{c.m.} / P_{c.m.} \right)^{1/2}$ appears on the right-hand side of (A.4).

## 2. Two-Body Kinematics

The general notation is indicated in Diag. A.1 for the process $m_1 + m_2 \longrightarrow m_3 + m_4$:
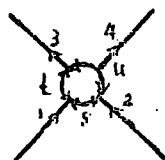


Diag. A.1

The invariant s, t, u, are defined by

$$
\begin{aligned}
s &= (P_1 + P_2)^2 &= (P_3 + P_4)^2 \\
t &= (P_1 - P_3)^2 &= (P_2 - P_4)^2 \\
u &= (P_1 - P_4)^2 &= (P_2 - P_3)^2
\end{aligned}
\qquad (A.5)
$$

with the constraint equation:

$$s + t + u = \sum_{i=1}^{4} m_i^2 \qquad (A.6)$$

In Lab frame where the particle 2 is at rest, the invariants are:

$$s = m_1^2 + m_2^2 + 2m_2(E_1)_{Lab}$$
$$t = m_2^2 + m_4^2 - 2m_2(E_4)_{Lab}$$ 
$$u = m_2^2 + m_3^2 - 2m_2(E_3)_{Lab}$$

(A.7)

For reactions in which $m_4 = m_2$ or elastic scattering, the momentum transfer t simplifies to: $t = -2m_2(T_4)_{Lab}$ where $T_4$ is the kinetic energy of the recoiling particle # 4.

In c.m. frame where energies and momenta of particles are $E_1$, $E_2$, $E_3$, $E_4$, and $P_1 = P_2 = P$, $P_3 = P_4 = P'$, then, $W^2 = S = (E_1 + E_2)^2 = (E_3 + E_4)^2$ and the two momentum transfer variables are:

$$t = t_{min} - 2PP'(1 - \cos \Theta_{c.m.}) \; ; \; t_{min} = (E_1 - E_3)^2 - (P - P')^2$$

$$u = u_{min} - 2PP'(1 + \cos \Theta_{c.m.}) \; ; \; u_{min} = (E_1 - E_4)^2 - (P - P')^2$$

(A.8)

$\Theta_{cm}$ is the angle between $\underline{P}_1$ and $\underline{P}_3$.

In c.m. $(\underline{P}_1 \cdot \underline{P}_3)$ can be expressed in terms of the invariants s, t, u, in the s-channel of Diag. (A.1) as follows:

$$4 P_s P_s' \cos \Theta_s = t - u + \frac{(m_1^2 - m_2^2)(m_3^2 - m_4^2)}{S}$$

(A.9)

For the t- and u-channel processes, where t and u are, respectively, the squares of the total c.m. energies in these channels and the other invariants are momentum transfers, the corresponding expressions are:

$$4 P_t P_t' \cos \Theta_t = s - u + \frac{(m_1 - m_3)^2 (m_2 - m_4)^2}{t}$$

$$4 P_u P_u' \cos \Theta_u = t - s + \frac{(m_1^2 - m_4^2)(m_3^2 - m_2^2)}{u}$$

(A.10)

The angle $\Theta_t$ is that of $\bar{2}$ and 1 in the c.m. of the t-channel of the process $1 + \bar{3} \rightarrow \bar{2} + 4$. $\Theta_u$ is the angle between $\bar{1}$ and 3 in the process $\bar{3} + 2 \rightarrow \bar{1} + 4$.

## APPENDIX B

## Kinematic and X-Section of Inclusive Processes[7,20,36]

For the simplest inclusive reaction (I.1b)
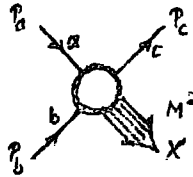


Diag. B.1

we specify the frame of reference, the number and types of variables, and the x-sections.

### B.1 The Lorantz Frame

Commonly used are the Laboratory (Lab), antilaboratory (anilab), and centre-of-mass (c.m.) frames. In what follows, only quantities in the c.m. will not be denoted by any subscripts.

### B.2 Independent variables

With given masses of a, b, and c and unpolarized beams, we need only three kinematical variables: energy, transverse, and longitudinal variables, to describe the X-section. The transverse is defined with respect to longitudinal axis given by the incident particle directions in the c.m.
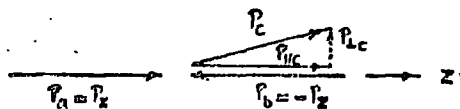


Diag. B.2

Also similarly in the other Lorentz frames only $P_{||}$ changes, $P_t$ is invariant to boost along the beam direction.

(B.2.1) For the energy variable, we may use either $P_{a\ lab}$, the total c.m. energy W, or its square:

$$S = (P_a + P_b)^2 = W_c^2 \qquad (B.1)$$

(B.2.2) For the transverse variable we may use the transverse momentum of particle c:

$$P_{\perp c} \equiv P_{\perp} = P \sin \theta = P_{c\ lab} \sin \theta_{c\ lab} \qquad (B.2)$$

where P and $\theta$ are c.m. momentum and production angle of particle c; $P_{c\ lab}$ and $\theta_{c\ lab}$ are the corresponding quantities in the Lab system.

The invariant four-momentum transfer is:

$$t = (P_b - P_c)^2 \qquad (B.3)$$

which for $x \sim 1$ (see below) and when $m_a = m_b = m_c$, $T_{c\ lab}$ is small, then the four momentum transfer is given by:

$$t \longrightarrow -P_{c\ Lab}^2 \sim -P_{\perp}^2 \qquad (B.4)$$

In any Lorentz frame $\mathcal{E}$ moving uniformly parallel to the incident direction - say, z-axis-particle c naturally has the three momentum $\underline{P}_c$ with components $P_{||}$ and $\underline{P}_t$. Now, if there is another Lorentz frame $\mathcal{E}'$ moving with a relativistic velocity parallel to the z-axis in which particle c has only transverse component of momentum, $\underline{P}_c' = \underline{P}_t$, then the energy of particle c is $E_c' = m_t$ where:

$$m_{\perp c} := ( \underline{P}_{\perp c}^2 + m_c^2 )^{1/2} \qquad (B.5)$$

is sometimes called the transverse or longitudinal mass and is denoted by $w_c$, $\mu$, or K. Metrics are chosen so that $P_i^2 = m_i^2$

which helps to have the effective mass associated with the longitudinal momentum if we use it in B.5;  i.e.:

$$E_c^2 = P_{c\parallel}^2 + m_{\perp c}^2 \tag{B.6}$$

(B.2.3) For the Longitudinal variables of which are the following where quantities are all referring to particle c whose subscript will be omitted:

1. Longitudinal c.m. Momentum

$$P_\parallel = P \cos \Theta \tag{B.7}$$

2. Missing mass

$$M^2 \equiv M_x$$

$$= S + m^2 - 2E\sqrt{S} \xrightarrow[S \partial M^2 \gg]{} \tag{B.8}$$

$$\frac{M^2}{S} \approx 1 - \frac{2P_\parallel}{\sqrt{S}} \tag{B.9}$$

3. Feynman x-variable

$$x \equiv \frac{P_\parallel}{P_\parallel^{max}} \qquad ; \quad -1 < x < 1 \tag{B.10}$$

$$\xrightarrow[S \gg]{} \frac{2P_\parallel}{\sqrt{S}} \quad \text{or} \quad 1 - \frac{M^2}{S} \tag{B.11}$$

(B.10) and (B.11) are equivalent only to the extent that $M_{a,b,c}$ and $|P_t|$ can be neglected compared with s and $M^2$. Clearly $x_a \sim 1$ and $x_b \sim -1$, and if $x \sim 1$ it means that c has acquired most of the momentum of a, c is a 'fragment' of a, or if $x \sim -1$, c is a fragment of b. The "central region" $x \sim 0$ implies that c is approximately stationary in the c.m. and so is not directly connected with a or b.

4. c.m. Rapidity variable

$$y_c = \frac{1}{2} \log \frac{E + P_\parallel}{E - P_\parallel}$$

$$= \log\left((E + P_\parallel)/m_\perp\right) \xrightarrow[P_\perp^2 \gg m^2]{} -\log\left(\frac{1}{2}\frac{\Theta}{2}\right) \tag{B.12a}$$

With the range of variability as:

$$y_a + \log \frac{m_\perp}{m_a} \leqslant y_c \leqslant y_b + \log \frac{m_b}{m_\perp} \tag{B.12b}$$

5. Lab rapidity variable

$$y = y_{Lab} = y_{ac} = y_a - y_c \tag{B.13a}$$

With the range of variability as:

$$\log \frac{m_\perp}{m_a} \leqslant y_{ac} \leqslant \log \frac{S}{m_\perp m_1} \tag{B.13b}$$

Formula (B.12b) and (B.13b) are valid in the limit of large s. We add that the extreme values of (B.12a) occur when $P$ reaches its extreme values (which occur when $M^2 \rightarrow 0$ and $E \approx \sqrt{s}/2$, $P_{\parallel} \approx \pm \sqrt{s}/2$, $|P_\perp|$ are negligible). Then, (B.12b) can be rewritten as follows:

If $\quad y_{c\ max} = \frac{1}{2} \log\left(\frac{s}{m_\perp^2}\right) \quad$ et $\quad y_{c\ min} = -\frac{1}{2} \log\left(\frac{s}{m_\perp^2}\right)$

Then range of $y_c$ is:

$$Y_c = y_{c\ max} - y_{c\ min} = \log\left(\frac{s}{m_\perp^2}\right) \qquad\qquad \text{(B.12b)}$$

$y_c$ will be maximum when C is a fragment of a; i.e.: c takes on the longitudinal momentum of a, while $y_c$ will be in its minimum value when c takes on the longitudinal momentum of b - hence, c will be a fragment of b. $y_c = 0$ corresponds to c being at rest in the c.m.

In terms of central and peripheral collisions, the central region arises from the central part of collisions which is mainly occupied by pions with low c.m. momenta, while the other two fragmentation regions arise from the peripheral parts of the collisions.

Table B.1: Frame of Reference and Set of Variables Often Used for the Analysis of Inclusive Reactions

| Frame | Set of Variables | | |
|---|---|---|---|
| Target or Lab Frame (rest frame of particle b) | $P_{a\ lab}$, | $\theta_{c\ lab}$, | $P_{c\ lab}$ |
| | $P_{a\ lab}$, | $P_t$ | , $y_{c\ lab}$ |
| Projectile or Anti-lab Frame (rest frame of particle a) | Symmetric of Lab frame | | |
| C.M. Frame | W, | $\theta_c$, | $P_c$ |
| | s, | P, | $P_c$ |
| | s, | P, | x |
| | s, | P, | T |
| | s, | t, | $M^2$ |

### B.3 Phase-Space: Invariant X-Sections

The single-particle inclusive X-section is given by (A.2) integrated over all final state momenta except particle c and summed over all final states $f$ which contain c and are kinematically allowed. The cross section thus appears as:

$$d\sigma_{ab}^{c} = \frac{Lorentz\ Invariant}{Flux\ Factor}\ \frac{d^3P_c}{E_c} \tag{B.14}$$

By defining the invariant differential cross section for (ab ⟶ c anything else) as:

$$f \equiv f_{ab}^{c} = E_c\ d^3\sigma_{ab}^{c}/d^3P_c \tag{B.15}$$

and by using the different interrelation of the invariant phase space $d^3P/E$ which may be given as follows:

$$d^3P/E \simeq dP_{\perp}^2 dP_{\parallel}/E \simeq dP_{\perp}^2 dy \simeq dx\, dP_{\perp}^2/x \simeq dx\, dt \simeq dM^2 dt/s \tag{B.16}$$

(B.15) may be written in the following alternative forms where the quantities are all referred to as c;

$$f = \frac{E\,d^3\sigma}{d^3P} = \frac{E\,d^2\sigma}{\pi\,dP_{\parallel}dP_{\perp}^2} = \frac{d^3\sigma}{\pi\,dy\,dP_{\perp}^2} = \frac{s\,d^2\sigma}{\pi\,dt\,dM^2} = \frac{2E\,d^2\sigma}{\pi\,\sqrt{s}\,dx\,dP_{\perp}^2} \tag{B.17}$$

Here, presence of factor $\pi$ is for giving the cross section per unit azimuthal angle.

# APPENDIX C

Theoretical Framework Assuming a Finite
Correlation Length: Scaling and Limiting
Fragmentation Hypothesis: Optical Theorem
and its Generalization: Factorization:
Some Theoretical Models

## C.1 Theoretical Framework Assuming a Finite Correlation Length

If the phase space $dy\,d^2P_{\perp}$ represents $(P_t, y)$ space of multiparticle production processes, then, the base length, y, of this space is limited by the possible kinematical range of variable y, while its height is limited by the dynamical effects on $P_t$. In this plot, by making the hypothesis of the existence of a correlation length in rapidity over which a given particle can be influenced by another one, L (hypothesis[37] of short range order) the single particle spectra in different regions may be separated. For instance, it may be assumed that two particles produced in a high energy interaction are uncorrelated if this relative rapidity is larger than L, and then accordingly define the following three regions:
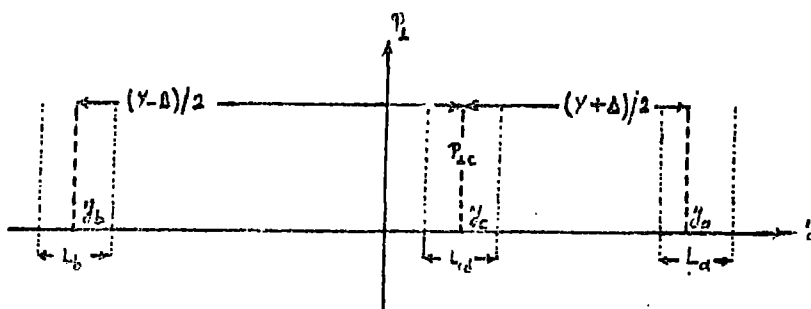


Diag.C.1: Illustration of different regions in the $(P_t, y)$ space:

Target fragmentation of fixed length L about $y_a$.

Projectile fragmentation of fixed length L about $y_b$.

Central region of length $\approx$ logs (actually this is predicted to be as lengthy as Y-2L).

If $L \sim 2$, then the central region starts[8] to develop only for laboratory momenta larger than 100 GeV/C. At lower energies we have only fragmentation of ingoing particles.

Of the immediate consequences of this hypothesis are the scaling[39] and limiting fragmentations[38] discussed below.

(C.la)  <u>Limiting Fragmentation and Scaling at finite x</u>

W.r.t. (B.12) and (B.13), $f_{ab}^c = f_{ab}^c ( y_a - y_b , y_c - y_a , p_\perp )$ depends on three variables;  the first being equivalent to the c.m. energy, $W$, and the other two to the momentum $\underline{P}$ of particle c in a frame related to the incident particles. However, the assumption of a finite range of correlation implies that:  if $S(Y)$ is large enough, the produced particle c would not know the position and type of particle b on the rapidity axis;

$$\lim_{\substack{Y(S) \to \infty \\ y_c - y_a \ Fixed}} f_{ab}^c ( y , y_c - y_a , p_\perp ) = f_a^c ( y_c - y_a , p_\perp ) = f_a^c ( x , p_\perp ) \qquad (C.1)$$

The first form in (C.1) is the statement of Limiting Fragmentation[38] of particle a, while the second  equivalent form is the statement of Feynman Scaling[39] in the region $x > 0$.

Similarly, we may write down the statement for production of particle c in the vicinity of particle b when $x < 0$.

(C.lb)  <u>Central Region</u>

In central region of Diag. C.1 and while the produced particle is many correlation lengths away from either projectile or the target, then, the produced particle does not know what are the situations of the incident particles with respect to the rapidity axis as $S(Y) \longrightarrow \infty$ ;

$$\lim_{\substack{Y \to \infty \\ y_c - y_b \gg L_b \ a \ y_a - y_c \gg L_a}} f_{ab}^c ( y , y_{cm} , p_\perp ) = f_{ab}^c ( p_\perp ) \qquad (C.2)$$

In this region the invariant cross section is seen to be flat and depends on the incident particles a and b only.

## C.2 Optical Theorem and Its Generalization[7,35,40]

Of the relation which is satisfied by total cross section ab → X is the so called optical theorem. In brief, if
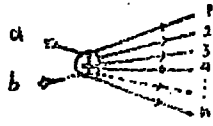
 is the diagrammatical representation of the ampli-

tude of $\sigma^{tot}(ab \to x)$, then $\sum_n$  $\sim \sigma_{ab}^{tot}(s)$ which is
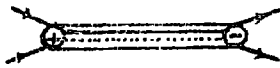
naturally obtained from multiplication of the amplitude by its complex conjugate and summation over all possible intermediate states. Now, if the amplitude  is Hermition (or real) analytic, then taking the discontinuity across the branch cut associated with particles in the intermediate state (compatible with conservation of 4-momentum) of our elastic amplitude ab → ab in the forward direction ( $\theta_s = 0$  $t = 0$ , where subscript s refers to the reaction in s-channel) is possible; i.e.:

$\sigma_{ab}^{tot}(s) \sim Disc$  . Notice however, that the real analyti-

city of amplitude implies that: Disc(amplitude)= Im(amplitude).

As it is seen a complicated situation (i.e. sum of exclusive processes all with varying energy dependences) is converted into a manageable one (i.e. the energy dependence of just a single physical amplitude). This advantage has been tried to be realizable in relating one-particle inclusive cross sections to the discontinuity in the intermediate state of the forward 3 → 3 amplitude which then by itself allows us to make Regge predictions for inclusive distributions. In hoping so, the prediction of the Regge Theory for the asymptotic behaviour of the amplitude of the two-body processes through exchange of a single Regge pole which may be sketched out as:

$$\left[ A(s,t) \sim (s-u)^{\alpha(t)} \left( \underset{s \gg}{\sim} s^{\alpha(0)} \right) \right] \Rightarrow \left( \frac{d\sigma}{dt} \sim \beta(t)\, s^{2\alpha(t)-2} \right) \Rightarrow$$

$$\sigma_{ab}^{tot}(s) \sim \overset{a \quad\quad a}{\underset{b \quad\quad b}{\rule{2cm}{0pt}}} \alpha(t=0) \sim s^{\alpha(0)-2}$$

$$\simeq A + \frac{B}{\sqrt{s}} \qquad ; \qquad \textit{Leading Regge Pole}$$

$$\textit{Pomeron} \qquad \alpha(0) = 1$$

$$\textit{Meson} \qquad \alpha(0) = \frac{1}{2}$$

is in our mind. However the completeness relations helps us to get $f_{ab}^{c}(s,P_c) \sim \sum_{x} \left( \text{diagram} \right)$ the single particle inclusive distribution, after squaring and summing over all possible intermediate states of the inclusive reaction amplitude $\left( \text{diagram } a,b \to c,x \right)$. In turn we see that the analytical continuation of the amplitude from an outgoing c to an incoming $\bar{c}$ is a crossing property which allows us to have $f_{ab}^{c}(s,P_c) \sim f_{ab\bar{c}}^{ab\bar{c}} \sim \sum_{x} \left( \text{diagram} \right)$. Here the applicability of the unitarity equations $S^{+}S = 1 = SS^{+}$ to the particular initial and final states of the process $ab\bar{c} \to ab\bar{c}$, that is:

$$i \left( (\langle f| A^{+}|i\rangle) - (\langle f|A^{-}|i\rangle) \right) = -(2\pi)^{4} \sum_{n} \delta^{4}(P_{n}-P_{i}) \langle f|A^{+}|n\rangle \langle n|\bar{A}|i\rangle \qquad (C.3)$$

where scattering amplitude $A^{+}$ and $A^{-}$ are representing, respectively, + and - bubbles, and being supposed to be Hermiltian analytic, may be used to see how $f_{ab}^{c}(s,P_c)$ can be proportional to the discontinuity of the forward elastic scattering amplitude $ab\bar{c} \to ab\bar{c}$ as: $f_{ab}^{c}(s,P) \sim \text{Disc} \left( \text{diagram} \right)$. Moreover, doing so demands the equality of the initial and final states which means $t_{aa'} = t_{bb'} = t_{cc'} = 0$ where $t_{ii'} = (P_{i} - P_{i'})^{2}$.

## C.3 Factorization

Many theoretical models assume or obtain the factorization property. For instance the finite range correlation picture for n-particle distributions has implicit in it the idea of factorization. Thus in (C.1), f, when normalized to $\sigma_{ab}^{tot}$ , depends on a and c, but not on b, and in (C.2) it is independent of both a and b. Practically, factorization in, say, $(P_t, y_{lab})$ means that the invariant cross section may be written as a product of two independent functions of $P_t$ and $y_{lab}$; i.e.:

$$f(y, P_t, y_{lab}) = F(P_t) G(y_{lab}) \tag{C.4}$$

In Regge language, the factorization is said to be a natural consequence of the assumption of Pomeron-singularity dominance of the total cross sections.

## C.4 Some Theoretical Models

Following a very phenomenological feature of inelastic collisions, that is: the cutoff in the transverse momentum distribution, classification of the models used to predict the particle production spectra may fall into the following two:

(A) Models in which the transverse momentum cutoff
    is a deep consequence of a bootstrap hypothesis
    (e.g.: Thermodynamic Models and Dual Models).

(B) Models in which the transverse momentum cut-
    off is explicitly imposed from outside (e.g.
    Diffractive fragmentation models, Multi-
    peripheral and Regge-exchange Models, Field
    Theoretical Models.)

The following are a list of such models, defined in a very loose way.

(C.4a) <u>Statistical Thermodynamic Models</u>[41]

The reaction products are considered to be originated
from a state of statistical equilibrium of "fireballs",
each one being made of others including particles and
resonances. However, the model considers hadron matter
at "the boiling point" (the limiting temperature - 160 MeV),
where all kinds of objects are supposed to be present inside
the interaction region (or hot spot), because all the c.m.
energy is assumed to be concentrated in a small volume of the
interaction region in a very short time. During this time,
larger energy densities (and thus, mass densities) than
whatever they could originally be, could be found.

(C.4b) <u>Dual Models</u>[42]

It is a requirement of the property of duality that
each term contributing to the scattering amplitude should
be invariant under a cyclic or anticyclic permutation of
the external momenta. Resonances in the s-channel generate
Regge trajectories in the crossed channel. The conjectured
idea is that the "normal" trajectories are generated by
particles and resonances, while the Pomeron trajectory is
built by the non-resonant background part of the amplitude.

(C.4c) <u>Diffractive Fragmentation Models</u>[41]

In general these models describe a reaction in terms
of the excitation of one or of both incident hadrons.
These excited states carry the same quantum numbers of
the corresponding incident hadrons.

Fragmentation models give a picture complementary to
that of the statistical models because they explain the
production of particles at forward and backward angles,

i.e.: in the fragmentation regions. These models, then, give a clear picture of what is happening in the peripheral part of the collision.

## (C.4d) Multiperipheral and Regge Exchange Models[7]

Based on the singly peripheral idea which is abstracted from the factorizability of the amplitude and stablishment of a bound on the momentum transfer, these types of models are illustrated by the multiperipheral graph where the particles in the chain are ordered in such a way so as to minimize the momentum transfers.

## (C.4e) Field Theory Models[43]

The program, here, would be to resolve the inelastic reaction into a sum over infinite sets of Feynman diagrams. However, in these models, hope is to get eventually an eikonal form of the scattering amplitude.

## REFERENCES

1.  G. GIACOMELLI, Proc. of VII Int. Conf. on High Energy
    Phys, NAL, BATAVIA, V3 (72)

2.  V. CHABAUD et al, PL 38B (72) 441, 445, 449

3.  U. AMALDI, 1973 AIX Conf.

4.  V. BARGER et al, Reports RPP/T/12, (72)

5.  S. Y. CHES et al, INDIANA UNIV (72) COO-2009-35

6.  T. T. CHAN et al, PRL 20(68) 1213
    L. DURAND et al, PRL 20(68) 637

7.  See e.g.; P.D.B. COLLINS, An Int. to Regge Theory and
    High Energy Phys. (Cambridge Univ. Press,
    1977)

8.  A.V. BARNES et al, 1974 LONDON CONF.
    V.N. BOLOTOV et al, NP B73(74) 365

9.  E. BRACCI et al, CERN/HERA 72-2 (72a)

10. See e.g.: B.H. BRANDSON, R.G. MOORHOUSE: "The Pion-
    Nucleon Systems" (Princeton Univ. Press,
    1973)

11. N. KWAK, PL58B (75) 233

12. H. de KERRET et al, PL62B (76) 363

13. J.N. PHILLIP et al, PL46B (73) 412

14. S. BRODSKY, High Energy Collisions (Ed. C. Quigg,
    American Institute of Phys, N.Y. 1973)

15. U.P. SUKHATME, Proc. of the 12th Rencontre de Moriond,
    Fline, France

16. J. LACH in 15

17. G. GIACOMELLI, Proc. of the Canadian Institute of
    Particle Phys. Summer School, McGill
    Univ. (73)

18. P. CAPILUPPI et al, NPB70 (74) 1

19. R. HAGEDORN, NC56A (68) 1027, NCS6 (68) 109

20. J. D. JACKSON, 14th SUSSP (1973)

21. G. NEUHOFER et al, PLB38 (72) 51

22. V. V. AMROSOV et al, NPB58 (73) 77

23. W. R. FRAZER et al, RMP44 (72) 284

24. E. L. BERGER, PRL29 (72) 887

25. M. G. ALBROW et al, PLB42 (73) 279, B44 (73) 207

26. E. L. BERGER, Proc. of 1973 Int. School of Subnuclear Phys. (Ed. A. ZICHICHI, Academic Press, (75))

27. J. WHITMORE et al, PL60B (76) 211

28. K. GUETTLER et al, 1976 TABILIZI (USSR) CONF
    B. ALPER et al, NPB100 (75) 237

29. C. HANG-MO et al, PL40B (72) 406
    L. K. LIKHODED et al, IHEP Preprint 74-51 (74)

30. B. ALPER et al, in 28

31. F. W. BUSSER et al, PL46B (73) 471

32. J. W. CRONION et al, PRL 31(73) 1426
    D. C. CAREY et al, PRL 32 (74) 24

33. J. W. CRONION et al, Chicago EFI preprint 74-1181 and 74-1182 (74)

34. P. V. LANDSHOFF, 1974 CERN Summer School

35. A. D. MARTIN, T. D. SPEARMAN, Elementary Particle Theory (North Holland, Amsterdam (1970))

36. S. HUMBLE, Int. to Particle Production in Hadron Phys. (Academic Press, London, (1974))

37. K. WILSON, AP, Austriaca 17 (63) 37
    A. KRZYWICKI, NOB58 (73) 633

38. J. BENECKE et al, PR188 (69) 2159

39. R. P. FEYNMAN, PRL 23 (69) 1415

40. R. G. ROBERT in 20

41. A. TOUNSI in 20

42. H. HARAI, PRL20 (68) 1305
    P.G.O. FREUND, PRL20 (68) 235

43. See e.g.: M.L. PERL, High Energy Hadron Phys. (John Willey and Sons, N.Y. 74)

44. E. RUTHERFORD, Phil. Mage 21 (1911) 669

45. R. E. TAYLOR, 1969 LIVERPOOL CONF.

46. J. D. BJORKEN, PRL16 (66) 408

47. G. MILLER, ARNS22 (73) 203

48. R. E. TAYLOR, 1975 SLAC Conf.

49. E. D. BLOOM et al, PRD4 (71) 2901

50. F. W. BRASSE et al, NPB 39 (72) 421

51. V. I. ZAKHAROV, 1976 TABILISI (USSR) CONF.

52. E. D. BLOOM in 57

53. R. P. FEYNMAN in 39 and Photon Hadron Int. (BENJAMIN Inc.)

54. C. CALLAN et al, PRL 22 (69) 156

55. C. H. LLEWELLYN SMITH, PR5C (72) 261

56. J. D. BJORKEN, PR179 (69) 1547

57. J. KUTI et al, PRD4 (71) 3418
    P. V. LANDSHOFF et al, NPB28 (71) 240

58. D. H. PERKINS, 1972 BATAVIA Conf.

59. D. H. PERKINS, CONTEMP. P16 (75) 173

60. P. MUSSET, 1973 AIX Conf.
    D. H. PERKINS in 48

61. F. E. CLOSE, 1976 SUSSP

62. D. H. PERKINS in 34

63. S. D. DRELL et al, PRL25 (70) 316

64. F. H. HALZEN et al, PRL40 (78) 1117

65. S. D. ELLIS et al, RMP49 (77) 753

66. S. J. BRODSKY et al, PRL31 (73) 1153 and PRD11 (75)1304
    V. A. MATVEEV et al, NCL7 (73) 719

67. R. BLANKENBECLER et al, PL39B (72) 649

68. B. SCHREMPT et al, PL55B (75) 303

69. S. M. BERMAN et al, PRD4 (71) 3388

70. R. D. FIELD et al, PRD15 (77) 2590

71. D. SIVERS et al, PR23C (76) 1

72. P. V. LANDSHOFF et al, PRD10 (74) 891

73. D. ANTEASYAN et al, PRL38 (77) 112 and 115

74. R. MOLLER, 1976 TUTZING (W. GERMANY) Coll.

75. G. C. FOX, 1976 BROOK HAVEN APS meeting

76. P. DARRIULAT et al, NPB107 (76) 429

77. M. DELLA NEGRA in 74

78. K. EGGART et al, NPB98 (75) 73

79. P. DARRIULAT et al, 1976 TBILISI Conf.

80. B. ALPER et al (DILR Collaboration) Preprint PR-76-031(76)

81. M. DELLA NEGRA et al, Preprint CERN/EP/Phys. 76-35

82. R. P. FEYNMAN et al, NPB128 (77) 1

83. J. F. GUNION, SLAC-PUB-1938-1977

84. A. G. CLARK et al, PL74B (78) 267

85. M. K. CHASE et al, NPB133 (78) 157

86. A. V. BARNES et al, PRL40 (78) 917

87. R. MOLLER, 1977 RENCONTRE de MORIOND, FLINE, FRANCE

88. M. JACOB et al, NPB113 (76) 395

89. C. BROMBERG et al, CALT-68-590
                        UCLA-1089

90. R. D. FIELD et al, CALT-68-593

91. G. DONALDSON et al PRL40 (78) 917

92. R. D. FIELD et al, CALT-68-633

93. R. CULTER PRD17 (78) 196

## Table I: Compilation of parameters fitted to Eqs. (III.1)-(III.2) - Taken from Ref.65

| Reaction | $N$ | $\hat{M}^2$ | $F$ |
|---|---|---|---|
| $pp \to \pi^+$ | 8.60 ± 0.04 | | |
| | 7.70 ± 0.12 | 0.74 ± 0.02 | 11.0 ± 0.7 |
| | 8.2 ± 0.5 | | 9.0 ± 0.5 |
| $pp \to \pi^-$ | 8.60 ± 0.04 | | |
| | 7.78 ± 0.14 | 0.79 ± 0.0? | 11.9 ± 0.7 |
| | 8.5 ± 0.5 | | 9.9 ± 0.5 |
| $pp \to \pi^0$ | 8.60 ± 0.04 | | |
| | 7.2 ± 0.2 | | |
| | 10.8 ± 0.4 | 2.3 ± 0.3 | 7.1 ± 0.4 |
| $pp \to K^+$ | 8.72 ± 0.30 | 1.69 ± 0.05 | 9.0 ± 1.0 |
| | 5.4 | | 8.8 |
| $pp \to K^-$ | 8.76 ± 0.36 | 1.77 ± 0.10 | 12.2 ± 1.1 |
| | 8.9 | | 11.7 |
| $pp \to p$ | 10.33 ± 0.34 | 1.82 ± 0.07 | 7.3 ± 0.9 |
| | 11.7 | | 6.8 |
| $pp \to \bar{p}$ | 9.1 ± 0.3 | 1.17 ± 0.06 | 14.0 ± 1.4 |
| | 11.9 | | 8.0 |
| $\pi^- p \to \pi^0$ | 10.0 ± 0.2 | 1.8 ± 0.2 | 5.5 ± 0.3 |
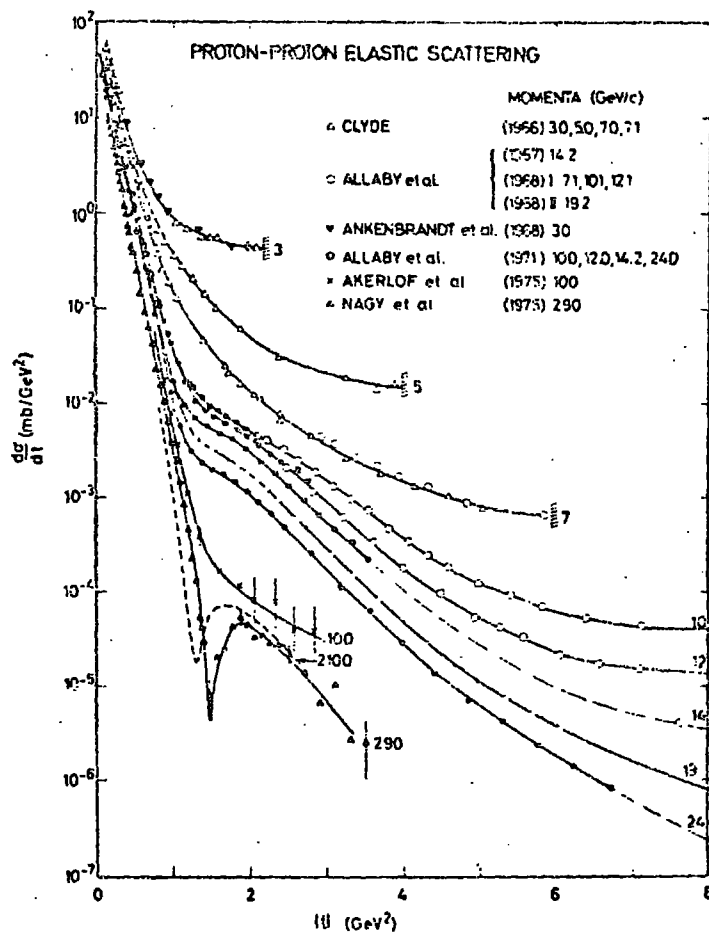
Fig. 1: Large angle elastic
pp scattering.
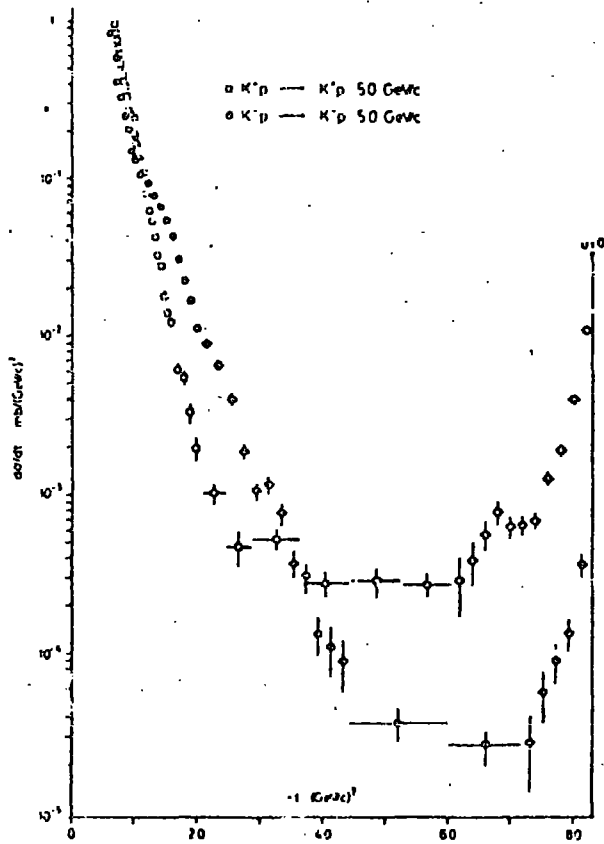
Fig. 2: $K^+p$ and $K^-p$ elastic
differential cross sections
over the entire momentum trans-
fer range at 5 GeV/c·
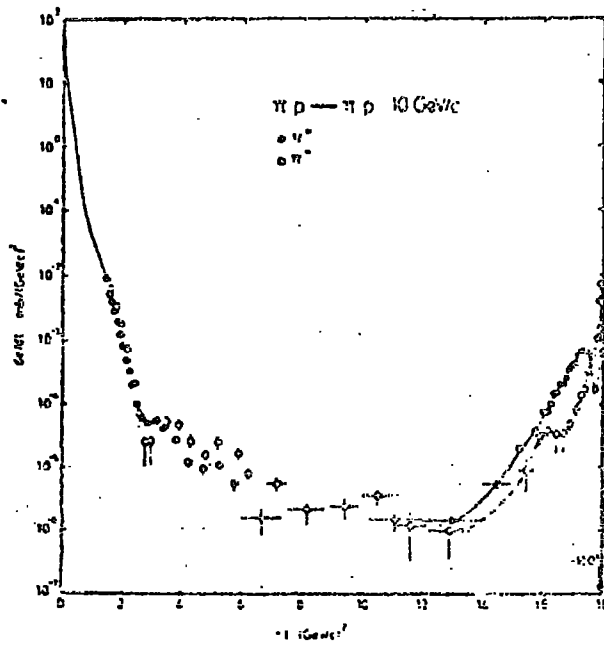
Fig. 3: The full angular distribution of
$\pi^{\pm}$p elastic scattering at 10 GeV
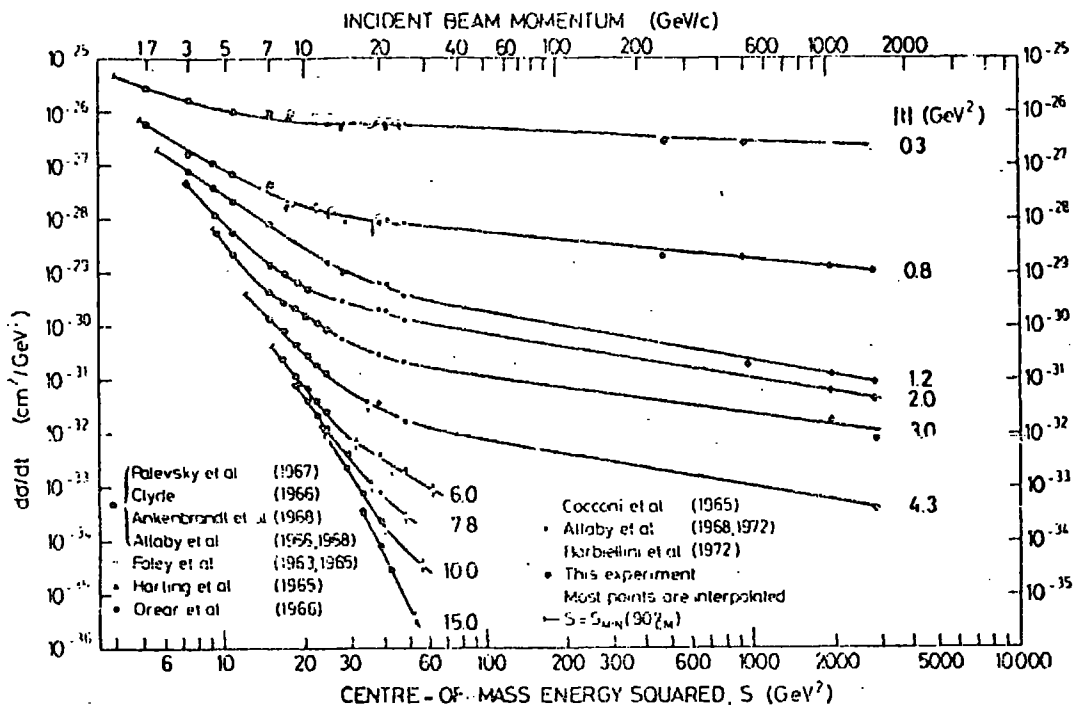
Fig. 4: Energy dependence of the pp elastic
cross sections for various fixed values of t.
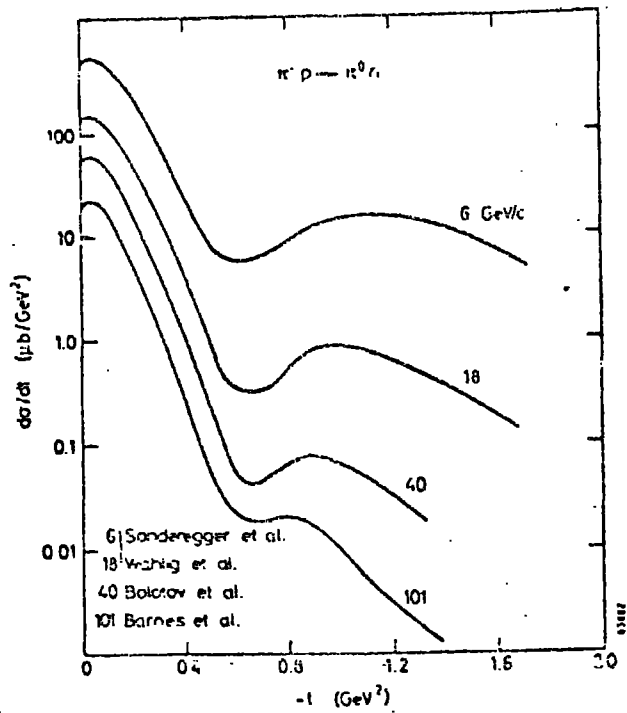
Fig. 5a: Schematic drawing of the energy dependence of $\pi^- p$ charge exchange scattering.
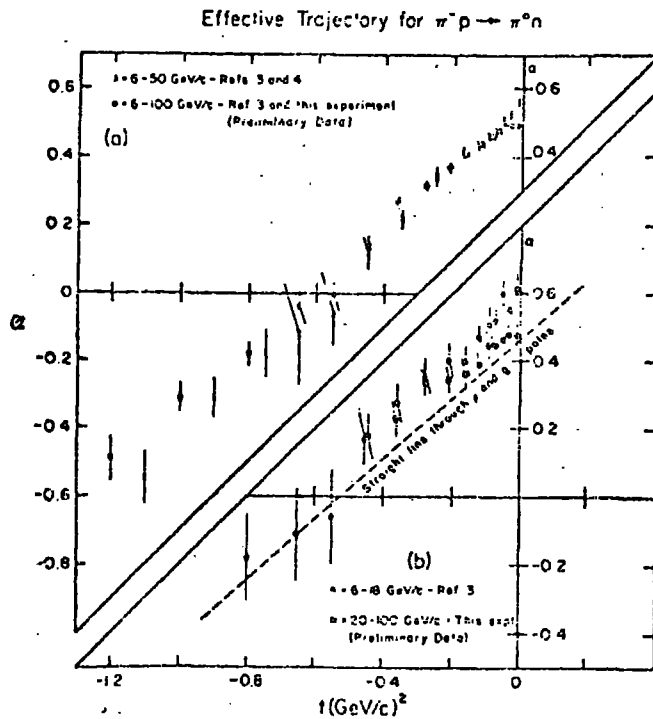


Fig. 5b: The effective trajectory derived from $\pi^- p \longrightarrow \pi^0 n$ .
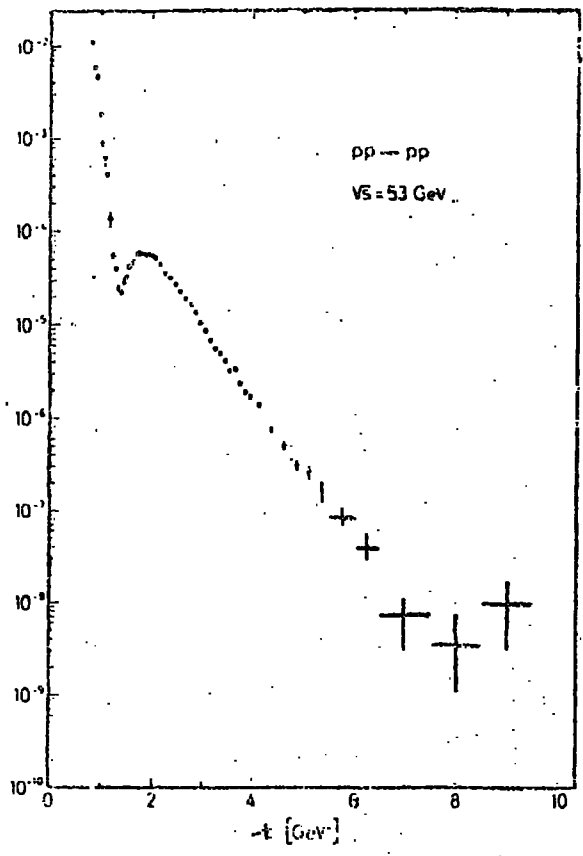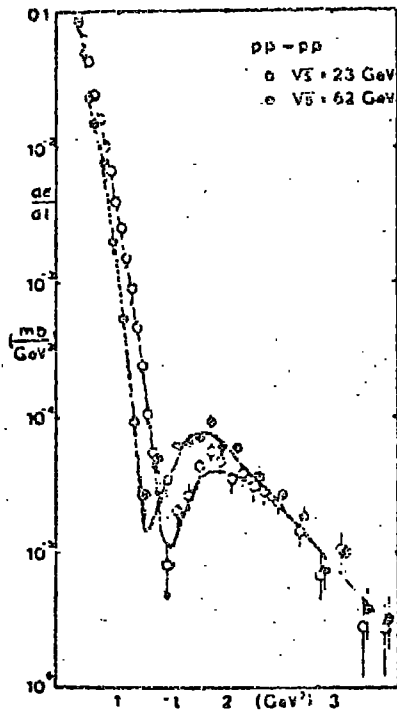
Fig. 6: Differential cross sections (a) for
momentum transfer -t > 0.6 GeV$^2$ (the solid
lines represent eq. (I.9)), (b) as a function of t.
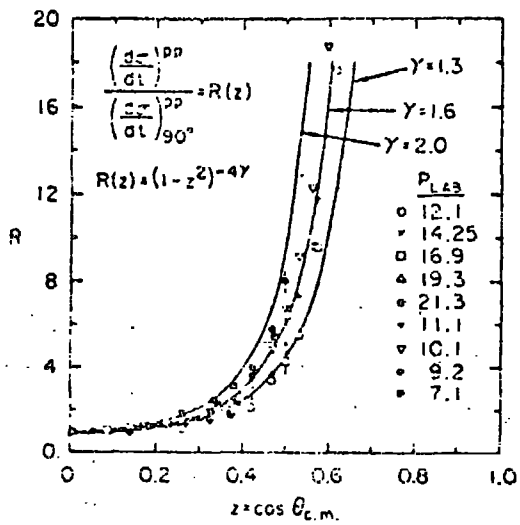
Fig. 7: The angular distribution
of pp scattering normalized to the
90° value at various values of the
incident momentum. The curves show
possible fits to the angular dis-
tribution.
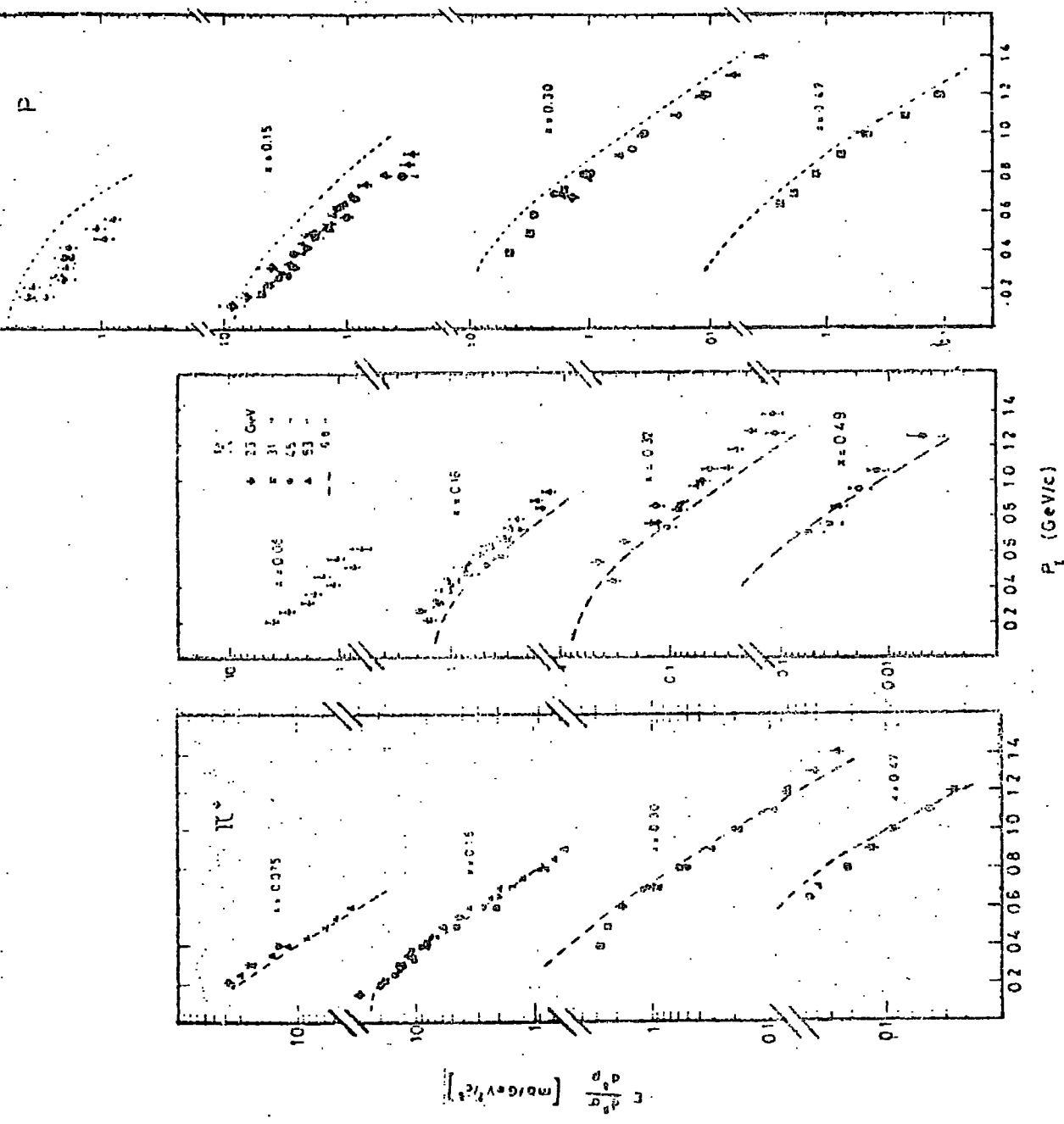
Fig. 8: The invariant cross sections for the inclusive production of $\pi^+$, $K^+$ and $p$ plotted versus $P_\perp$ at fixed values of $x$.
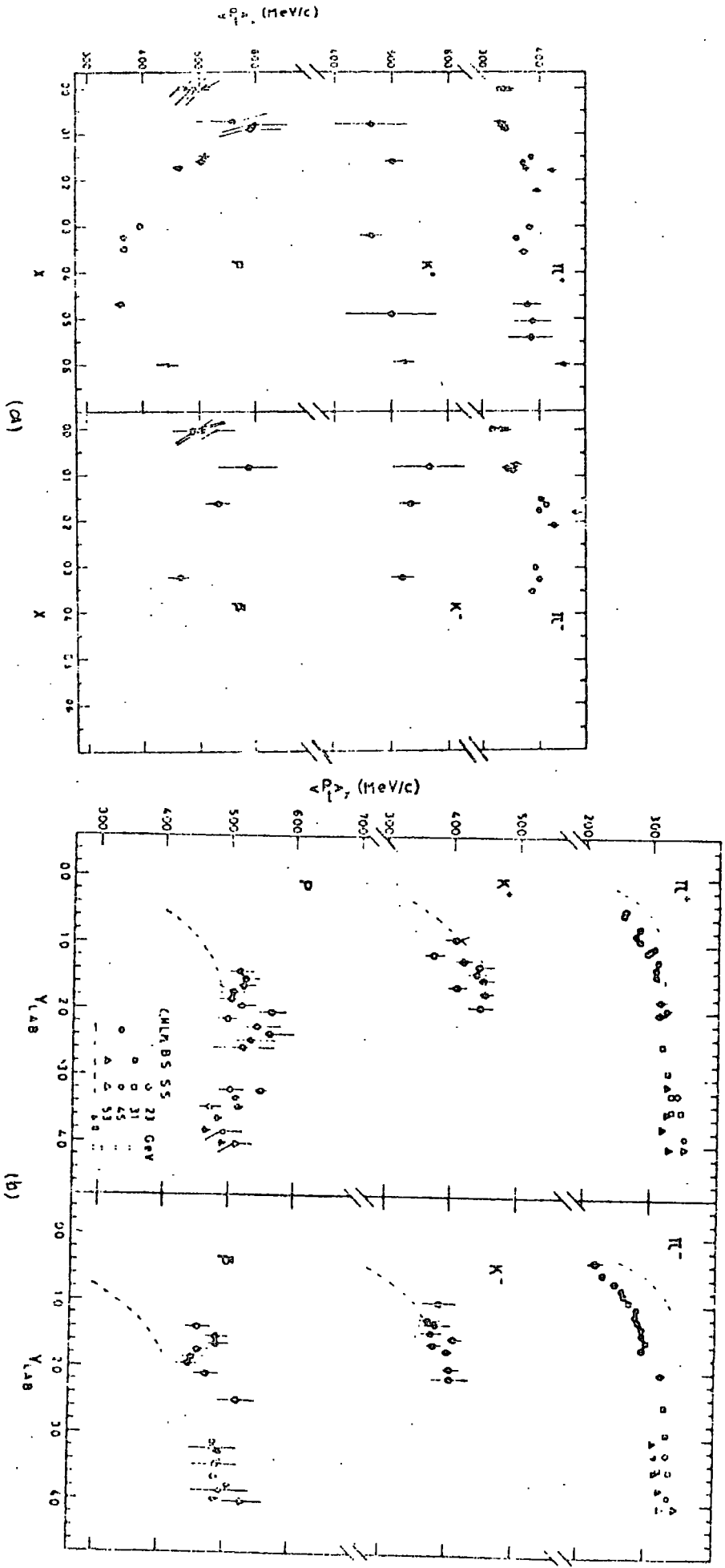
Fig. 9: The compilation of the average values of the transverse momentum for $\pi^+$, $\pi^-$, $K^+$, $K^-$, $p$, and $\bar{p}$, computed at fixed values of (a) the x-variable, $\langle P_\perp \rangle_x$, versus x, (b) the ylab-variable, $\langle P_\perp \rangle_{y_{lab}}$, versus $y_{lab}$.
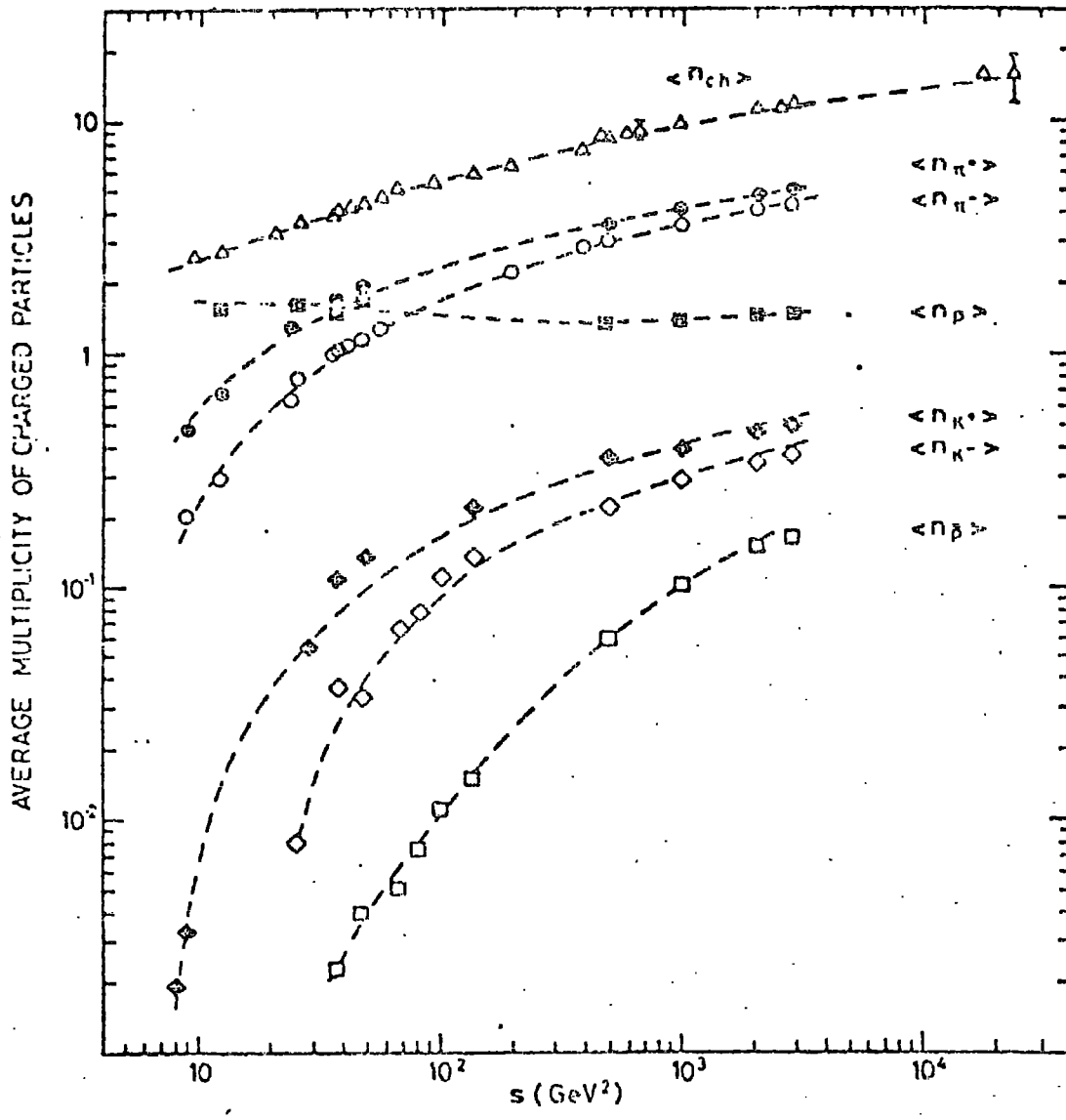
Fig. 10: The average multiplicity
of $\pi^+$, $\pi^-$, $K^-$, $K^+$, $\bar{p}$, p, and $<n_{ch}>$
as a function of s. The dashed lines
represent the results of the fits
according to Eqs. (J.13) and (J.14)
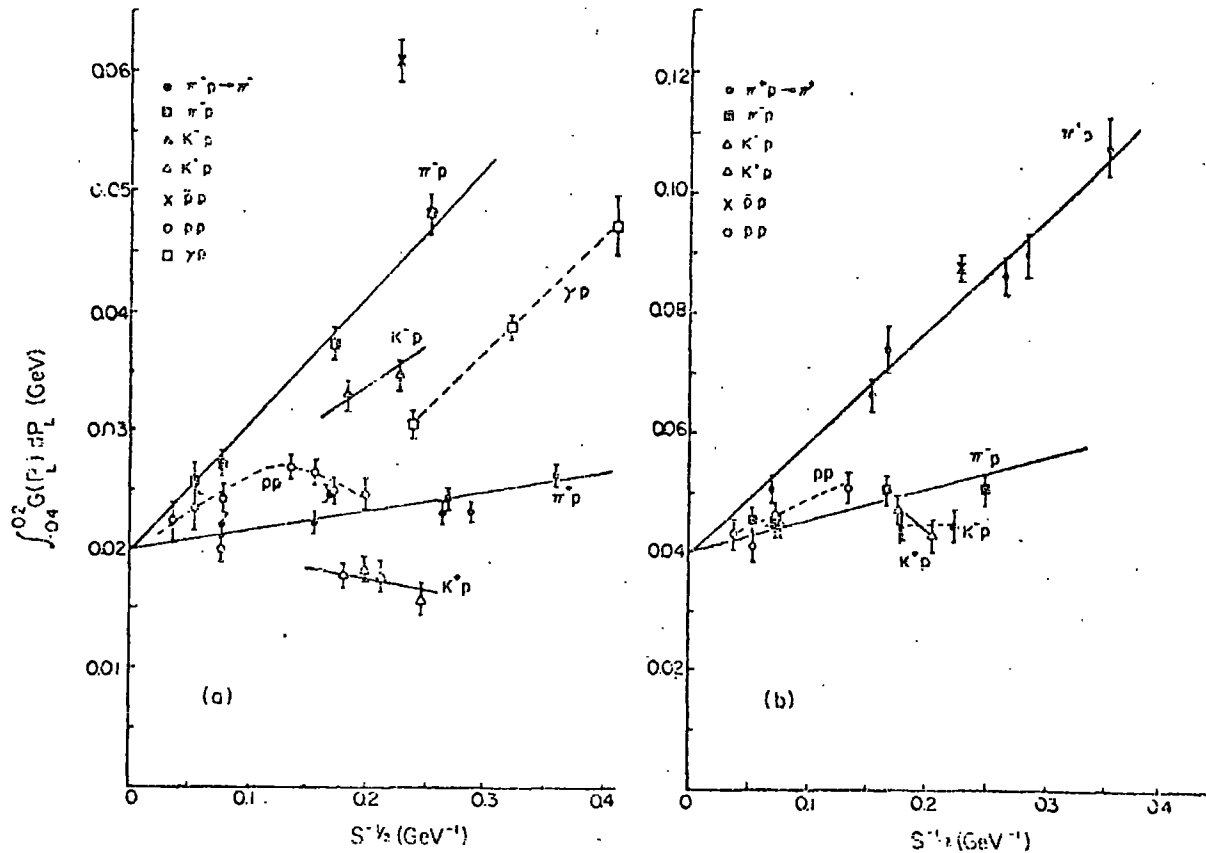
Fig. 11: The invariant cross section for inclusive $\pi$ production, evaluated in the laboratory system and integrated over all $P_\perp^2$ and over $-0.4 < P_L < 0.2$ GeV/c, versus $s^{-\frac{1}{2}}$. The lines are hand-drawn to guide the eye through the data. (a) $\pi^-$ and (b) $\pi^+$ production.
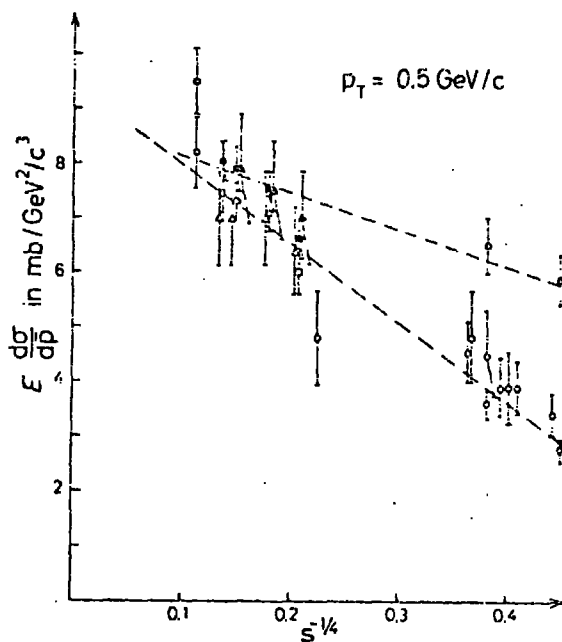
Fig. 12: The invariant cross section for
production of $\pi^{\pm}$ at $\theta^{c.m.} = 90^{\circ}$ and $p_T = 0.5$ GeV/c, as a function of $s^{-\frac{1}{4}}$. Open
symbols denote $\pi^-$, black symbols $\pi^+$.
The circles, triangles, and squares rep-
resent measurements by bubble chambers,
the Saclay-Strasbourg Collaboration, and
this experiment, respectively. The dashed
lines are fits to the data points.
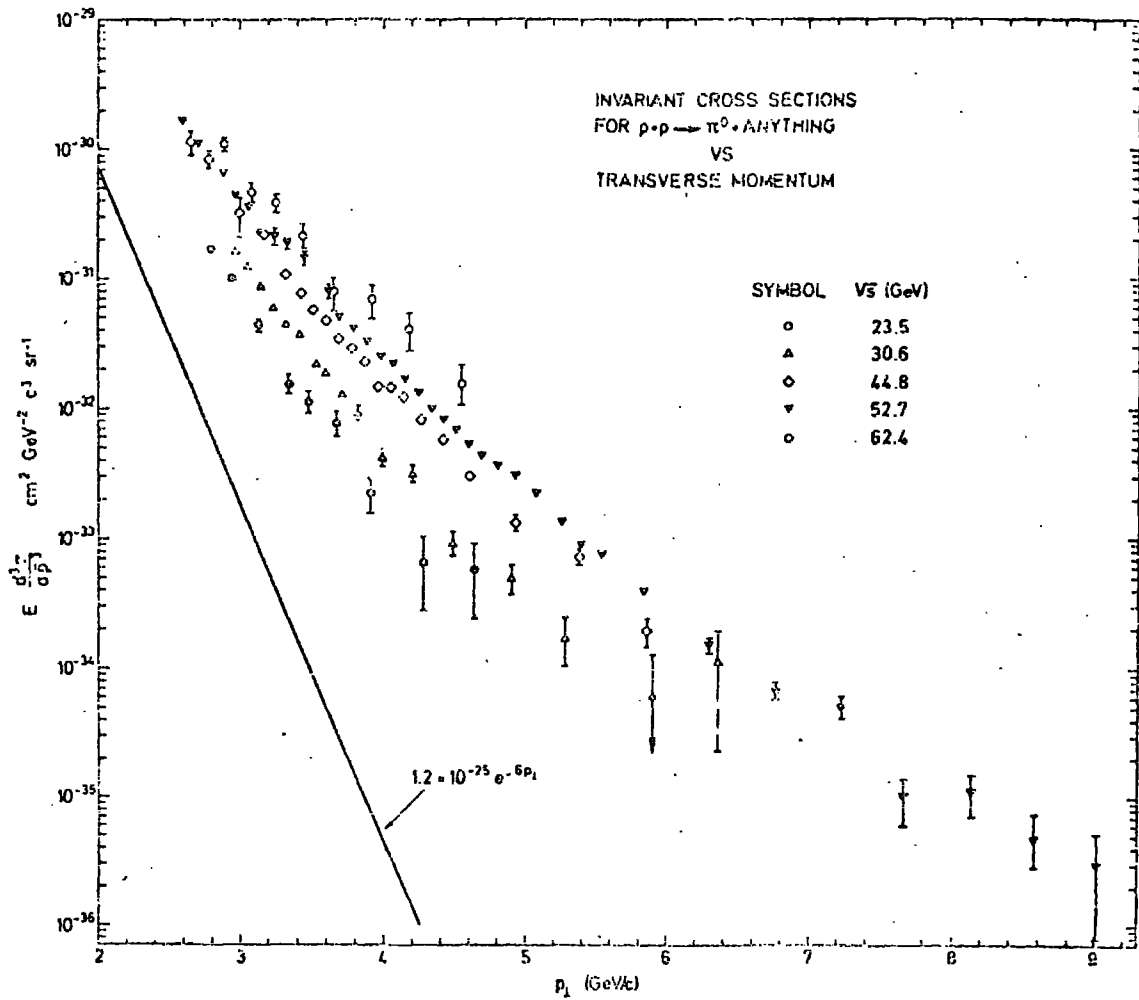
Fig. 13: The transverse momentum
dependence of invariant cross-
sections of five centre-of-mass
energies. The errors are statistical
only.
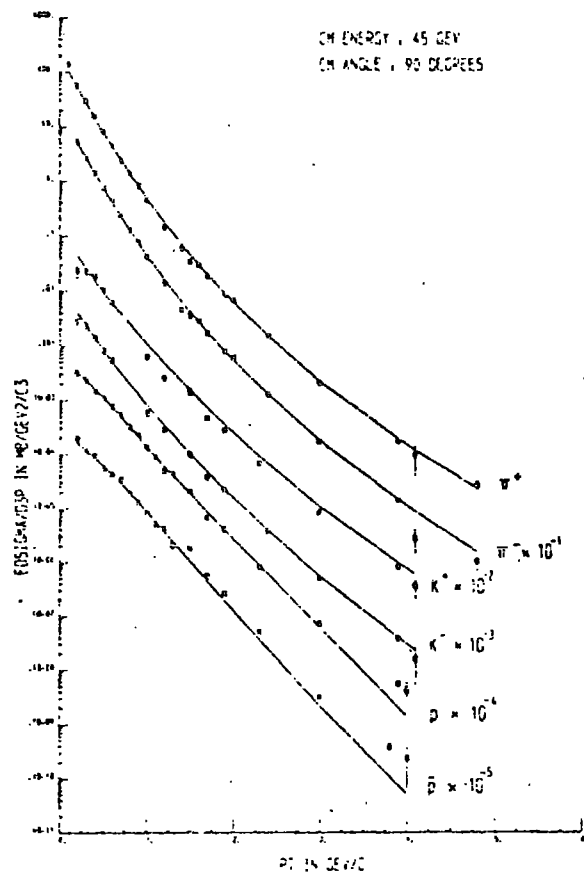
Fig. 14: The invariant differential
cross section for production of $\pi^\pm$,
$K^\pm$, and $p^\pm$, at $\theta^{c.m.} = 90°$ and $\sqrt{s} = 45$ GeV.

PRINCETON - CHICAGO

p + W → π + ANYTHING

- 400 GeV
- 300 GeV
- 200 GeV

$E \, d\sigma/d^3p \ (cm^2 \ GeV^{-2})$

$10^{-26}$
$10^{-27}$
$10^{-28}$
$10^{-29}$
$10^{-30}$
$10^{-31}$
$10^{-32}$
$10^{-33}$
$10^{-34}$
$10^{-35}$
$10^{-36}$
$10^{-37}$
$10^{-38}$
$10^{-39}$

200 GeV →

400 GeV

EXTRAPOLATION
FROM SMALL
$P_\perp$ DATA

$P_\perp$ (GeV/c)
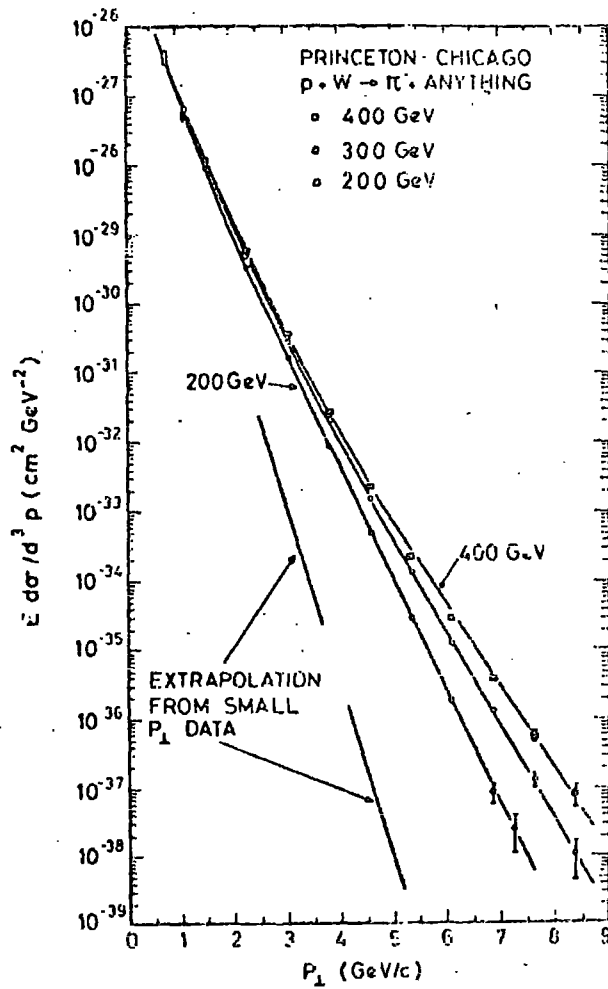
Fig. 15 : Exhibition of π
production versus $P_\perp$ at
different fixed energies
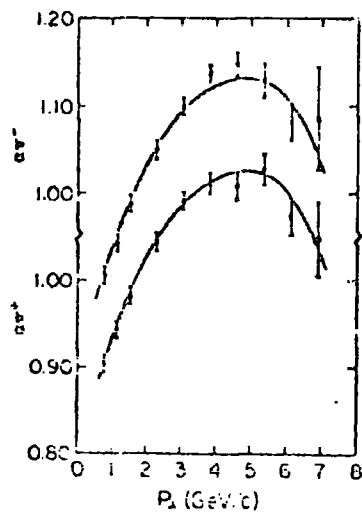
Fig. 16:  The power $\alpha$ in the atomic
number dependence vs $P_T$ for $\pi^+$ and
$\pi^-$.  The lines are drawn to guide
the eye.

A SCALING OF THE INCLUSIVE $\pi^0$ CROSS SECTION
AT LARGE TRANSVERSE MOMENTA

| SYMBOL | $\sqrt{s}$ (GeV) |
|--------|-----------|
| ⊖ | 23.5 |
| △ | 30.6 |
| □ | 44.8 |
| ▽ | 52.7 |
| ○ | 62.4 |
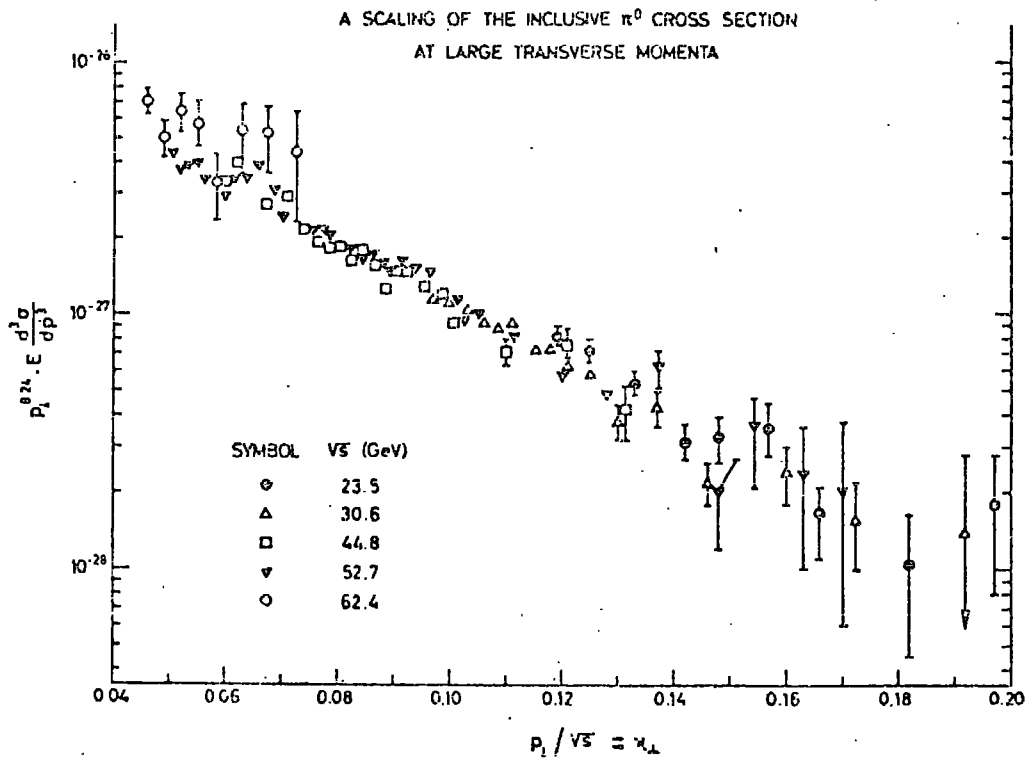
Fig. 17: The function $F(P_\perp/\sqrt{s}) = P_\perp^n E(d^3\sigma/dP^3)$,

$n = 8.24$.
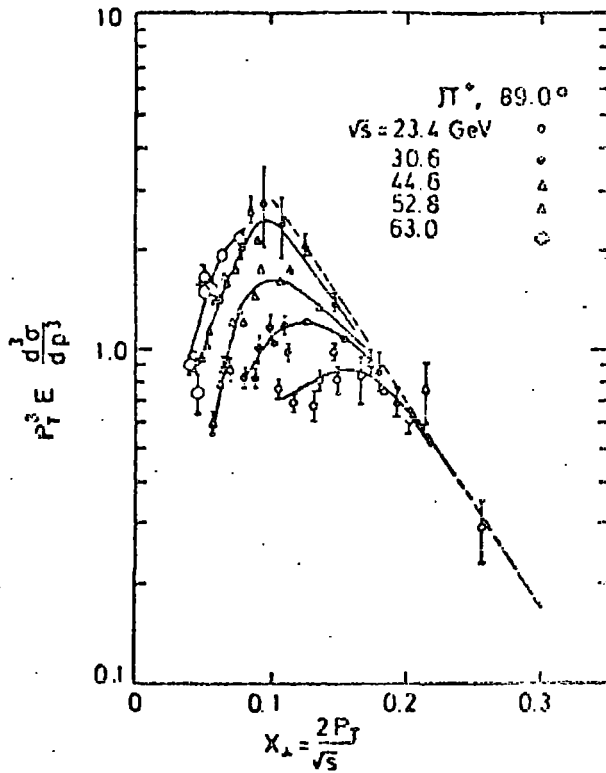
Fig. 18: $\pi^{+}$ data at $\Theta_{c.m.} = 89^{\circ}$ for five different energies of the ISR, illustrating the possible approach to a scaling limit at high $p_T$ satisfying the function

$$E\frac{d^3\sigma}{dp^3} = p_{\perp}^{-8} f(p_{\perp}/\sqrt{s})$$

The straight line is a fit to $\pi^{0}$ data renormalized by a factor of 0.7.
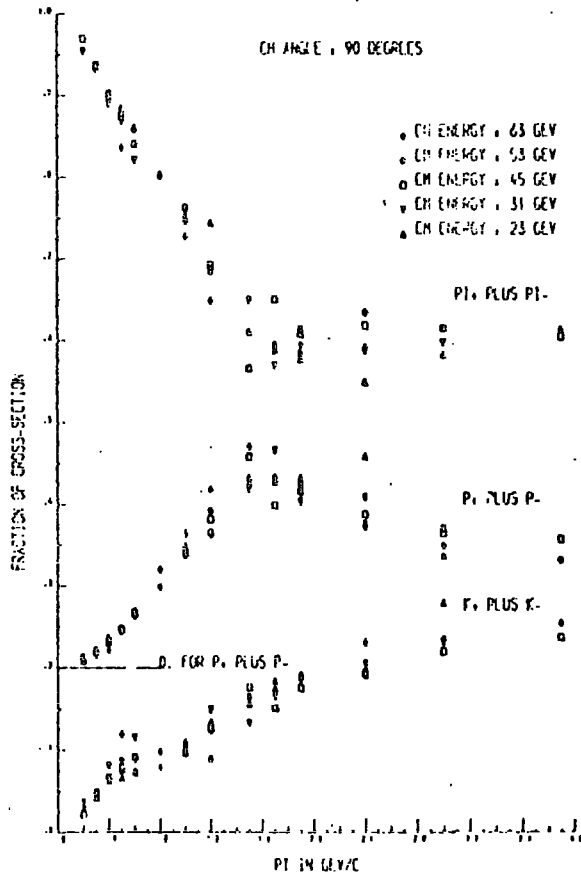
Fig. 19: At $\Theta^{C.m.} = 90^{\circ}$, the fraction of the charged production cross section going into pions, kaons and protons (summed over both signs), as a function of $P_\perp$. The cross sections used is $d\sigma/dp\,d\Omega$. The proton plus antiproton fraction is shifted upwards by 0.2 units in order to avoid confusion with the kaon fractions.

CM ANGLE: 90°
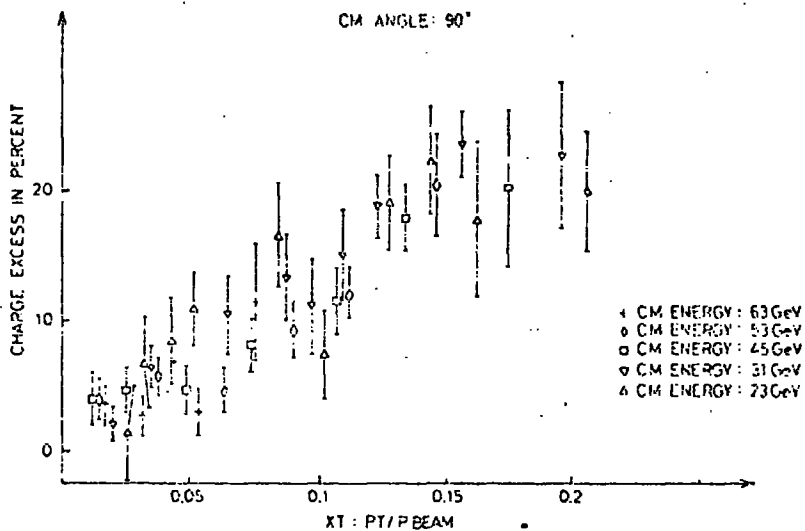
Fig. 20: The charge excess in percent as a
function of $x_\perp = 2 P_\perp / \sqrt{s}$ at $\Theta^{cm} = 90°$. The
charge excess was computed as the sum of the
cross sections for production of $\pi^+$, $K^+$,
and protons, minus the sum of the cross sections
for production of $\pi^-$, $K^-$, and antiprotons,
divided by the sum of the cross sections for
production of all these charged particles. The
cross section used is $d\sigma / dp \, d\Omega$.
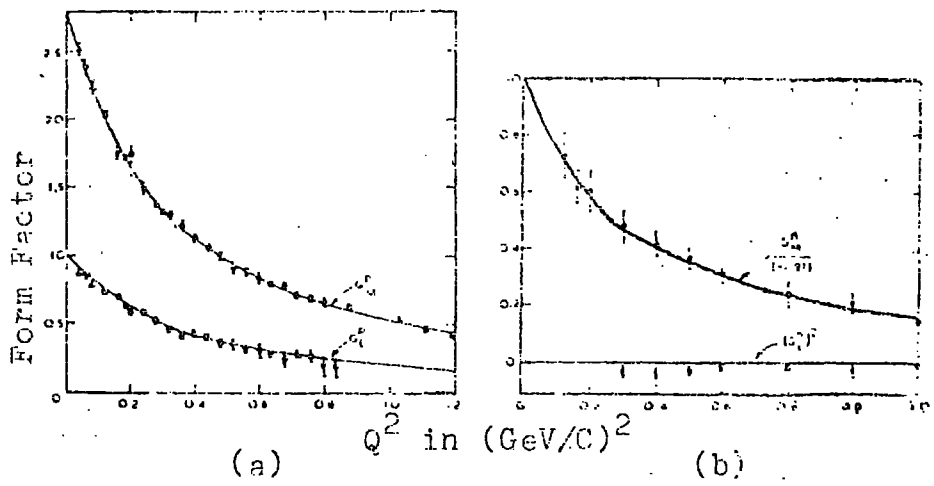
Fig.21: Form factor of
(a) proton, (b) Neutron
versus $Q^2$
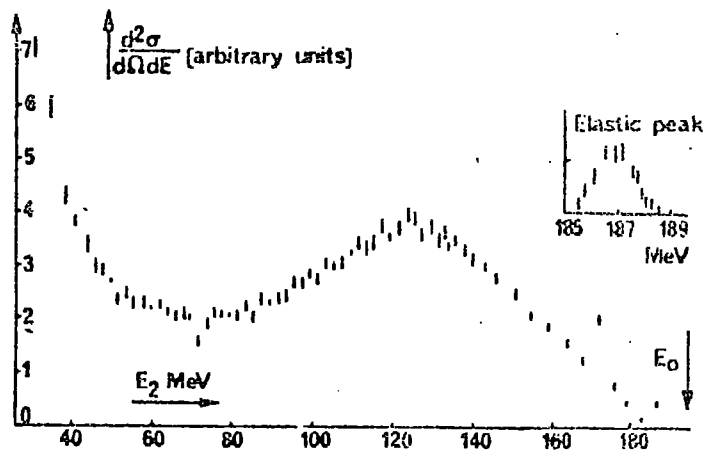
Fig. 22 :  Inelastic scattering of
194 MeV electrons at 135° from the C¹²
nucleus
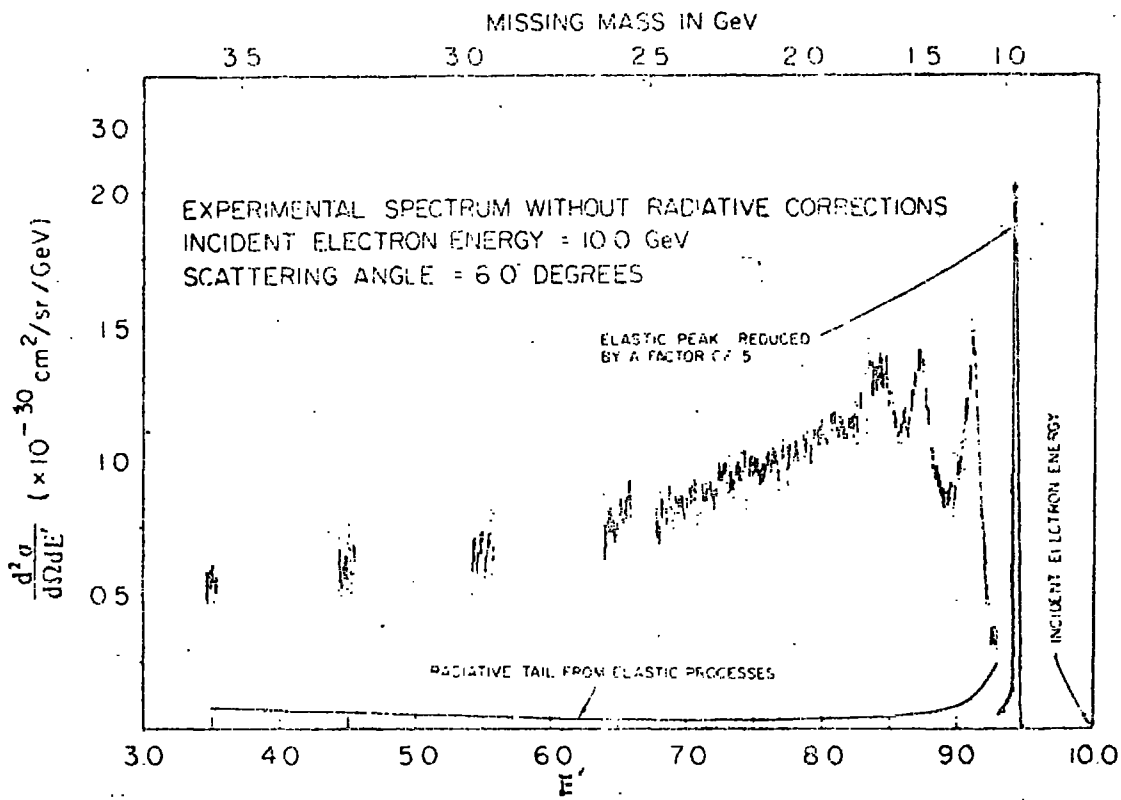
Fig. 23: A spectrum of scattered electrons
at 6° for 10 GeV electrons incident on
hydrogen. $d^2\sigma/d\Omega\,dE'$ is shown as a function
of scattered electron energy, E'.
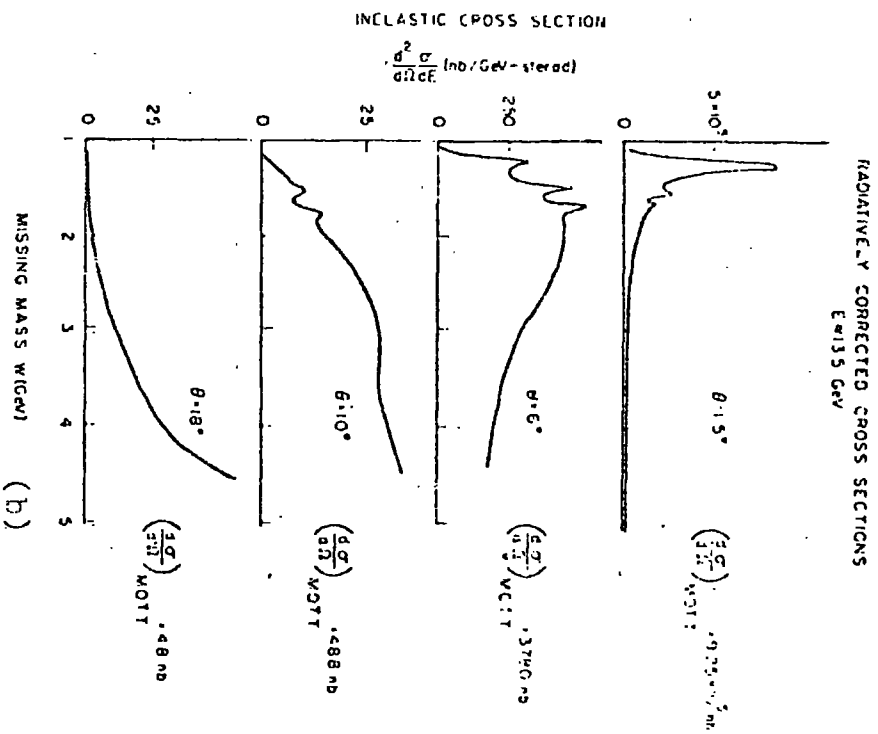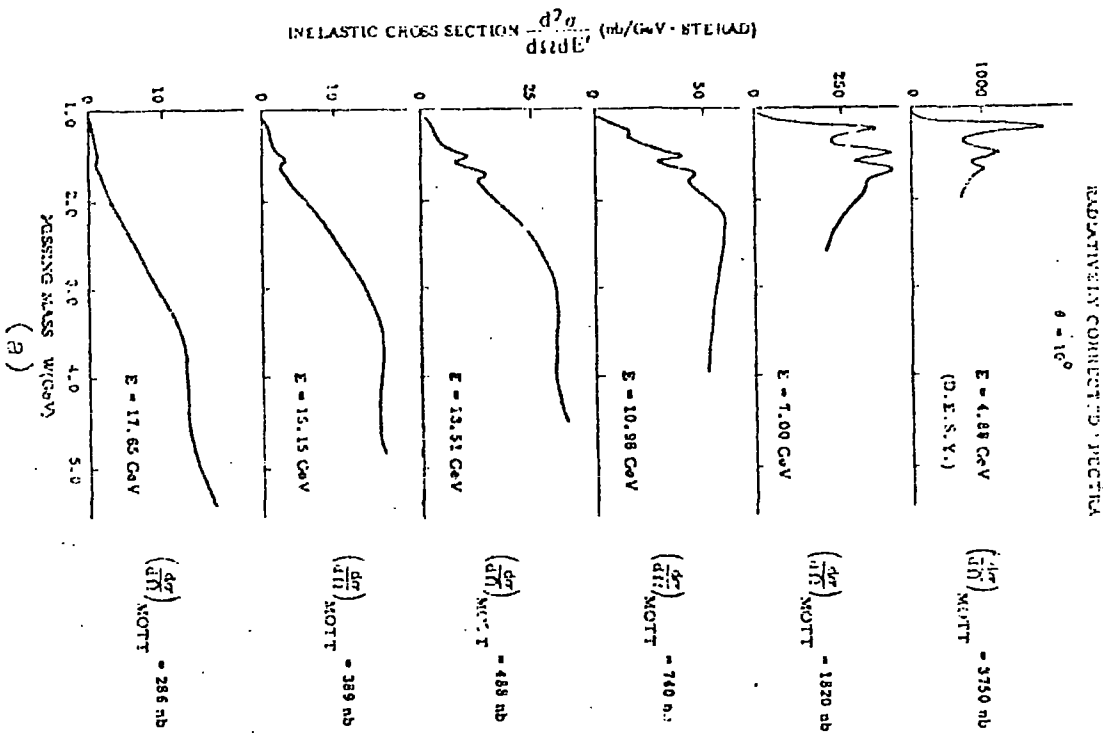
Fig. 24: Sketch of the behaviour of radiatively corrected ep cross sections for various (a) energies and (b) angles.
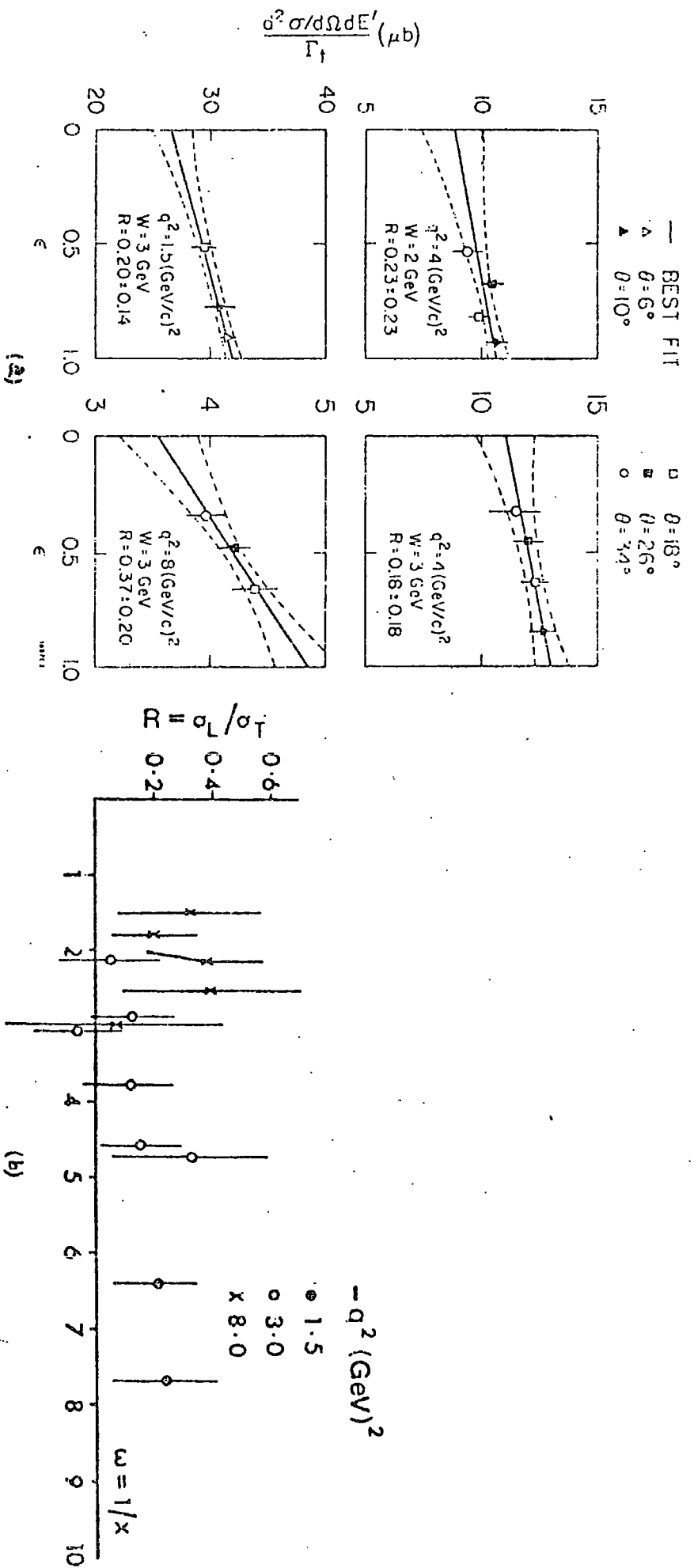
Fig. 25: (a) Separate determination of $\sigma_L$ and $\sigma_T$ (the dashed lines indicate the one standard deviation values of the fits). (b) the data on $R = \sigma_L/\sigma_T$.
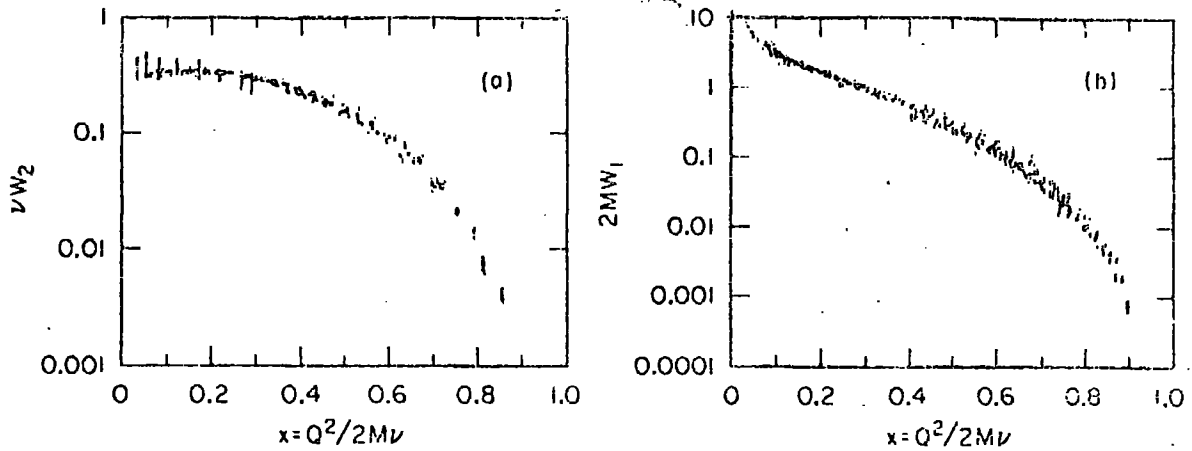
Fig. 26a: Values of $\nu W_2$ and $2MW_1$ for the proton with $Q^2 > 1$ GeV$^2$ and $W^2 > 4$ GeV$^2$. $R = \sigma_L/\sigma_\perp$ is assumed to be zero, and values of $\nu W_2$ are extracted from cross section measurements with $\varepsilon \geq 1/2$, while values of $2MW_1$ are extracted for $\varepsilon \leq 1/2$. The large vertical bars below $x = 0.3$ in the graph of $\nu W_2$ are obtained from muon data taken at Fermilab.
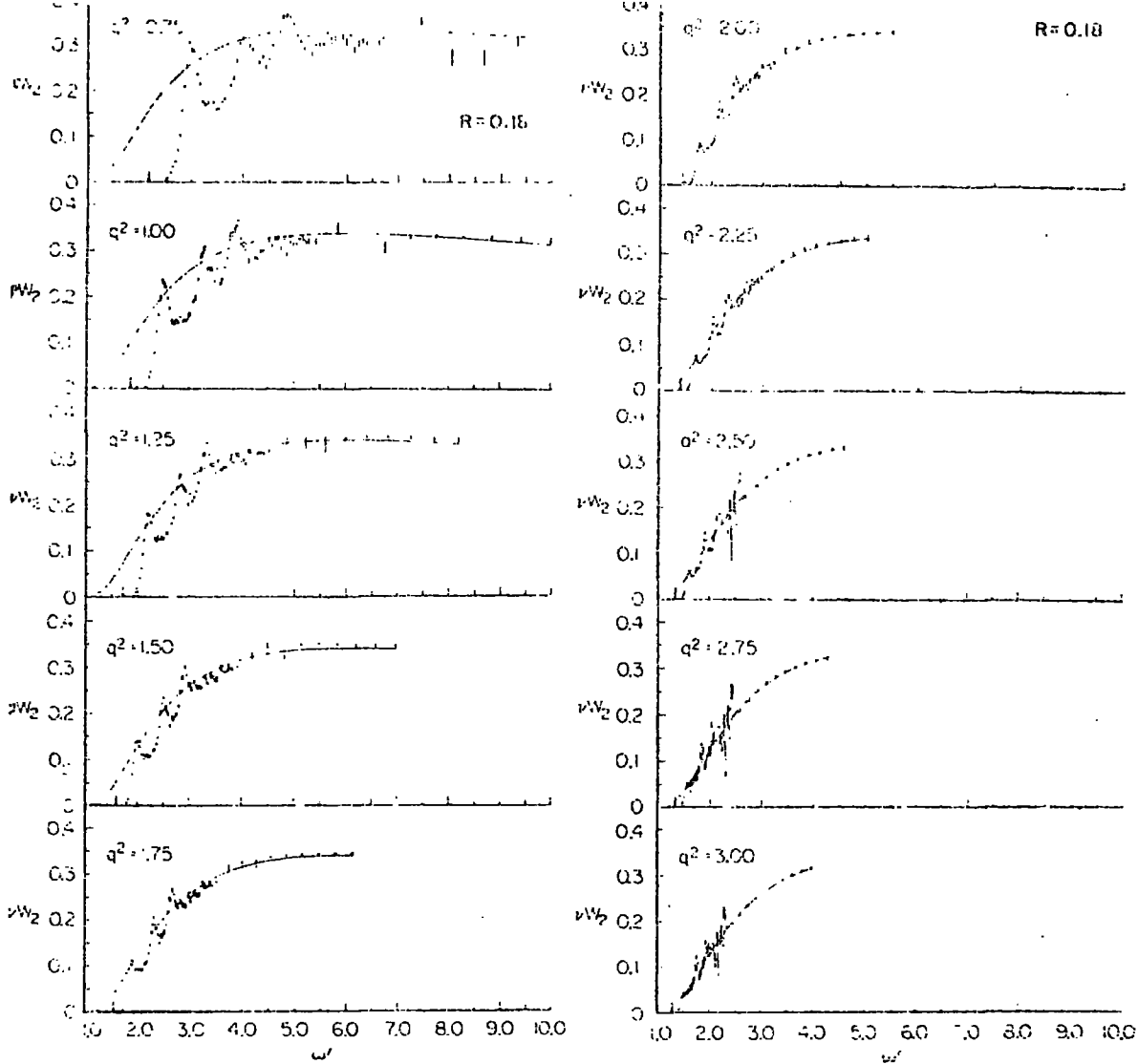
Fig. 26b: $\nu W_2(\nu, q^2)$ versus $\omega' = 1 + \dfrac{W^2}{q^2}$ (at fixed $q^2$). Fit to the data, the scaling limit curve $\nu W_2(\omega')$, is seen as solid line.
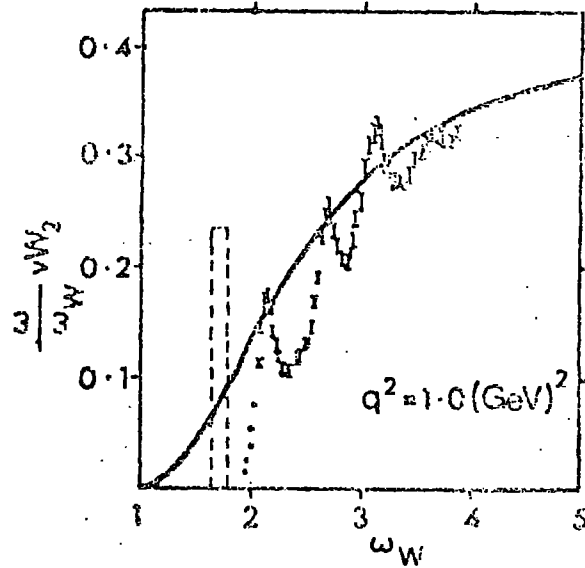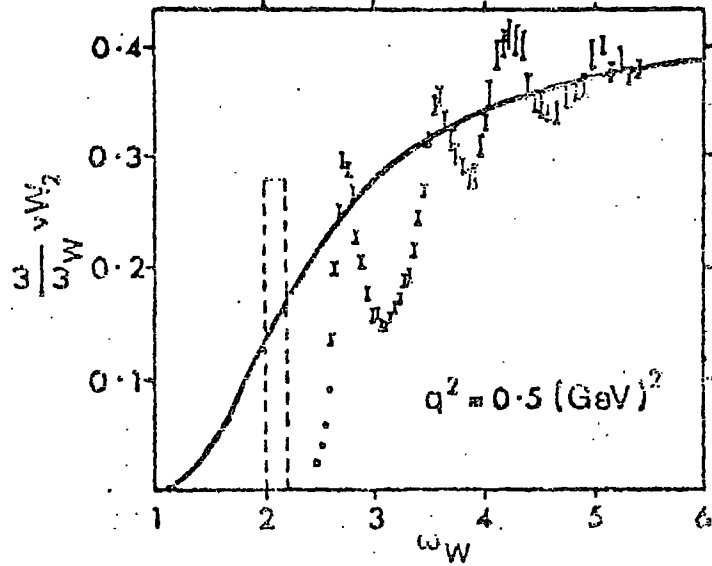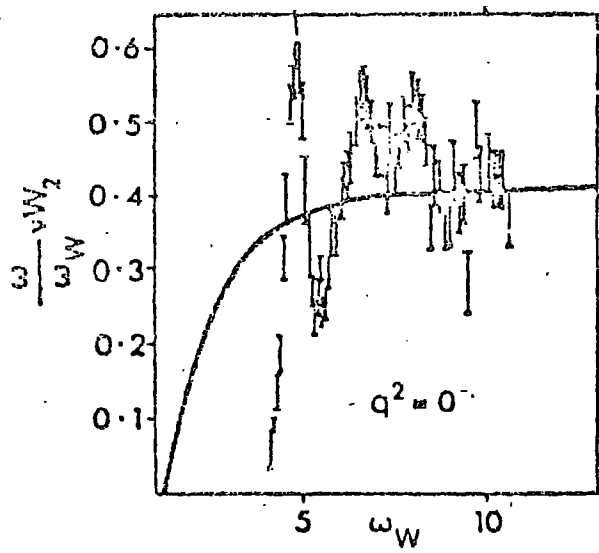
Fig. 26c: Comparison of $\omega_\nu W_2 / \omega_w$ in the resonance region with the scaling limit curve. The dashed rectangles represent the $\delta$-function contribution of elastic scattering.
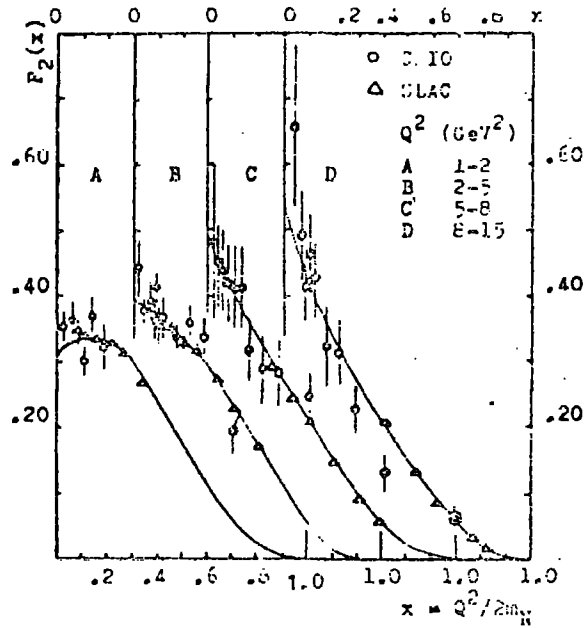
Fig. 26d: Proton structure
function $F_2(x)$ versus $Q^2$.
The x scales of the subsequent
graphs are shifted by 0.3. The
curves are the fits $F_2(x) = \sum_{i=1}^{5} a_i (1-x)^i$.
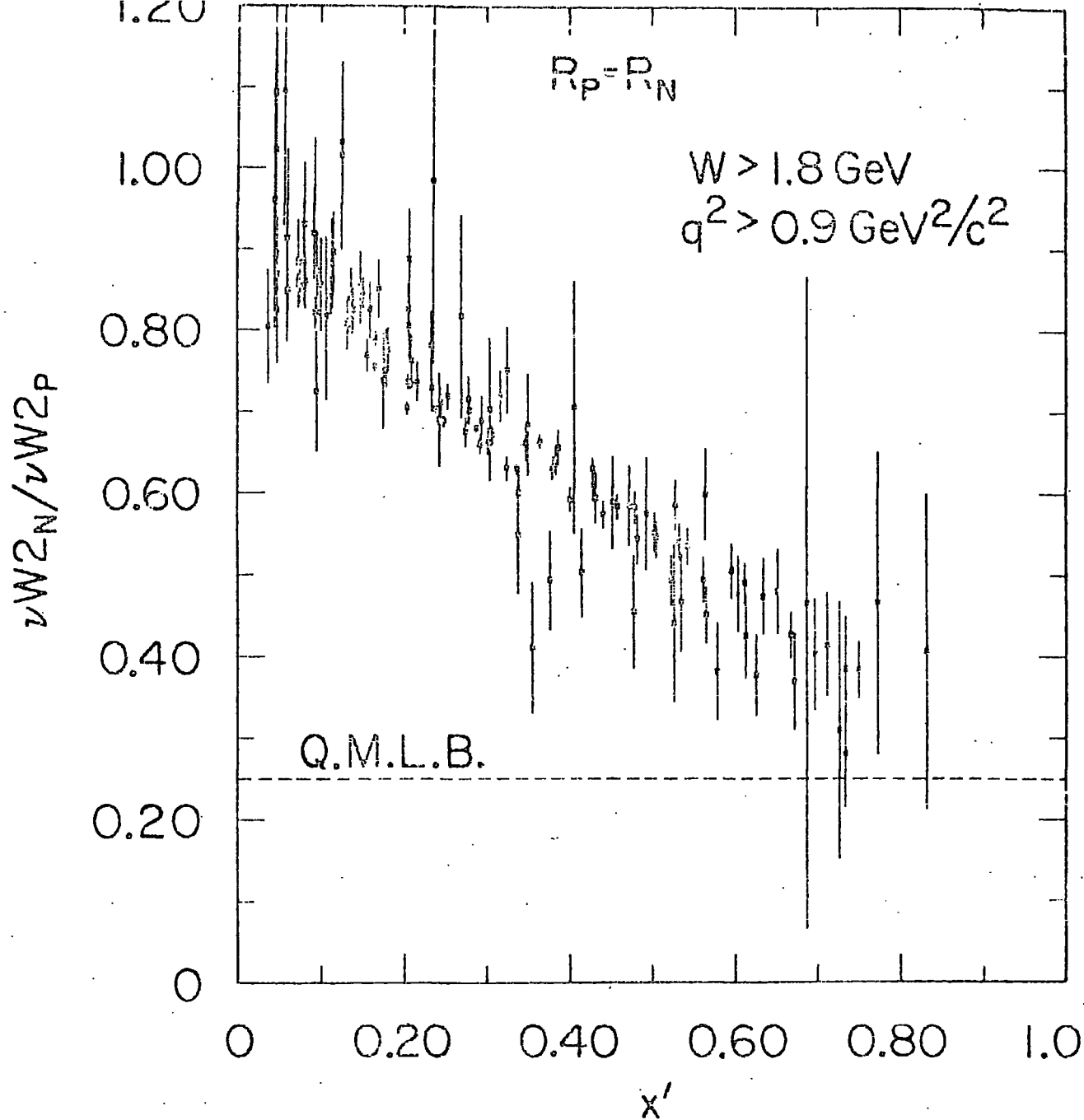
Fig. 27a: (n/P) for the combined data plotted versus x' , $R_p = R_n$ is assumed.
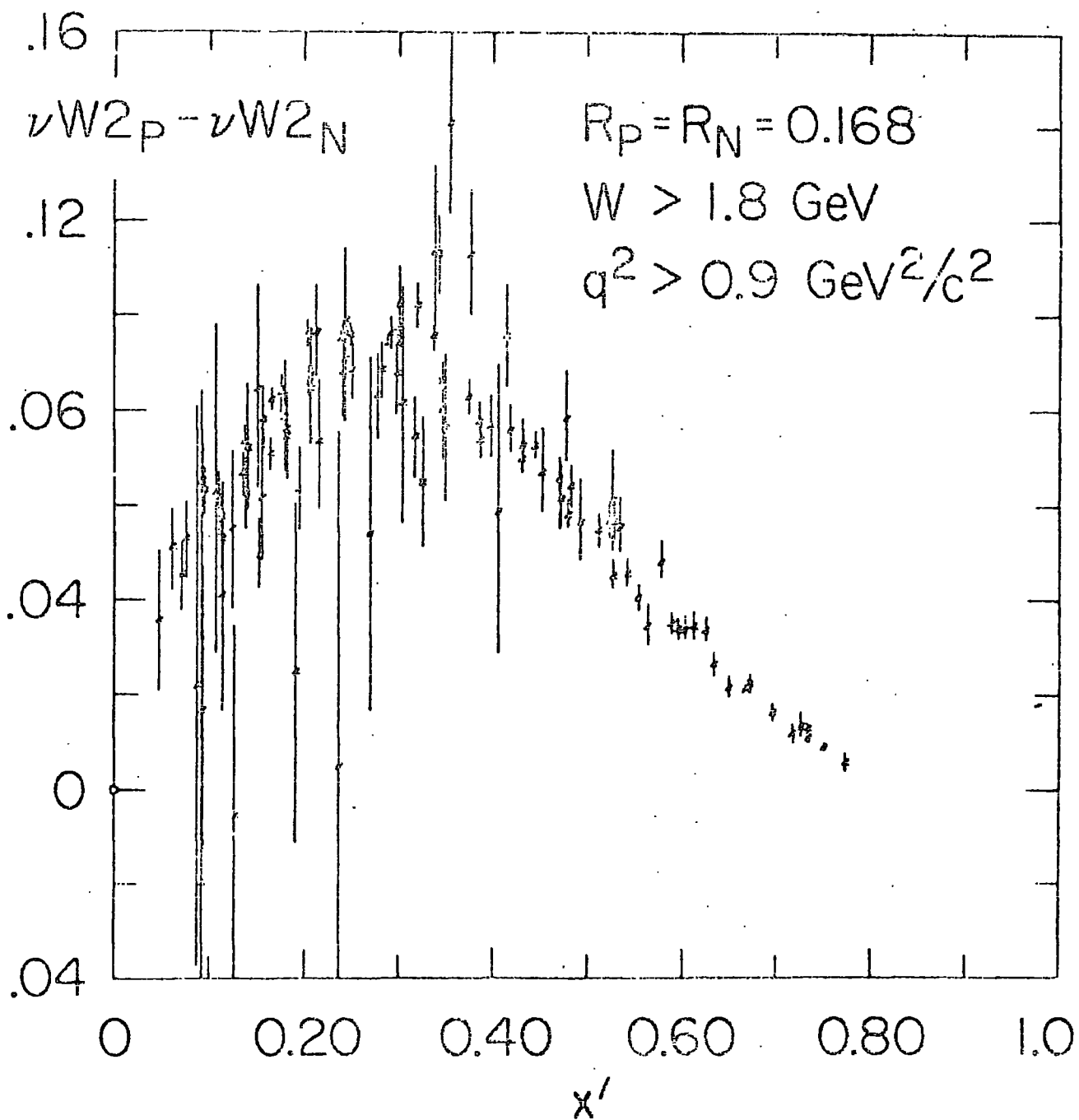
Fig. 27b: $\nu W_2^p - \nu W_2^n$ versus x' under the
assumption that $R_p = R_n \leqslant 0.168$
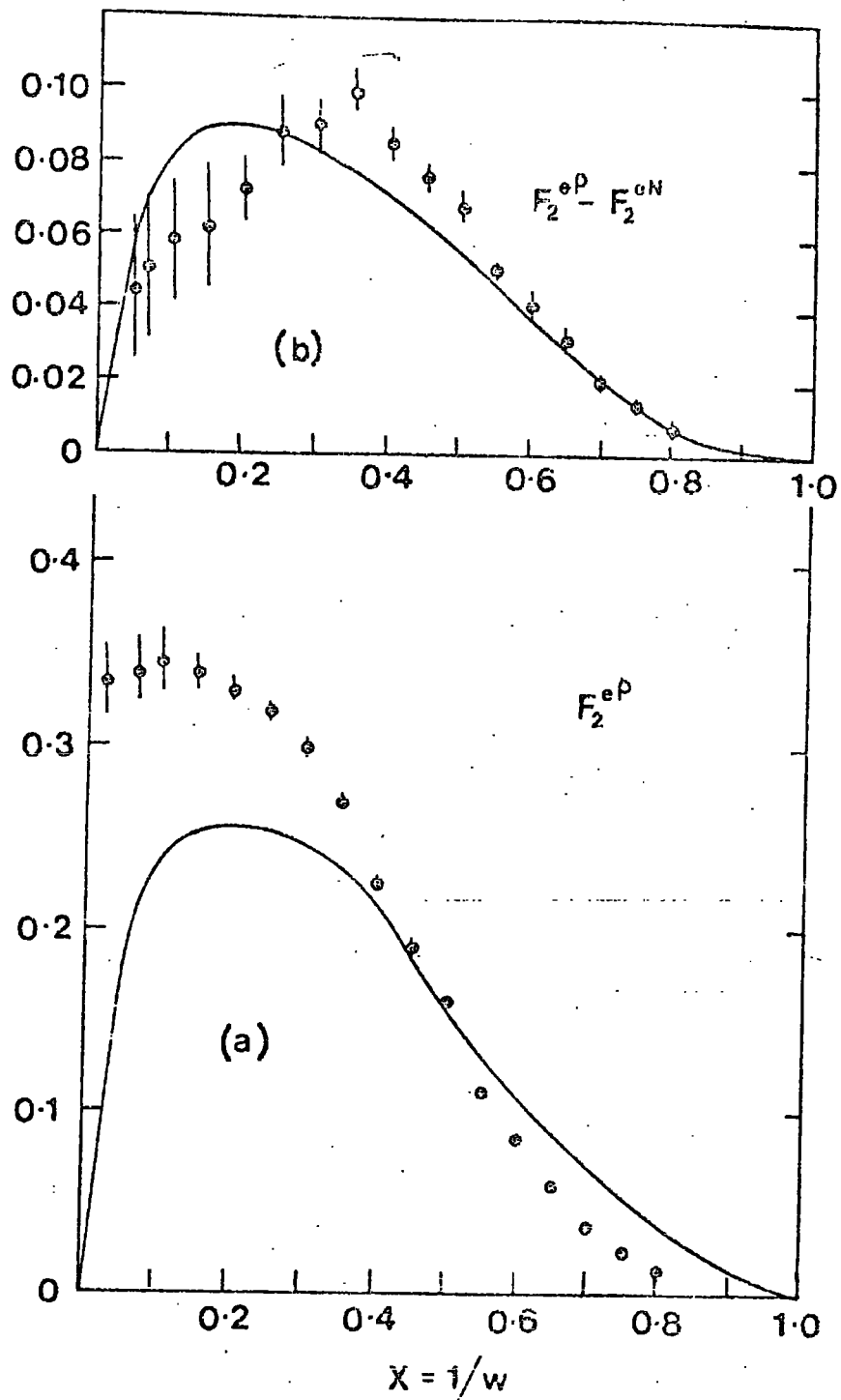
Fig. 27b' (Upper): If the sea has zero isospin and is even under charge conjugation (hence $F_2^{ep} - F_2^{eN} = \frac{1}{3}V$ ). In lower part ( $V = F_2^{ep}$ contribution from the sea)) is plotted versus x.

NEUTRINO AND ANTINEUTRINO TOTAL CROSS SECTIONS ON NUCLEONS
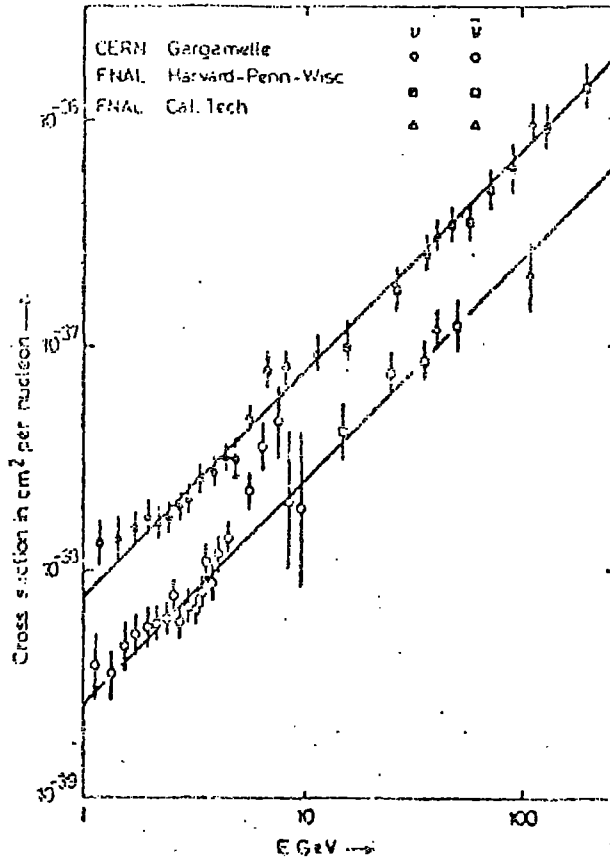
Fig. 28: Total cross-sections
for scattering of neutrinos and
antineutrinos by nucleons. The
measurements are consistent with
a simple linear energy dependence,
and with a constant ratio of anti-
neutrino to neutrino cross-sections,
with a mean value $0.36 \pm 0.02$ .
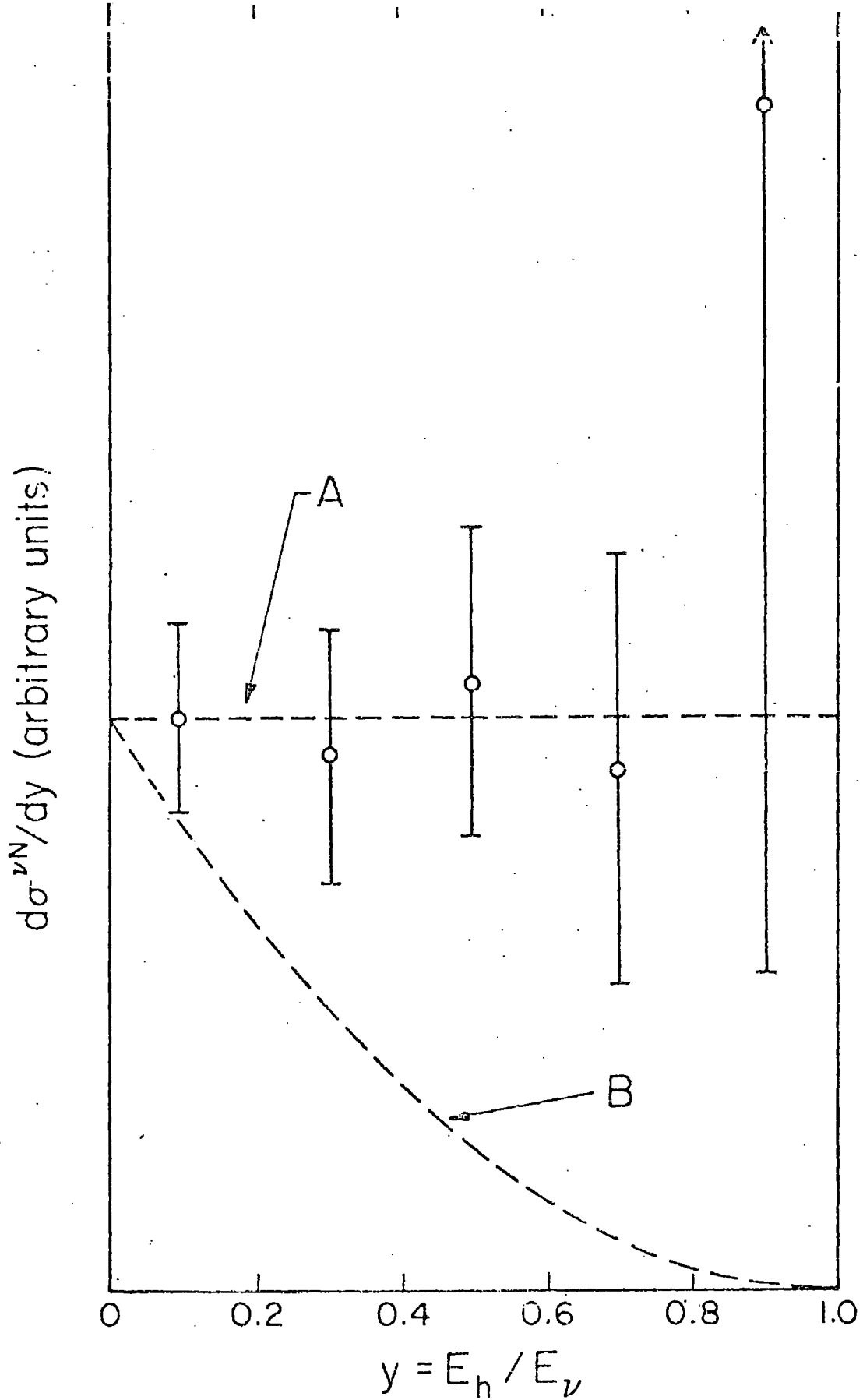
Fig. 29: $d\sigma^{\nu N}/dy$ versus y for $\langle E_\nu \rangle \sim 50$ GeV. A flat y dependence and a $(1-y)^2$ dependence are shown for comparison.
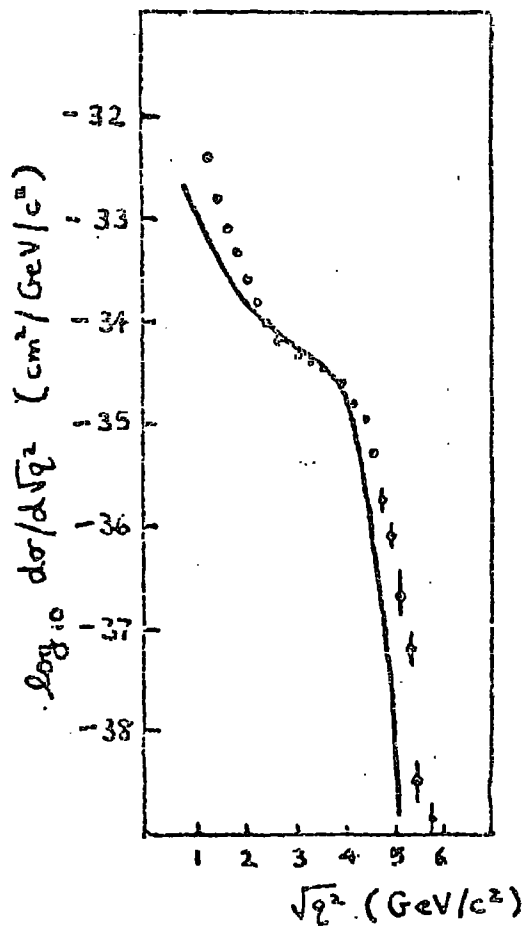
Fig. 30: Data for heavy
muon-pair production on a
uranium target, with curve
calculated from the Drell-
Yan term.
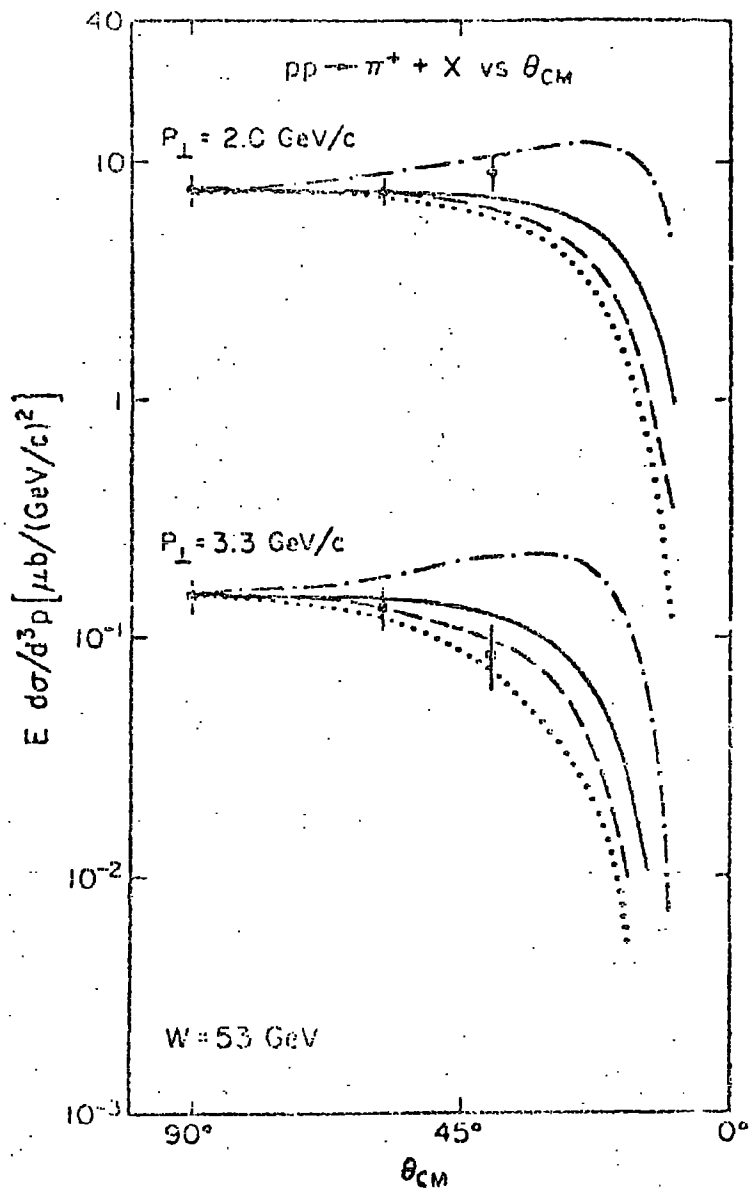
Fig. 31: The angular dependence of $E\,d\sigma/d^3p$ $(pp \to \pi^+ X)$ at $W = 53$ GeV and $P_t = 2.0$ and $3.3$ GeV/C resulting from several choices for $d\hat{\sigma}/d\hat{t}$ : $(\hat{s}^2+\hat{u}^2)/\hat{s}^2\hat{t}^4$ (dash-dot), $1/(-\hat{s}\hat{t}^3)$ (solid), $1/(\hat{s}^2\hat{t}^2)$ (dashed), $1/\hat{s}^4$ (dotted).
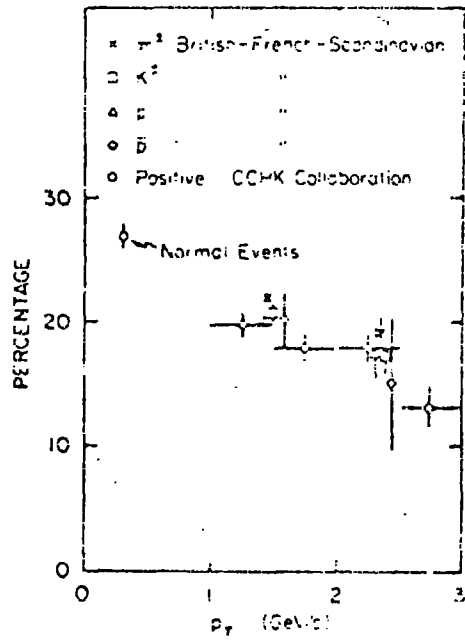
Fig. 32: Percentage of
events with leading
particles as a function
of the transverse momentum
of the large $P_\perp$ secondary.
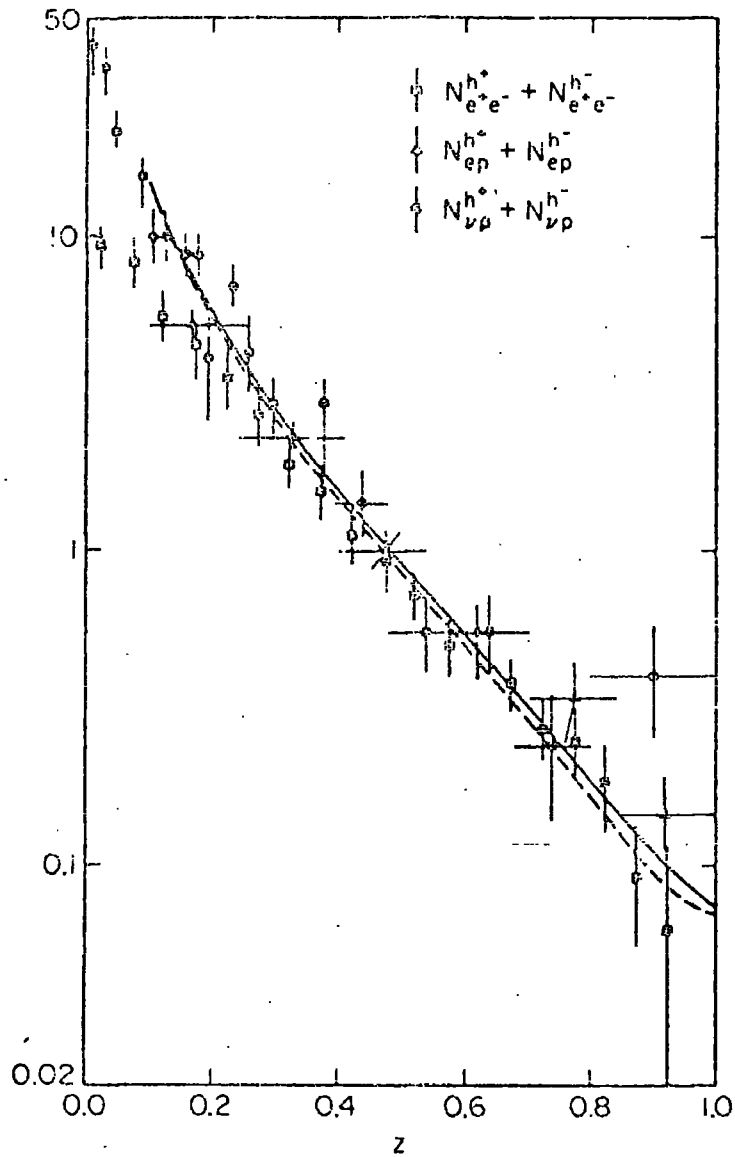
Fig. 33: Comparison of three separate experimental methods of finding $P_{h/q}$ (z) . The three different lepton processes differ slightly because they weight quark types differently. The solid line is the Field Feynman parameterization for neutrino case and dashed is $e^+e^-$: electroproduction lies between these two.
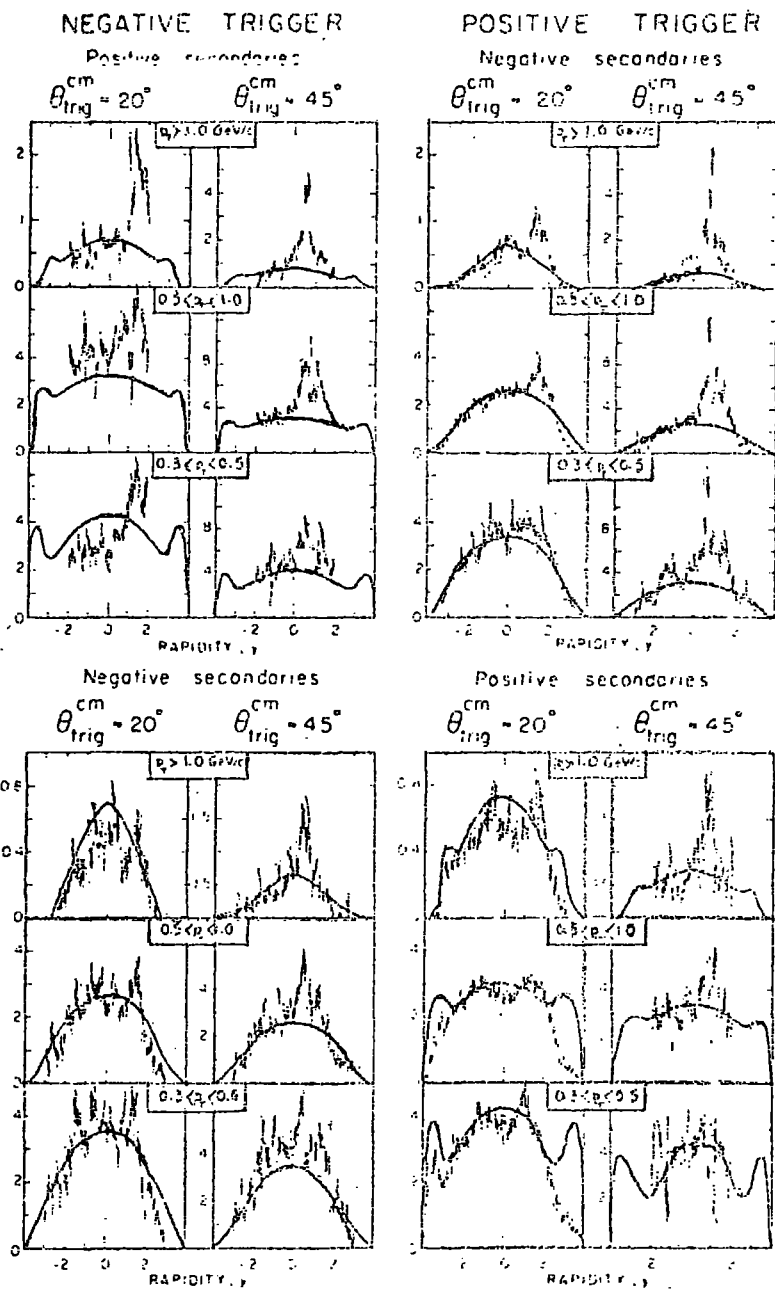
Fig. 34: Rapidity distribution of charged particles emitted towards the $20°$ $\pm$ and $45°$ $\pm$ large $P_\perp$ trigger for three $P_\perp$ intervals. The vertical scale is the charged multiplicity, times 100, per interval of $\Delta\phi$ and $\Delta y$ (in radian$^{-1}$). Corresponding minimum bias distributions are shown as solid lines.
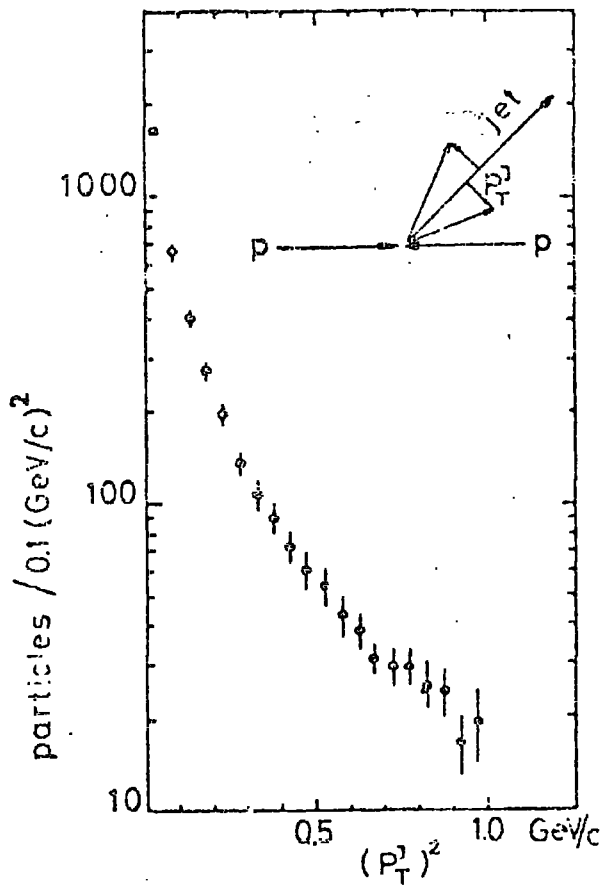
Fig. 35: Transverse momentum
squared distribution of particles
in the "jet" towards the trigger,
relative to the jet axis for the
$45°$ ± trigger.
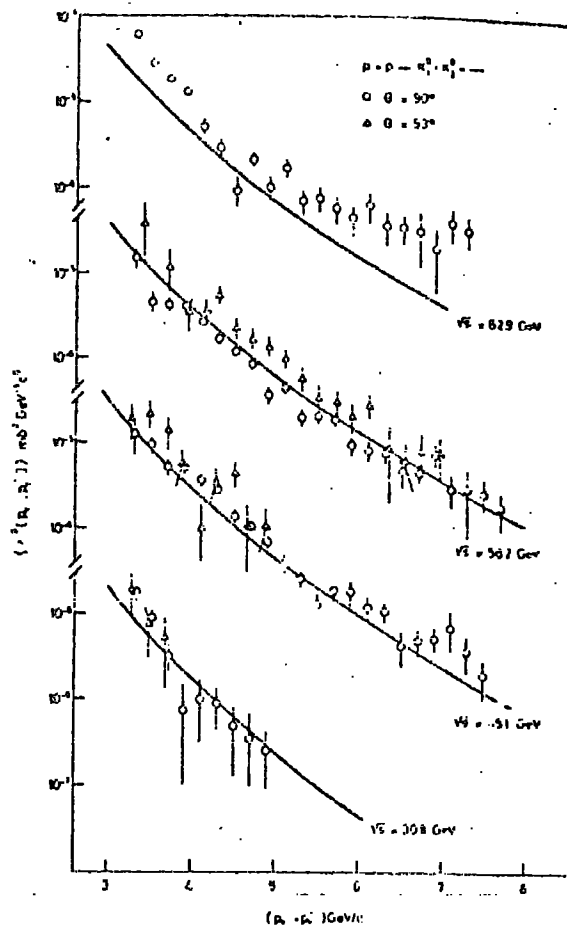
Fig. 36: Invariant cross-
sections for production of
two alongside $\pi^{o\prime}s$.
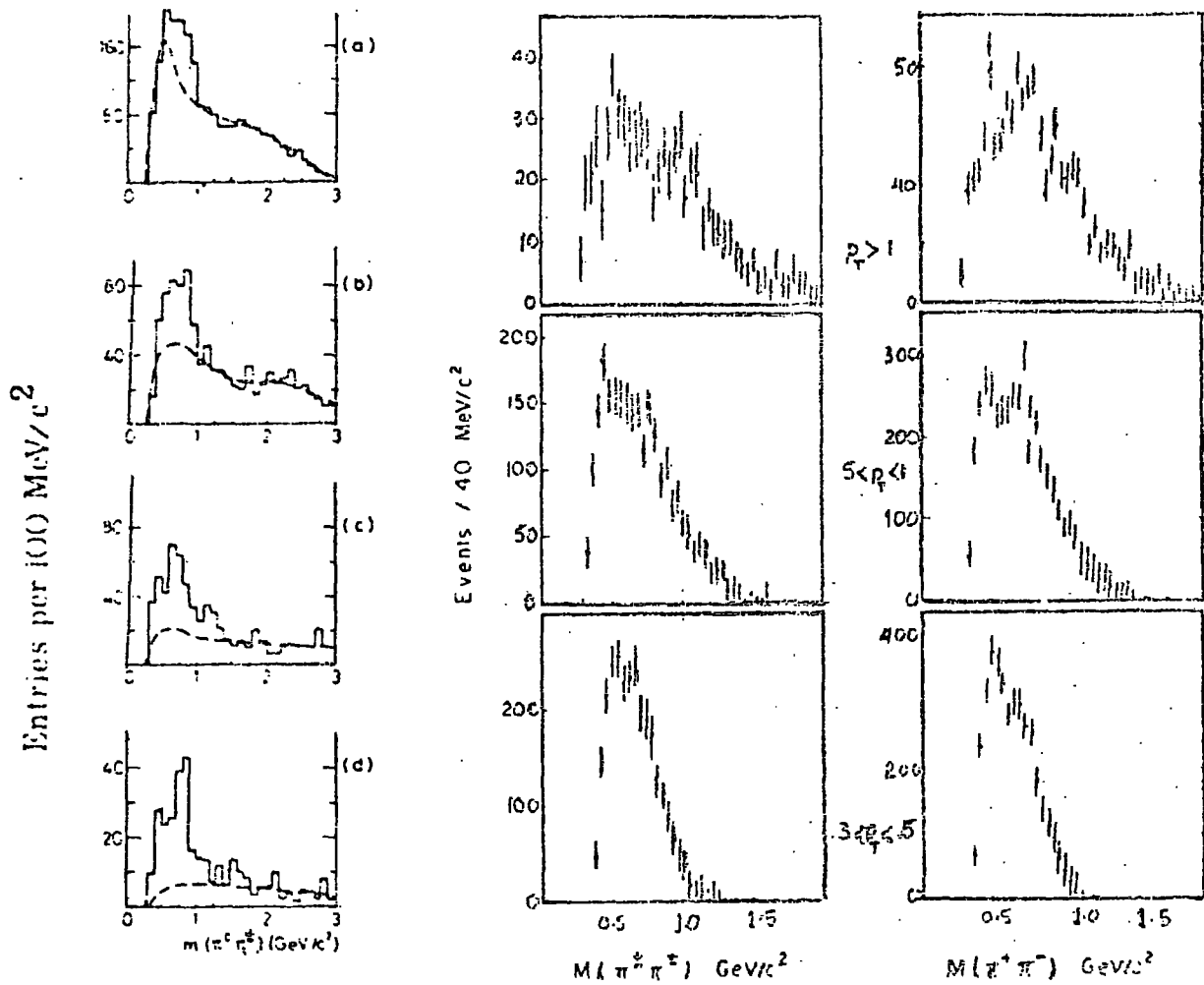
Fig. 37

$\pi^0 \pi^{\pm}$ invariant mass distrib-
ution for charged particles
produced towards ($|y| < 2$)
the $90°$ $\pi^0$ trigger for four
$p_x$ intervals:

a)   $0.4 < p_x < 0.6$ GeV/C

b)   $0.6 < p_x < 0.3$ GeV/C

c)   $0.8 < p_x < 1.1$ GeV/C

d)   $1.1 < p_x < 1.7$ GeV/C

The dashed line is an esti-
mation of the uncorrelated
minimum bias background.
CERN R412 data.

$\pi \pi$ invariant mass distrib-
ution for charged particles
produced in the peak ($0 < y <$
1.5) towards the $45°$ $\pm$
trigger for three $p_T$ intervals:
$0.3 < p_T < 0.5$ GeV/C;   $0.5 < p_T$
$< 1.0$ GeV/C;   $p_T > 1.0$ GeV/C.
The data are shown separately
for the neutral pairs ($Q = 0$)
and the doubly charged pairs
($|Q| = 2$). CCHK data.
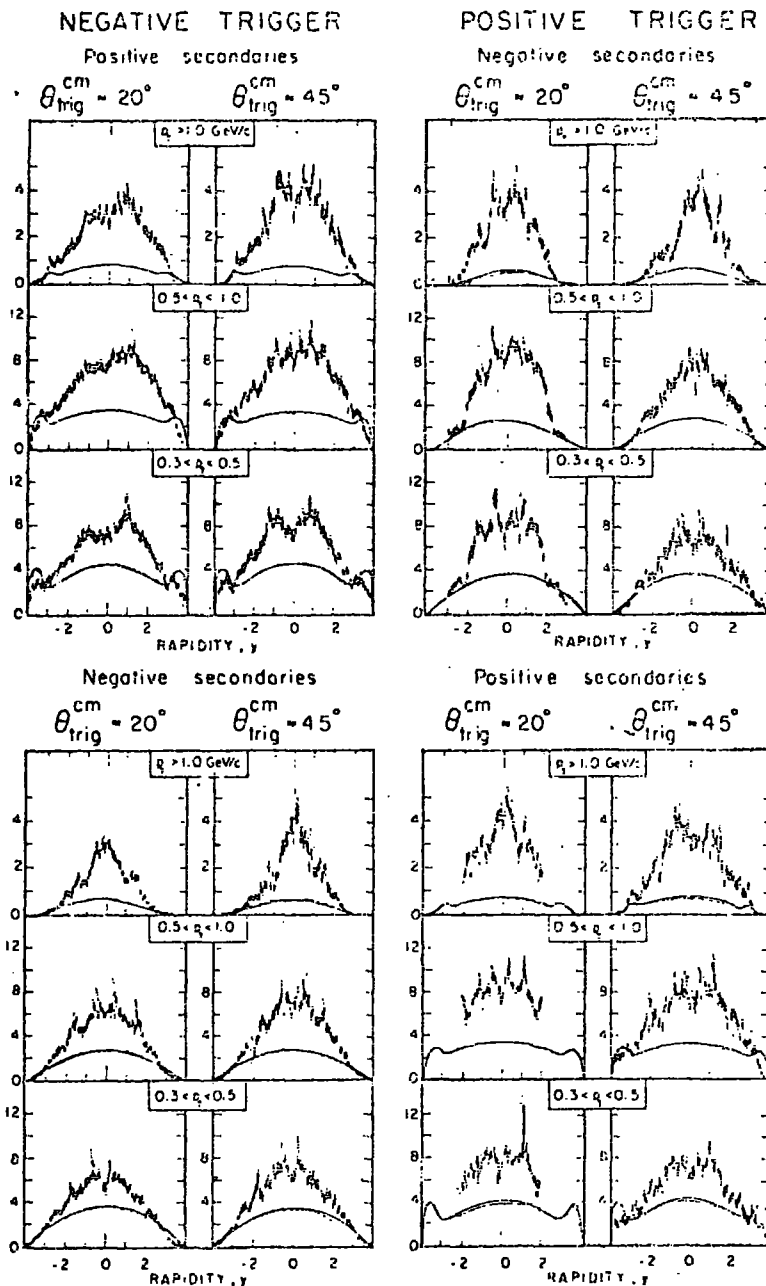
Fig. 38: Rapidity distributions of charged particles produced away from the 20° ± and 45° ± large $p_T$ triggers for three $p_T$ intervals. The vertical scale is the charged multiplicity, times 100, per interval of $\Delta\phi$ and $\Delta y$ (in radian$^{-1}$). Minimum bias distributions are shown as solid lines. CCHK data.
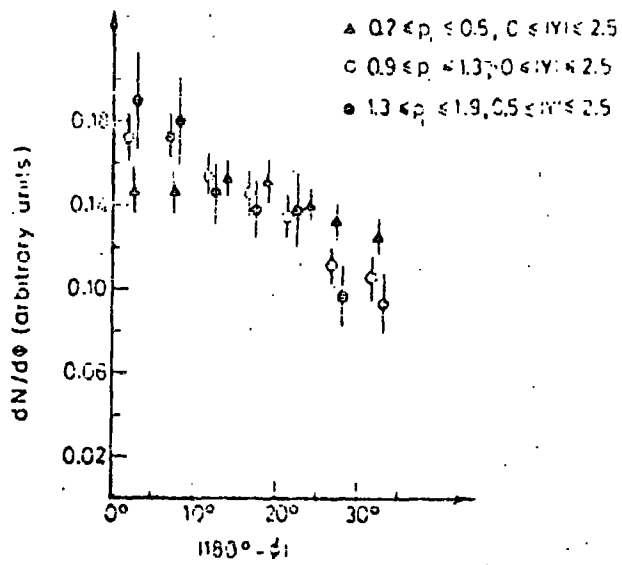
Fig. 39: Azimuthal distribution
of charged particles in the away
region in the events with large
$P_t$ $\pi^o$ emitted at 90°.
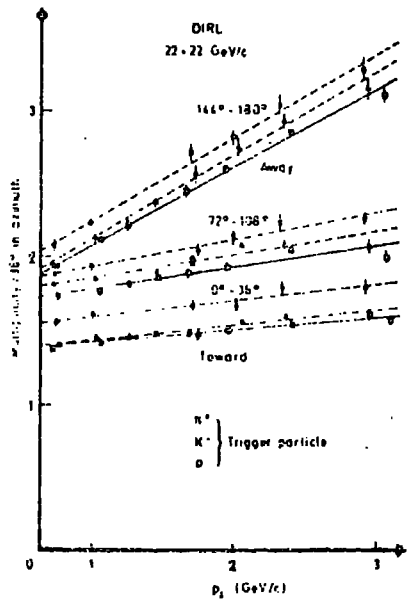
Fig. 40:   Away and towards
multiplicity distributions.
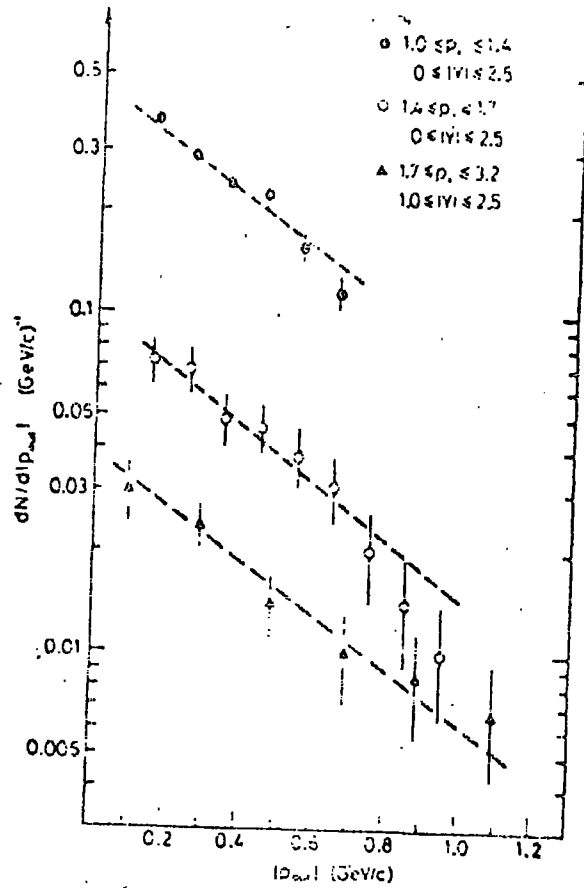
Fig. 41: Distributions of
$|P_{out}|$ for different intervals
of transverse momentum $p_{\perp}$ of the
charged particles. The dashed
lines correspond to a function
$dN/d|P_{out}| \sim exp(-2|P_{out}|)$.
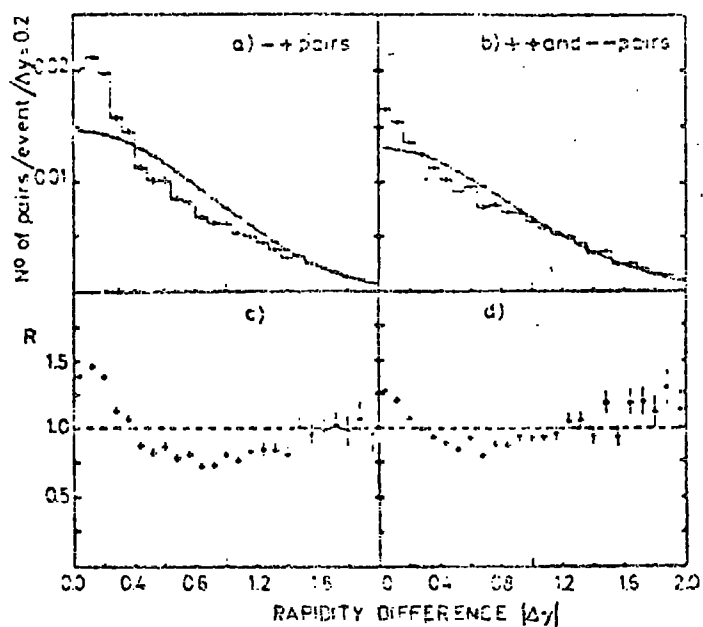
Fig. 42: The distribution of rapidity
difference of pairs of particles in the
away region (full line). Also shown is
the equivalent distribution for uncorre-
lated pairs. (c) and (d) show normalised
rapidity difference distributions obtained
by taking the ratio of the distributions
of (a) and (b), respectively, to the back-
ground distributions of these figures.
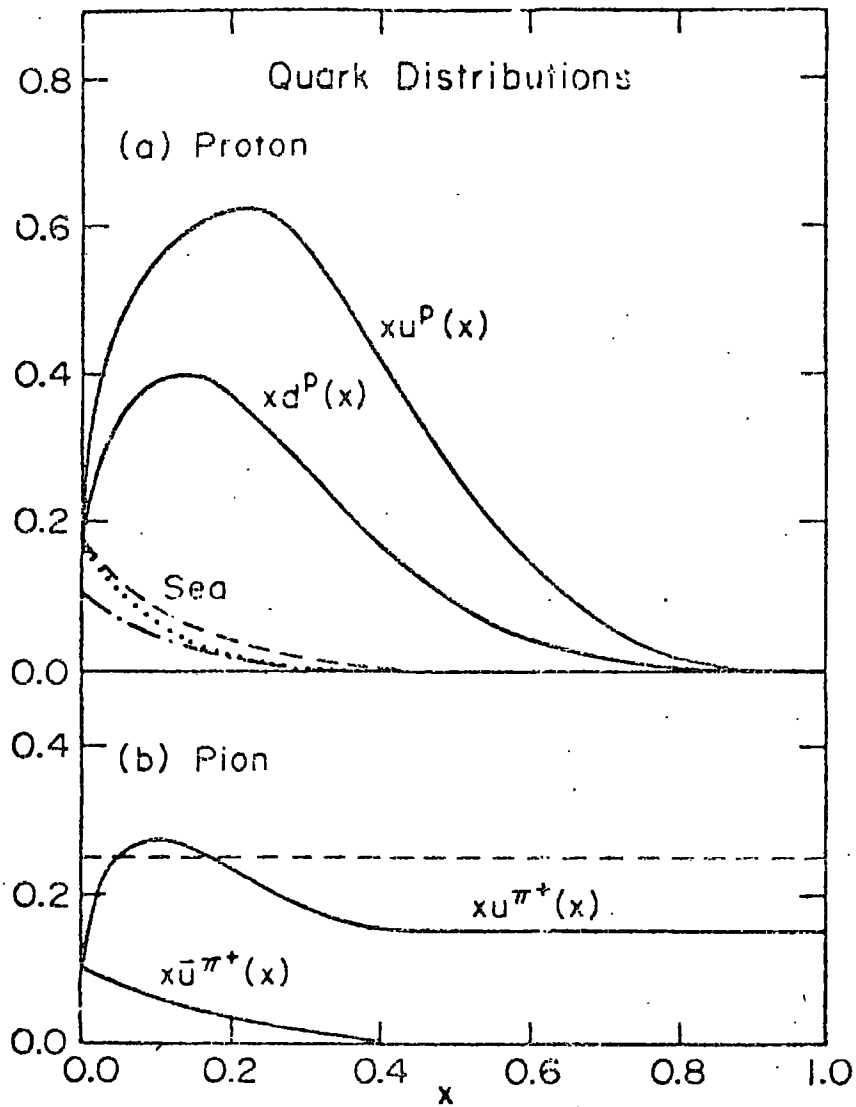
Fig. 43: Quark distributions within the proton. It is assumed that as $x \longrightarrow 1$; $x u(x) \sim (1-x)^3$ and $x d(x) \sim (1-x)^4$ . Also an unsymmetrical sea, with $x \bar{d}(x)$ (dashed curve) greater than $x \bar{u}(x)$ (dotted curve) and $x s(x) = x \bar{s}(x) = 0.1 (1-x)^6$ has been taken.
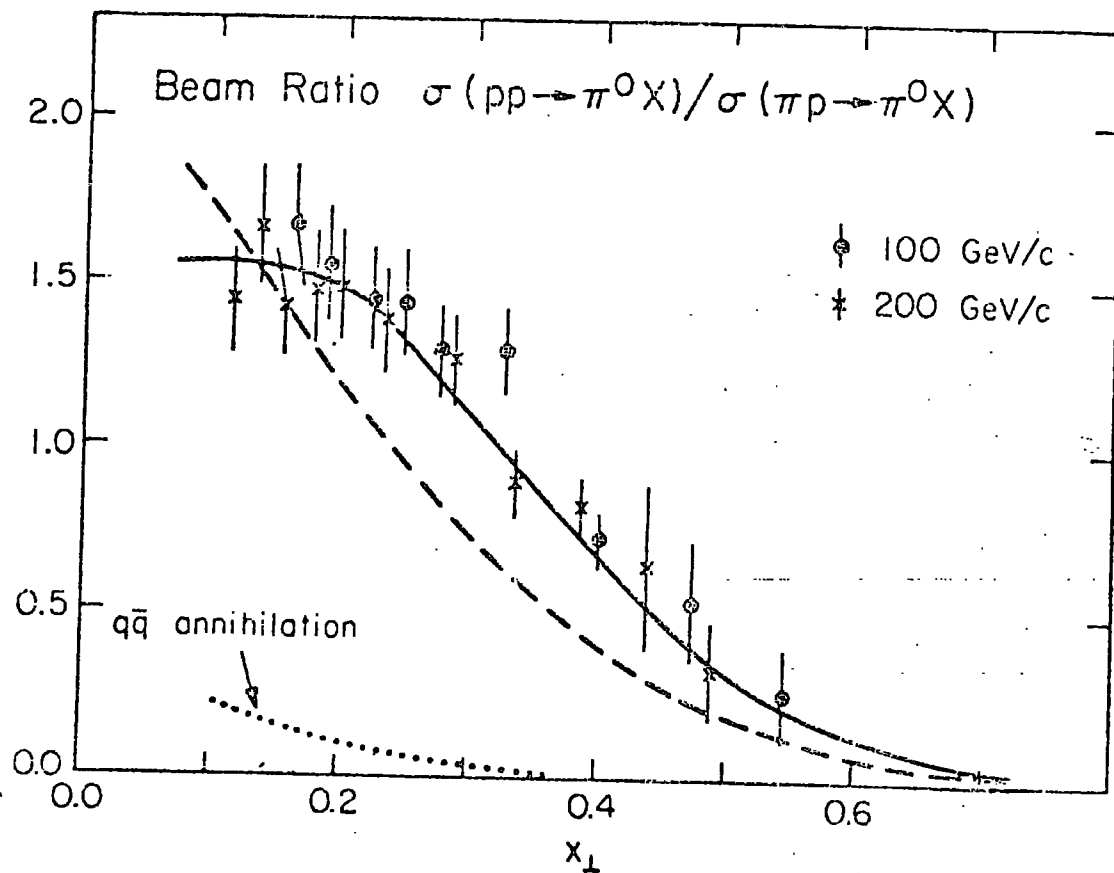
Fig. 44: The ratio of the invariant cross section $\sigma(pp \to \pi^0 x)/\sigma(\pi p \to \pi^0 x)$ at $\theta_{c.m.} = 90^0$ and $P_{lab} = $ 100 and 200 GeV/C.
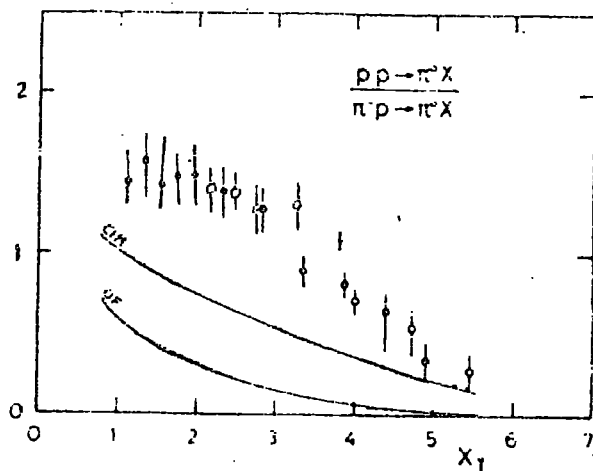
Fig. 45: The beam ratio
$PP \longrightarrow \pi^0 + X / \pi^- p \longrightarrow \pi^0 + X$
as a function of $x_\perp$ at $\Theta_{c.m.}$
$= 90^0$.
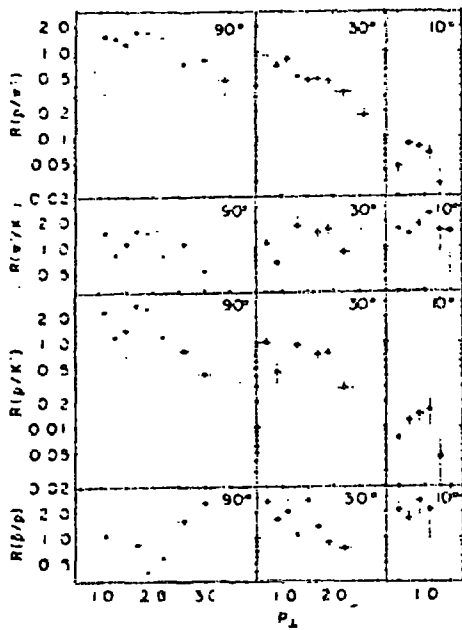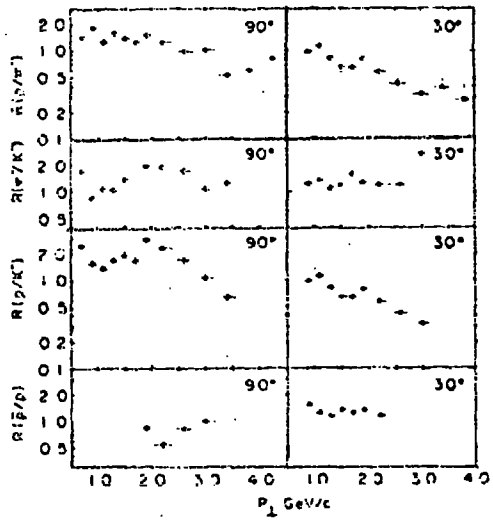
Fig. 46: Ratios of invariant cross sections versus $P_\perp$ at (a) 100 GeV/C, (b) 200 GeV/C.
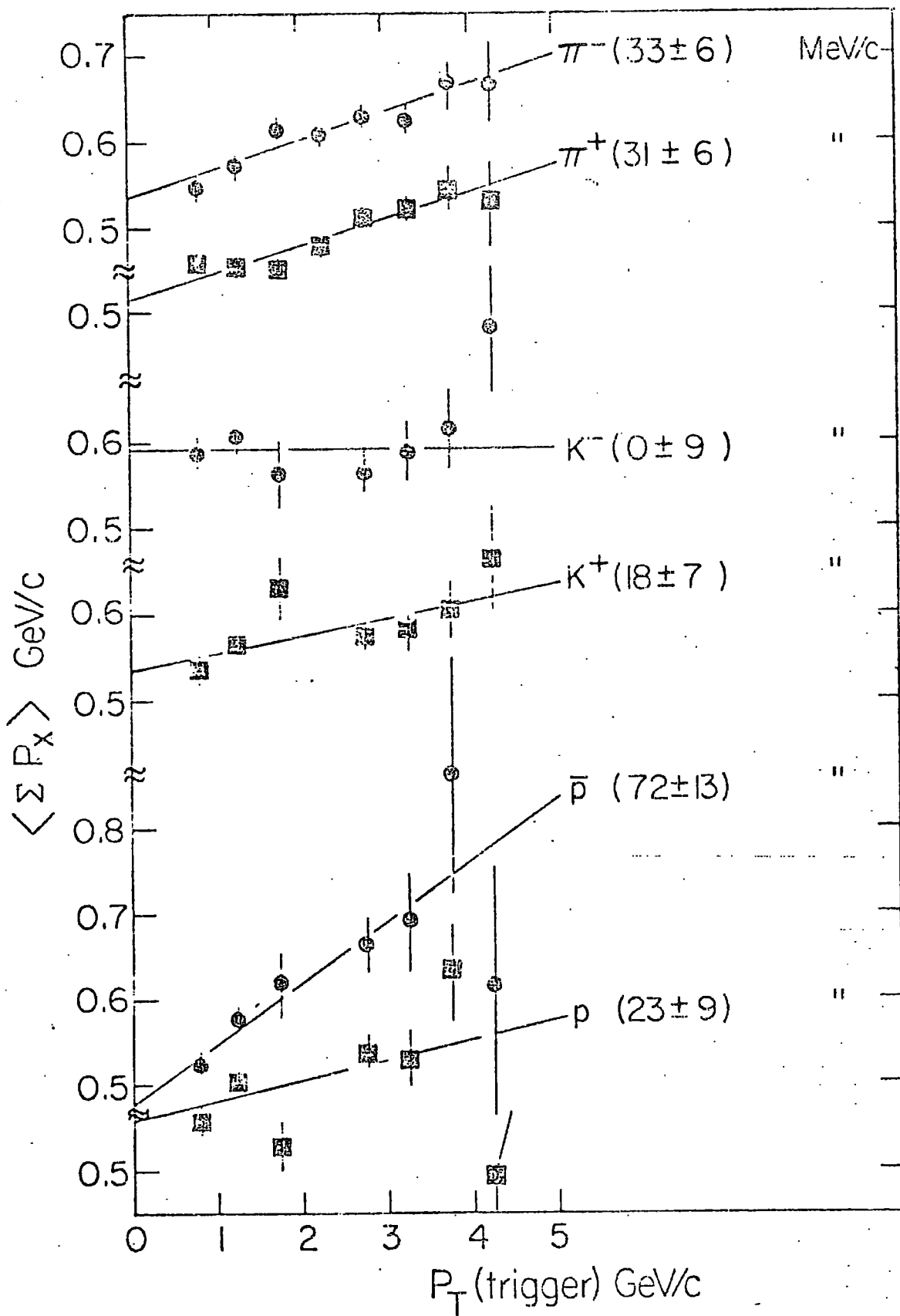
Fig. 47: Mean value of the momentum carried by charged particles on the trigger side within the rapidity interval |y| < 1 for different triggering particles.

HADRONS IN QUARKS



(a)

Fit
corresponds
to
$\langle k_T (h/q) \rangle = 315$ MeV/c

QUARKS IN HADRONS



(b) $\dfrac{\langle k_T^{\mu^+\mu^-} \rangle}{\sqrt{2} \langle k_\perp (q/h) \rangle} \approx$

$p \cdot C \rightarrow \mu^+ \mu^- X$

MASS $(\mu^+ \mu^-)$ GeV
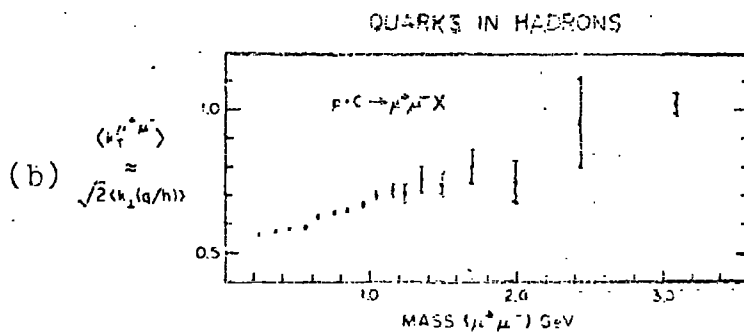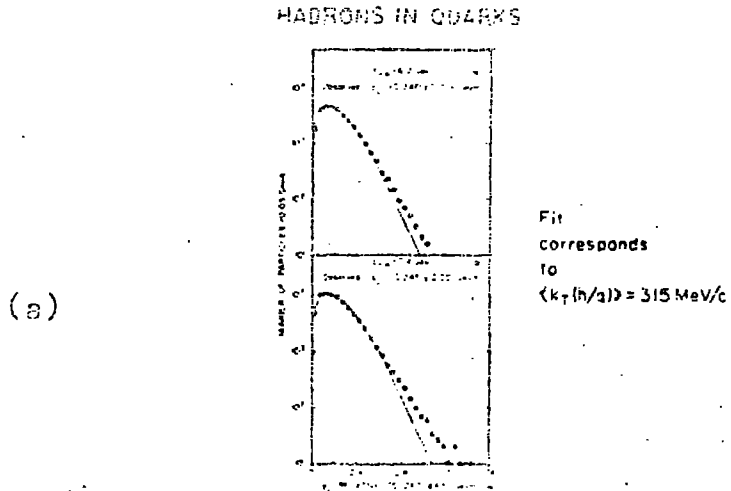
Fig. 48:  Experimental evidence
for transverse momenta of .
(a) hadrons in quarks and
(b) quarks in hadrons.
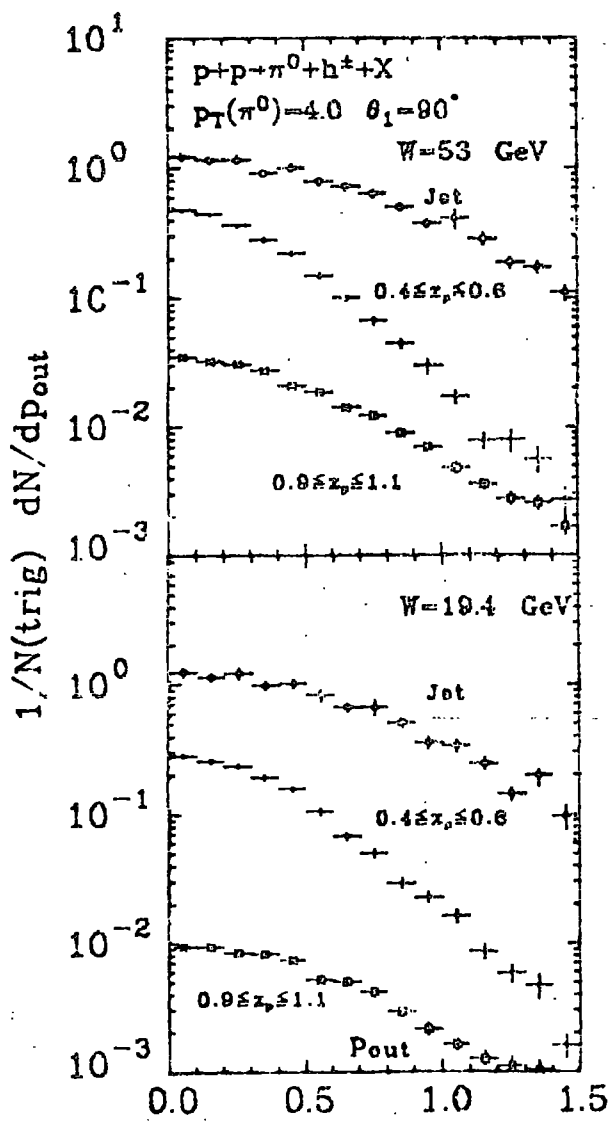
Fig. 49: Dependence of the away-side Pout distribution on the $\delta_p$ bin of the away hadrons from quark-quark scattering model for the process $PP \longrightarrow \pi^0 + h^{\pm} + X$ at $P_\perp(\pi^0) = 4.0$ and $\theta = 90^0$ using $< k_\perp >_{h \to q} = 500$ MeV.

TOWARDS DISTRIBUTIONS
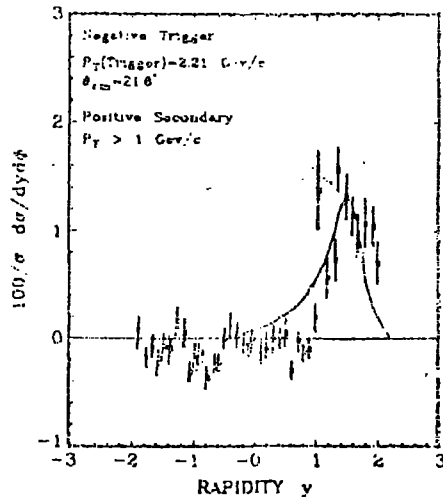


(a)

TOWARDS DISTRIBUTIONS
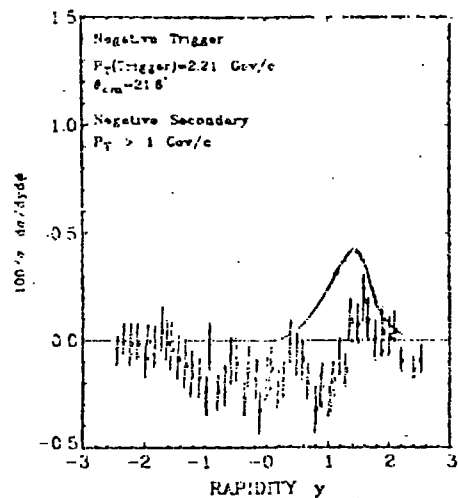


(b)

Fig. 50: Towards side rapidity
distribution. The trigger has
charge mean $P_\perp$ of 2.21 GeV/C and
a rapidity of 1.65. In (a) the
secondaries have + charge and lie
within an azimuth of $25°$ of the
trigger. In (b) the secondaries
have -charge, the other things are
the same as (a) but scale has been
changed. The solid curve is the
theory calculated with $< k_\perp >_{h \to q} =$
500 Mev.

TOWARDS SIDE CHARGED PARTICLES
TRIGGER IS $p_T^{\pi^0} > 3\,GeV/c$
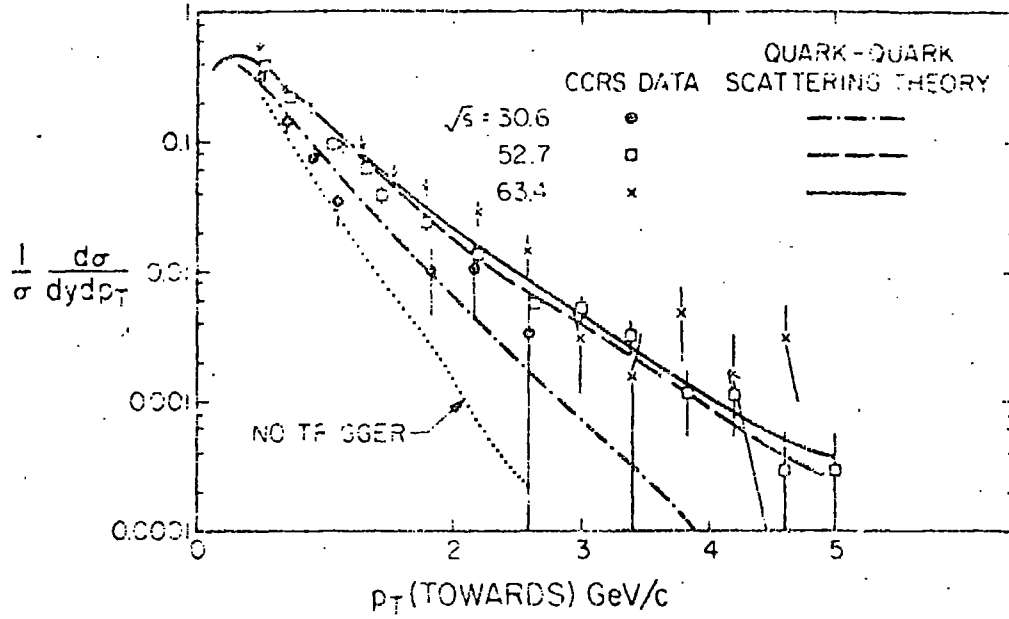


Fig. 51: Compares the energy dependence
of the towards correlation function in
the CCRS data and the model Q theory.

AWAY DISTRIBUTIONS

Negative Trigger
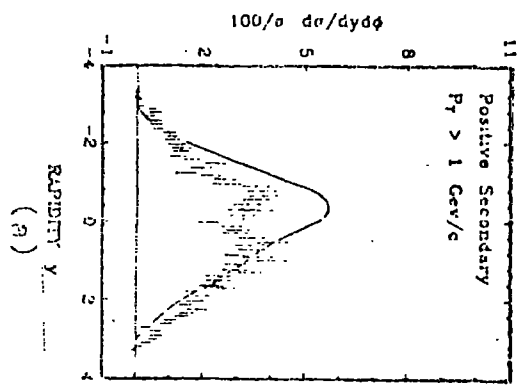$P_T$(Trigger)~2.43 GeV/c
$\theta_{cm}$=90°
Positive Secondary

Positive Secondary
$P_T > 1$ GeV/c

$100/\sigma \ d\sigma/dyd\phi$

RAPIDITY y

(a)

AWAY SIDE RAPIDITY

TRIGGER - CHARGE
$\theta_{cm}$ = 17.6°
$P_T$ = 2.65 GeV/c

SECONDARY - CHARGE
$|\phi - 180°| < 40°$
$P_T > 1$ GeV/c

$d\sigma/dt$
$(\hat{s}^2+\hat{u}^2)/(s'^2 \cdots)$
$1/(1-s/s')$
QED CM
$1/s^2$

$\frac{100}{\sigma} \frac{d\sigma}{dyd\phi}$

RAPIDITY y

(b)
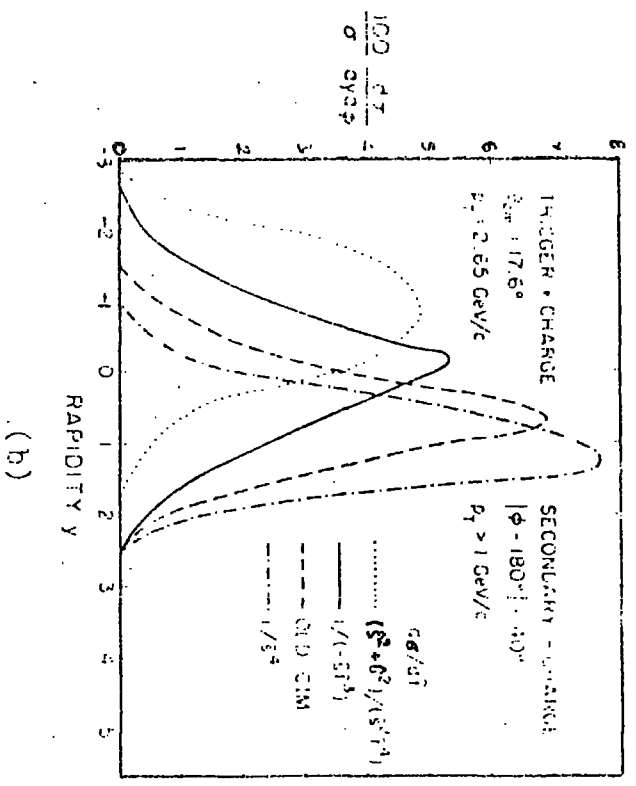
Fig. 52: (a) Comparison of the data with the predictions of the diffused quark model (signal and background have been subtracted). (b) Variation of the away side rapidity distribution with the form of $d\sigma/dt$ (see Chapter III). All models used $\omega y \ (-\delta k_1)$ internal transverse momentum smearing.

(a)-COPLANAR SINGLE HIGH $p_T$ EVENT
(LOW MULTIPLICITY)

X view

Run 195
Event 68
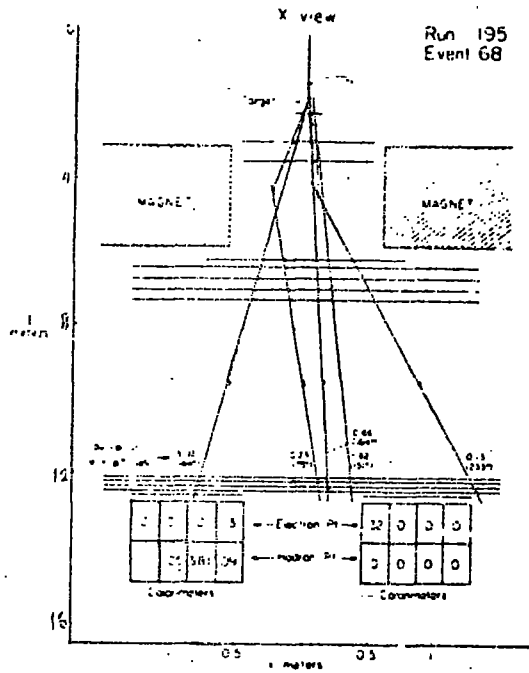
(a)

Fig. 53: (a) A single particle trigger
in an unusually low multiplicity event.
(b) A jet event.

(b)- SINGLE JET EVENT
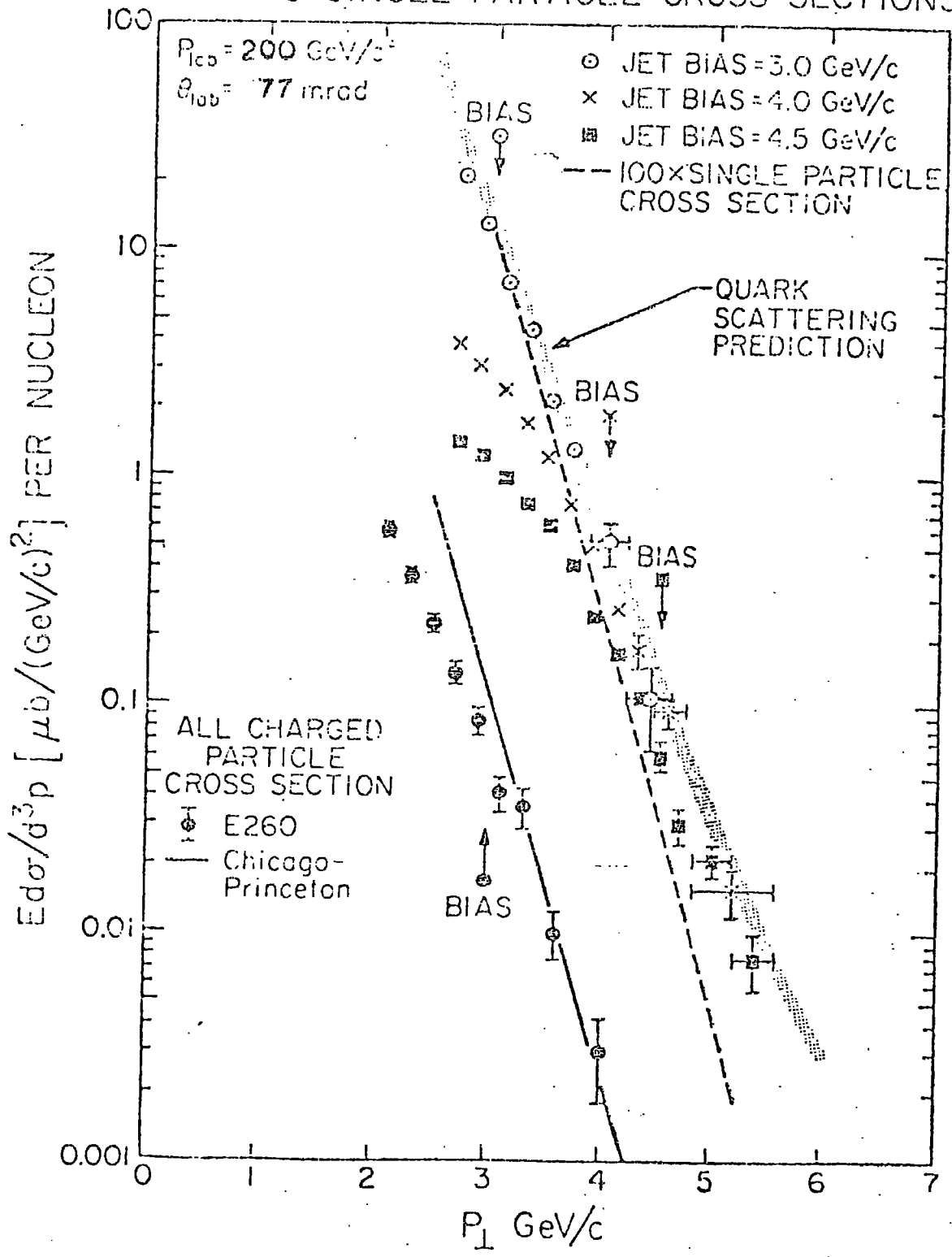
X view

Run 230
Event 75

(b)
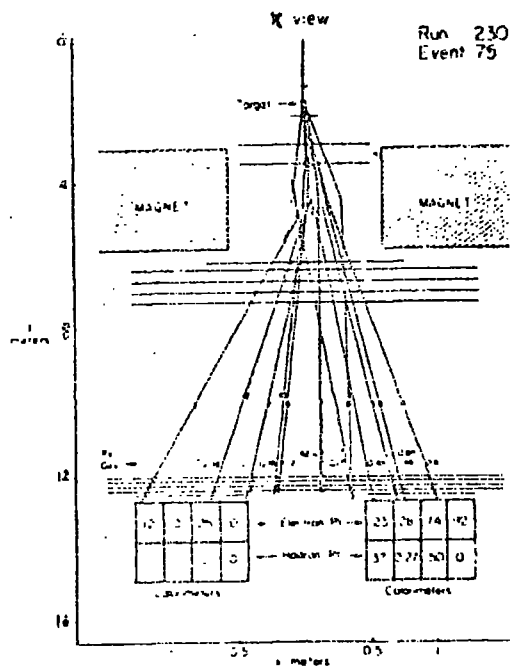
Fig. 54: Comparison of the jet and single particle (summed over all charges) cross sections measured off beryllium at 200 GeV/C by E 260.
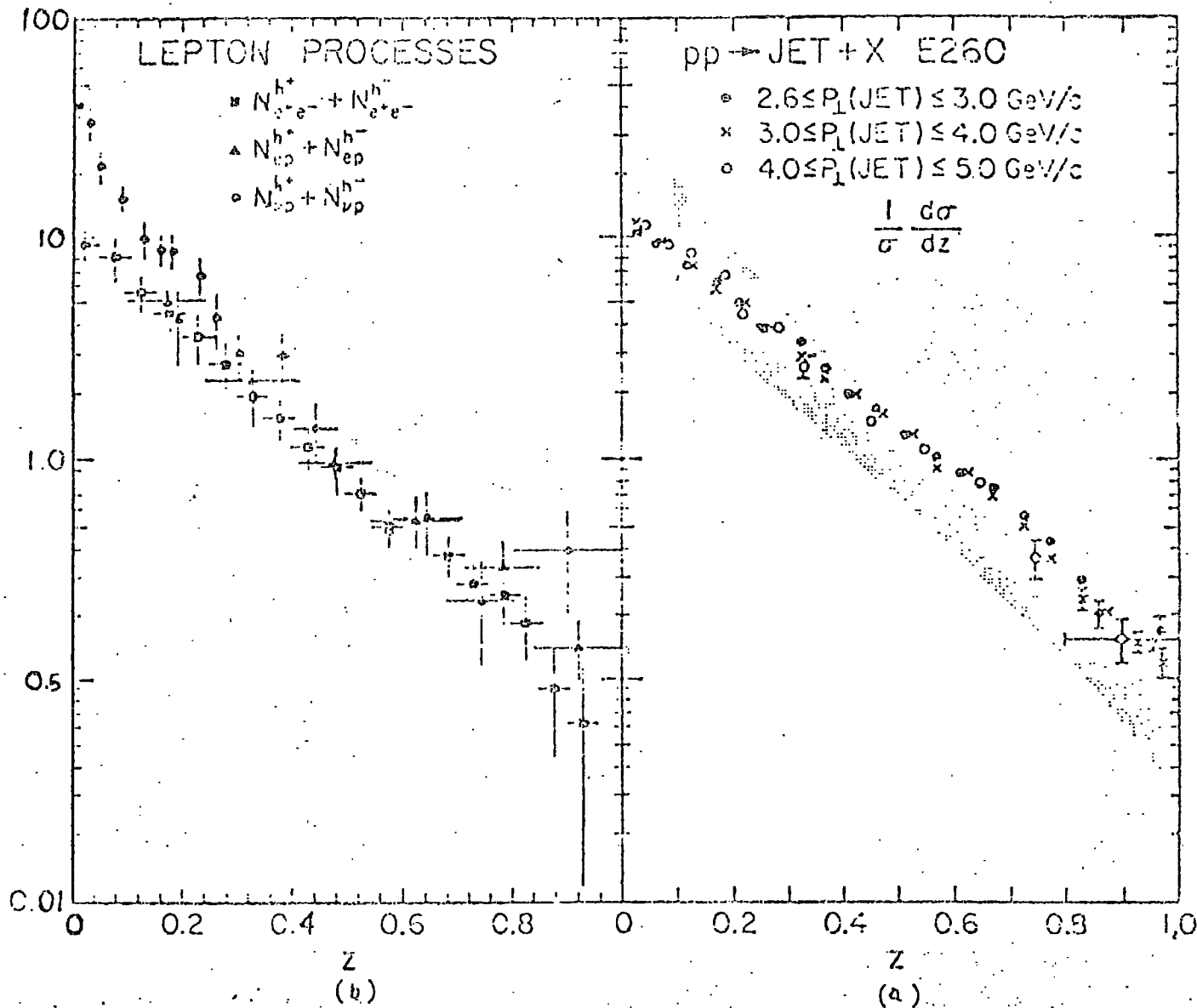
# QUARK FRAGMENTATION



Fig. 55: (a) Multiplicity of charged hadrons within the jet triggers observed by E 260. (b) Charge multiplicity function obtained from the processes: $e^+e^- \to h^\pm X$, $ep \to e h^\pm X$, $\nu T \to \mu^- h^\pm X$.
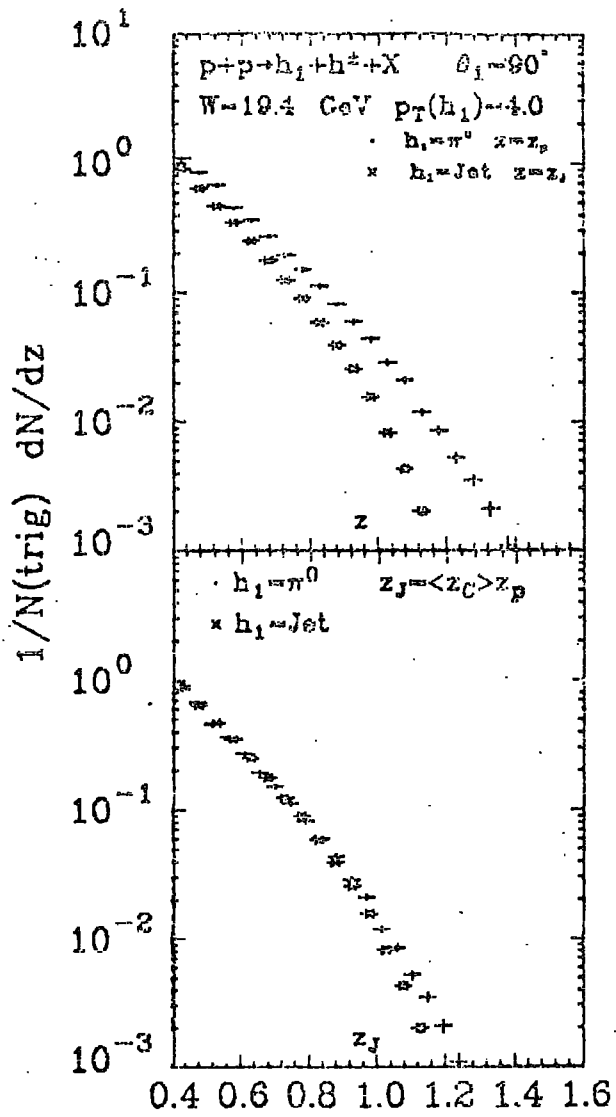
Fig. 56: Away side distribution
of charged hadrons for a $\pi^0$ and a
jet trigger in PP collision at $W =$
19.4 GeV and $p_T$ (trigger) = 4.0 GeV/C
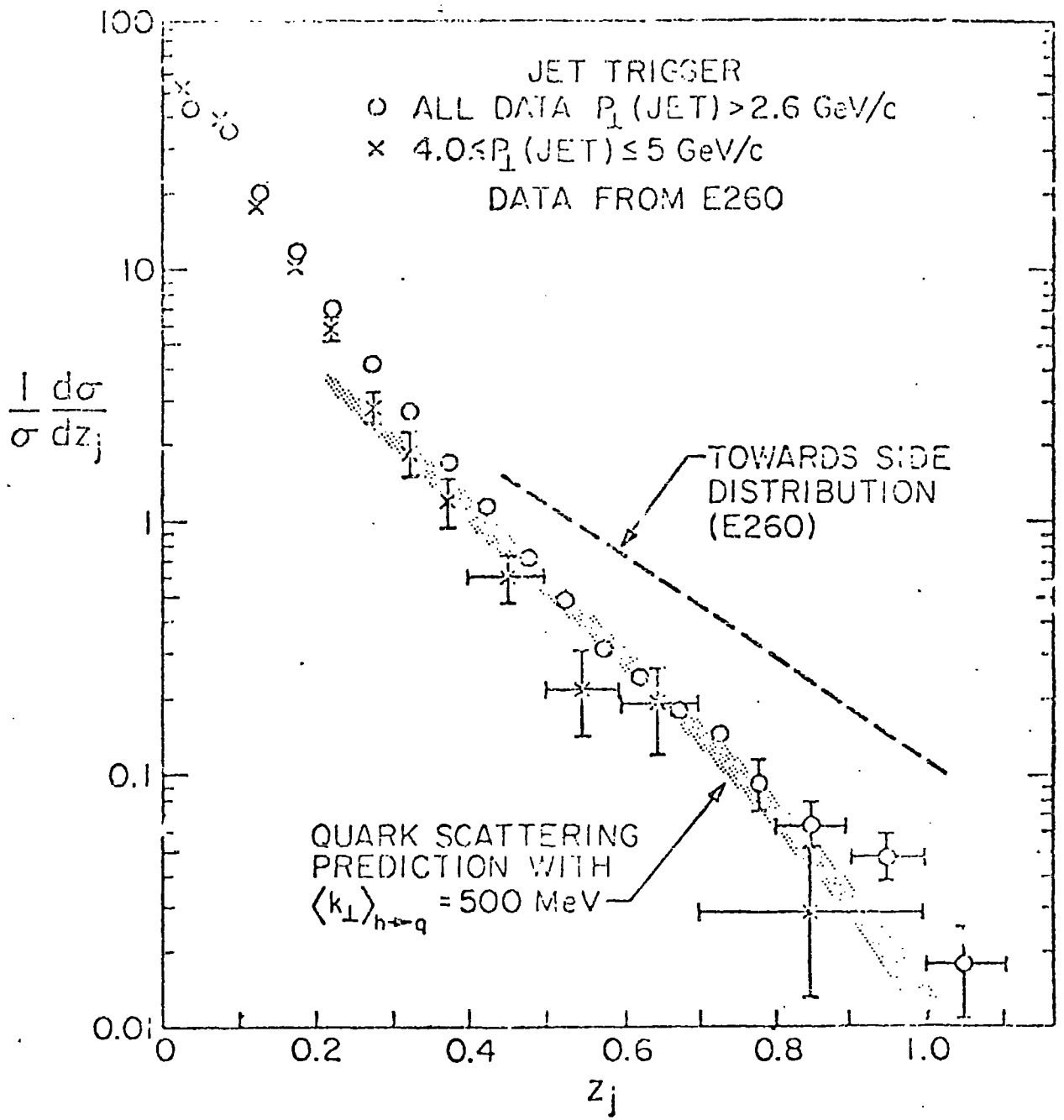— here $<k_\perp>_{h\to q}$ = 500 MeV.

Fig. 57: Away side distribution of charged hadrons and its comparison with the towards side distribution.